Anti-Correlation Digital Halftoning[*]

Dmitri A. Gusev[†]

Abstract. A new class of digital halftoning algorithms is introduced. Anti-correlation digital halftoning (ACDH) combines the idea of a well-known game, Russian roulette, with the statistical approach to bilevel quantization of digital images. A representative of the class, serpentine anti-correlation digital halftoning, is described and compared to error diffusion, ordered dither, and other important digital halftoning techniques. Serpentine ACDH causes fewer unpleasant correlated artifacts and less contouring than the benchmark algorithms. The quantization noise spectra associated with serpentine ACDH possess beneficial characteristics related to properties of the vision system. The term "violet noise" is proposed to describe quantization noise with stronger bias in favor of high-frequency components than that of blue noise. Novel techniques for color visualization of the noise spectra and the corresponding phase spectra are introduced, and the relative significance of the magnitudes and phases of the discrete Fourier transform of the quantization noise is studied. Unlike popular algorithms based on error diffusion, serpentine ACDH does not enhance edges. This is good for applications to digital holography and medical imaging. A simple input preprocessing technique allows one to introduce edge enhancement if desired, while keeping it more isotropic than that of error diffusion. The relation between unwanted transient boundary effects and edge enhancement accompanying error diffusion is examined, and approaches to reduction of boundary effects are considered. Serpentine ACDH does not cause significant boundary effects. The average intensity representation by different algorithms is studied for constant input levels (serpentine ACDH does remarkably well). Prospects for ACDH research are discussed.

Keywords: digital halftoning, digital imaging, anti-correlation digital halftoning, error diffusion, halftoning, dithering, ordered dither, serpentine raster, Russian roulette, noise spectrum, halftone, blue noise, image printing.

---

1. Introduction

Inherent limitations of devices for image visualization and printing (displays, printers) often require quantization of two-dimensional digital images to a limited number of grayscale levels. The case of bilevel quantization is of particular interest when an image is to be printed on a printer that can only produce black-and-white pictures. *Digital halftoning* [218] means image quantization by algorithms that exploit properties of the vision system to create the illusion of continuous tone. Many related neurobiological aspects of vision are discussed in [91]. Digital halftoning has been applied in such areas as digital holography [191], desktop publishing [202], medical imaging [164, 184], image compression/restoration [87], non-uniform sampling [144], video rendering [222], pattern recognition [80], verification of monochrome vision models [78, 128], and three-dimensional computer graphics [206].

This paper will be dealing with rectangular input and output digital images consisting of pixels (dots) on a common square grid. Other cases are considered elsewhere [203, 218, 247].

Section 2 will provide an overview of existing digital halftoning techniques — ordered dither, error diffusion, etc.

Section 3 will cover different approaches to halftone image quality evaluation. The term "violet noise" will be introduced to describe quantization noise with stronger bias in favor of high-frequency components than that of blue noise as it is defined by Ulichney [218].

A new class of digital halftoning algorithms, *anti-correlation digital halftoning (ACDH)*, will be introduced in Section 4. A representative of the new class, serpentine anti-correlation digital halftoning, will be defined. We will also discuss some aspects of texture perception that affect asymmetric anti-correlation filter design.

Section 5 will report results of visual examination of test image representations produced by different digital halftoning algorithms. Comparison of quantization noise spectra associated with the corresponding image-algorithm pairs will be discussed in parallel. It will be shown that serpentine ACDH causes fewer unpleasant correlated artifacts and less contouring than the benchmark algorithms, and that quantization noise spectra associated with the new method possess beneficial characteristics related to properties of the vision system. Novel techniques for color visualization of the noise spectra and the corresponding phase spectra will be introduced.

Section 6 will be devoted to the study of the relative significance of the magnitudes and phases of the discrete Fourier transform of the quantization noise.

Unlike popular algorithms based on error diffusion, serpentine ACDH does not enhance edges, nor does it cause significant transient boundary effects. In addition to that, it is preserves average intensities very well. Corresponding measurement results will be presented in Section 7, which will also establish a relation between the unpleasant boundary effects and edge enhancement accompanying error diffusion, and discuss approaches to reduction of boundary effects. While edge enhancement generally means extra distortion of the input image, it is sometimes considered pleasant, so we will describe a simple input preprocessing technique allowing one to add relatively isotropic edge enhancement to any digital halftoning algorithm.

Extension of ACDH to multilevel halftoning and color quantization will be discussed in Section 8.

Section 9 will present conclusions and outline prospective directions of research.

2. Overview of Digital Halftoning Techniques

For the purposes of our discourse, we define the input of a digital halftoning algorithm to be a two-dimensional digital grayscale image G represented by an $N_1 \times N_2$ matrix of real values $g_{i,j} \in [0, 1]$. Most of the paper is devoted to the case of bilevel quantization where a binary image B represented by an $N_1 \times N_2$ matrix of $b_{i,j} \in \{0, 1\}$ serves as output of the algorithm. The symbols $g_{i,j}$ and $b_{i,j}$ stand for *intensities* of pixels on a common square grid, where $i = 0, 1, \ldots, N_1 - 1$ and

$j = 0, 1, \ldots, N_2 - 1$ indicate line and column of a pixel respectively, thus describing its location in terms of the grid coordinates. An intensity value 0 means "black", and 1 means "white". It may be difficult to translate the intermediate intensity values into physically measurable quantities. We will return to this problem later in this paper. Other sources may assign other meanings to the word "intensity" [66, 100].

In many algorithms, the values $b_{i,j}$ are computed as outputs of an internal nearest-level binary quantizer. Whenever such a quantizer is present, the values of its inputs will be denoted $a_{i,j}$. Then

$$b_{i,j} = \begin{cases} 1 & \text{if } a_{i,j} \geq 1/2, \\ 0 & \text{if } a_{i,j} < 1/2. \end{cases} \tag{1}$$

The differences between the binary quantizer inputs and the corresponding input intensities will be referred to as

$$s_{i,j} = a_{i,j} - g_{i,j}. \tag{2}$$

The case when $s_{i,j} = s$ is simply a constant corresponds to ordinary bilevel *quantization with a fixed threshold*, which is well-known not to be a good halftoning algorithm ([218], Chapter 1). Figures 1 (a) and (c) feature two test image representations obtained by quantization with a fixed threshold equal to $1/2$, $s = 0$. Both 256×256 images are printed at the resolution of 100 dots per inch (dpi).

If $s_{i,j}$ are uncorrelated random numbers uniformly distributed on $[-1/2, 1/2]$, then we get *dithering with white noise* ([218], Chapter 4). Figures 2 (a) and (c) show output images of dithering with white noise.

Ordered dither [16, 127, 133] is a popular digital halftoning technique that can be defined by setting

$$s_{i,j} = 1/2 - (v_{(i \bmod \ell_1),(j \bmod \ell_2)} + 1/2)/\ell_1\ell_2, \tag{3}$$

where $v_{(i \bmod \ell_1),(j \bmod \ell_2)}$ are elements of an $\ell_1 \times \ell_2$ *dither matrix* Υ.

Figures 3 (a) and (c) feature two test image representations obtained by ordered dither with an 8×8 matrix from [111]:

$$\Upsilon = \begin{pmatrix} 0 & 32 & 8 & 40 & 2 & 34 & 10 & 42 \\ 48 & 16 & 56 & 24 & 50 & 18 & 58 & 26 \\ 12 & 44 & 4 & 36 & 14 & 46 & 6 & 38 \\ 60 & 28 & 52 & 20 & 62 & 30 & 54 & 22 \\ 3 & 35 & 11 & 43 & 1 & 33 & 9 & 41 \\ 51 & 19 & 59 & 27 & 49 & 17 & 57 & 25 \\ 15 & 47 & 7 & 39 & 13 & 45 & 5 & 37 \\ 63 & 31 & 55 & 23 & 61 & 29 & 53 & 21 \end{pmatrix}. \tag{4}$$

Such dither matrices were popularized by Bayer [16] and subsequently found to be a subset of those produced by the method of recursive tesselation [219].

Mitsa and Parker [147] used Ulichney's concept of *blue noise* [218], which is going to be discussed in detail in the next section, to design dither matrices they called *blue noise masks* (these matrices are also known as *stochastic screens* [37]). Other approaches to blue noise mask generation were proposed by Ulichney [221] (the popular *void-and-cluster* method) and other researchers [129, 130, 199, 243]. Images in Figures 4 (a) and (c) were obtained by ordered dither with a 128×128 blue noise mask generated using the void-and-cluster method. The method's internal parameter $\sigma = 1.5$, as recommended by Ulichney.

An interesting generalization of ordered dither is called *look-up-table (LUT) based halftoning* [125, 209, 229]. In LUT based halftoning, the interval $[0, 1]$ is divided into non-intersecting subintervals, each of which is associated with an $\ell_1 \times \ell_2$ matrix of zeros and ones called a *binary pattern*, or a *dot profile*. Whenever $g_{i,j}$ is within a certain subinterval, $b_{i,j}$ is the element in position $((i \bmod \ell_1), (j \bmod \ell_2))$ in the corresponding binary pattern. Suppose that $g_{i,j} < g_{i',j'}$ for some
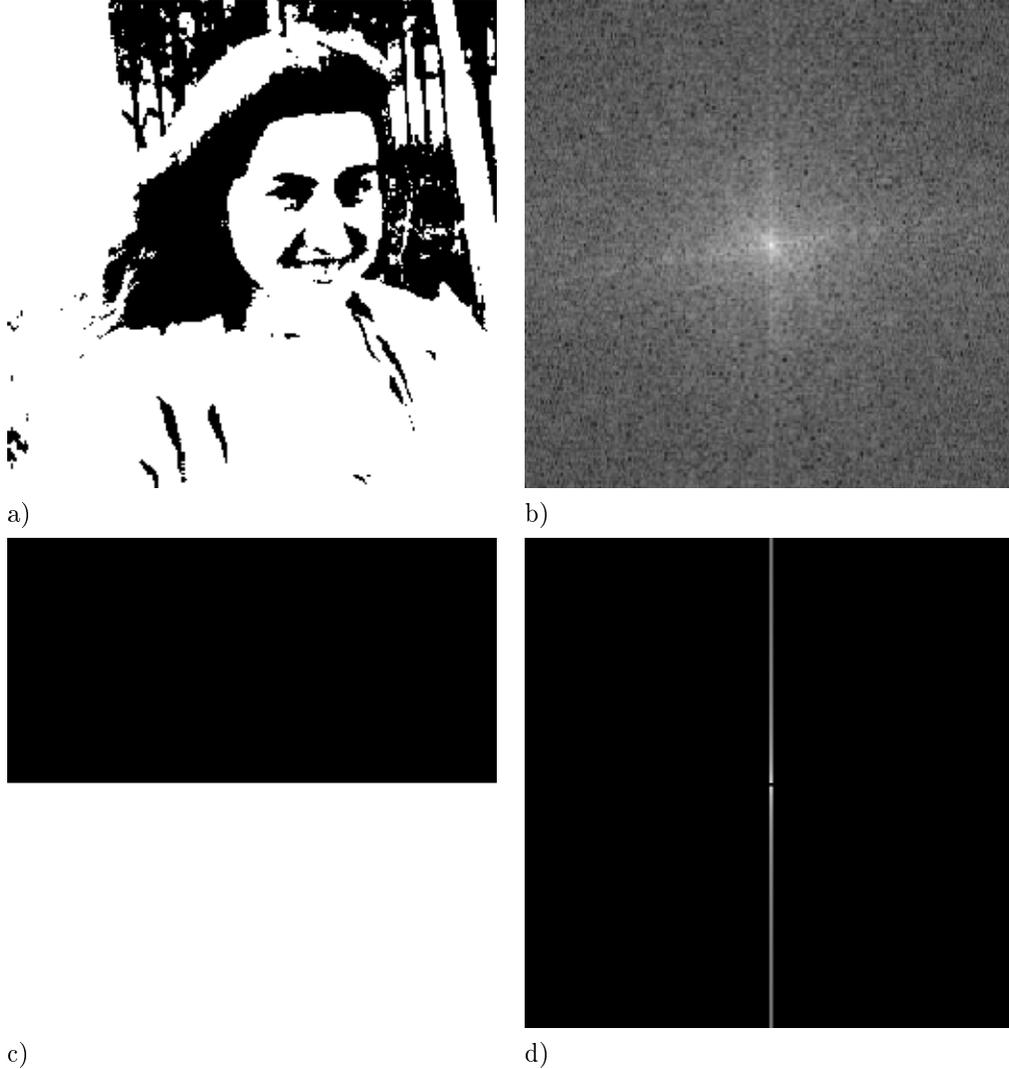
Fig. 1. Quantization with a fixed threshold ($s = 0$):
Halftone representations of test images (left);
the magnitude spectra of the corresponding noise images (right).
a) Portrait of Anya Pogosyants
b) Magnitude spectrum of the noise image (min $= 0.17$, max $= 8.5$)
c) Gray scale ramp
d) Magnitude spectrum of the noise image (min $= 0$, max $= 9.2$)

(i, j), (i', j'), such that $(i \bmod \ell_1) = (i' \bmod \ell_1)$ and $(j \bmod \ell_2) = (j' \bmod \ell_2)$. In LUT based halftoning, $b_{i,j} = 1$ does not have to imply $b_{i',j'} = 1$, and, similarly, $b_{i',j'} = 0$ does not have to imply $b_{i,j} = 0$. In other words, the *stacking constraint* inherent to ordered dither can be relaxed, and this is what makes LUT based halftoning more general. (Wash and Hamilton [226] showed that ordered dither can be performed using look-up tables, but they did not violate the stacking constraint.)

The difference

$$\epsilon_{i,j} = a_{i,j} - b_{i,j} \tag{5}$$

is commonly called the *quantization error* [57], *binary quantizer error* [77], or simply *error* [20, 111,

4
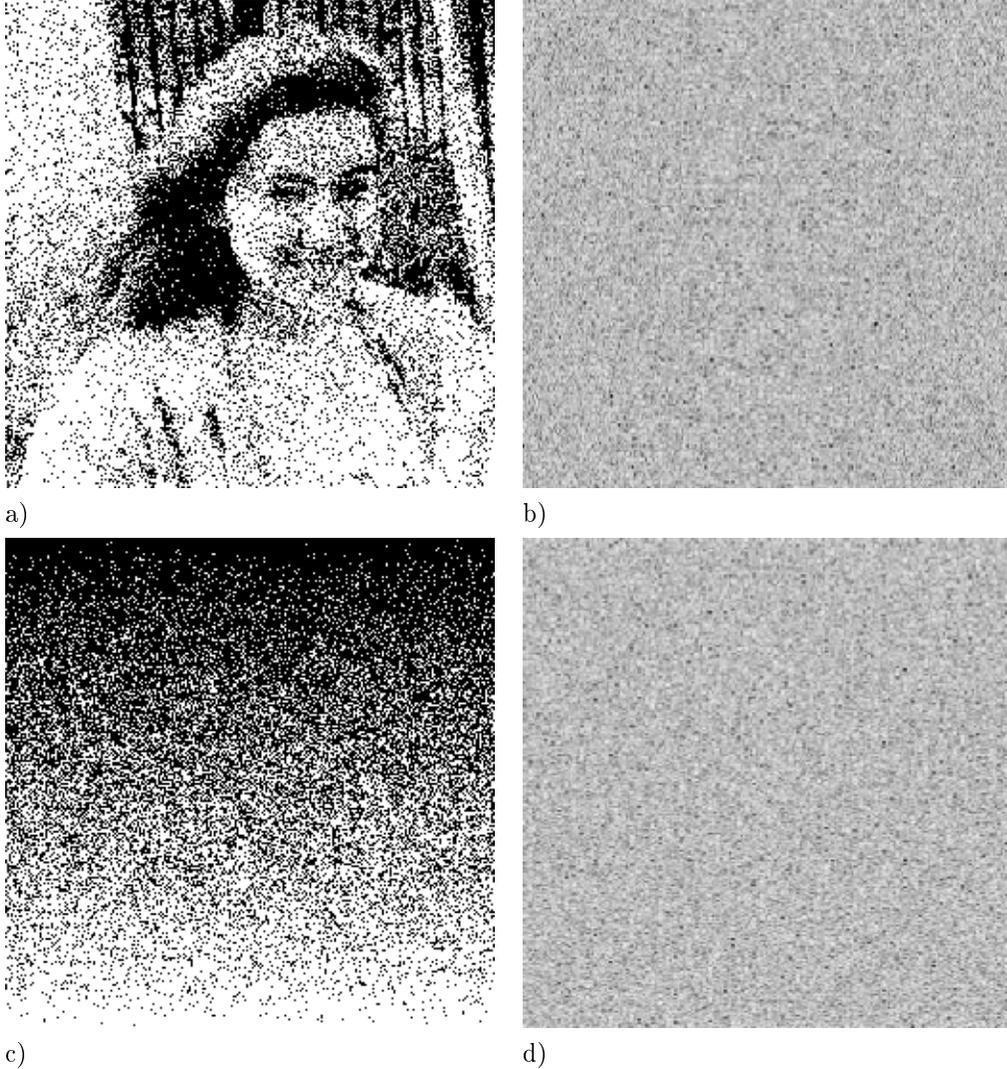
Fig. 2. Dithering with white noise:
   Halftone representations of test images (left);
   the magnitude spectra of the corresponding noise images (right).
      a) Portrait of Anya Pogosyants
      b) Magnitude spectrum of the noise image (min = 0.56, max = 5.7)
      c) Gray scale ramp
      d) Magnitude spectrum of the noise image (min = 0.42, max = 5.8)

218]. Knox [108] introduced the term *error image* meaning a visual representation of an $N_1 \times N_2$ matrix with elements equal to $-\epsilon_{i,j}$, $i = 0, 1, \ldots, N_1 - 1$, $j = 0, 1, \ldots, N_2 - 1$. (He defined the "error" as $b_{i,j} - a_{i,j}$, which makes sense but contradicts the established tradition.) Following [20, 57], we shall call

$$e_{i,j} = b_{i,j} - g_{i,j} \qquad (6)$$

the *quantization noise*, or just the *noise*. The visual representation of an $N_1 \times N_2$ matrix of $e_{i,j}$ would then become a *noise image* (Dalton [37] used this term with a different meaning). The reader should beware of cases when other meanings are assigned to "quantization error" and/or "quantization noise" [68, 77, 185, 58, 56].

5
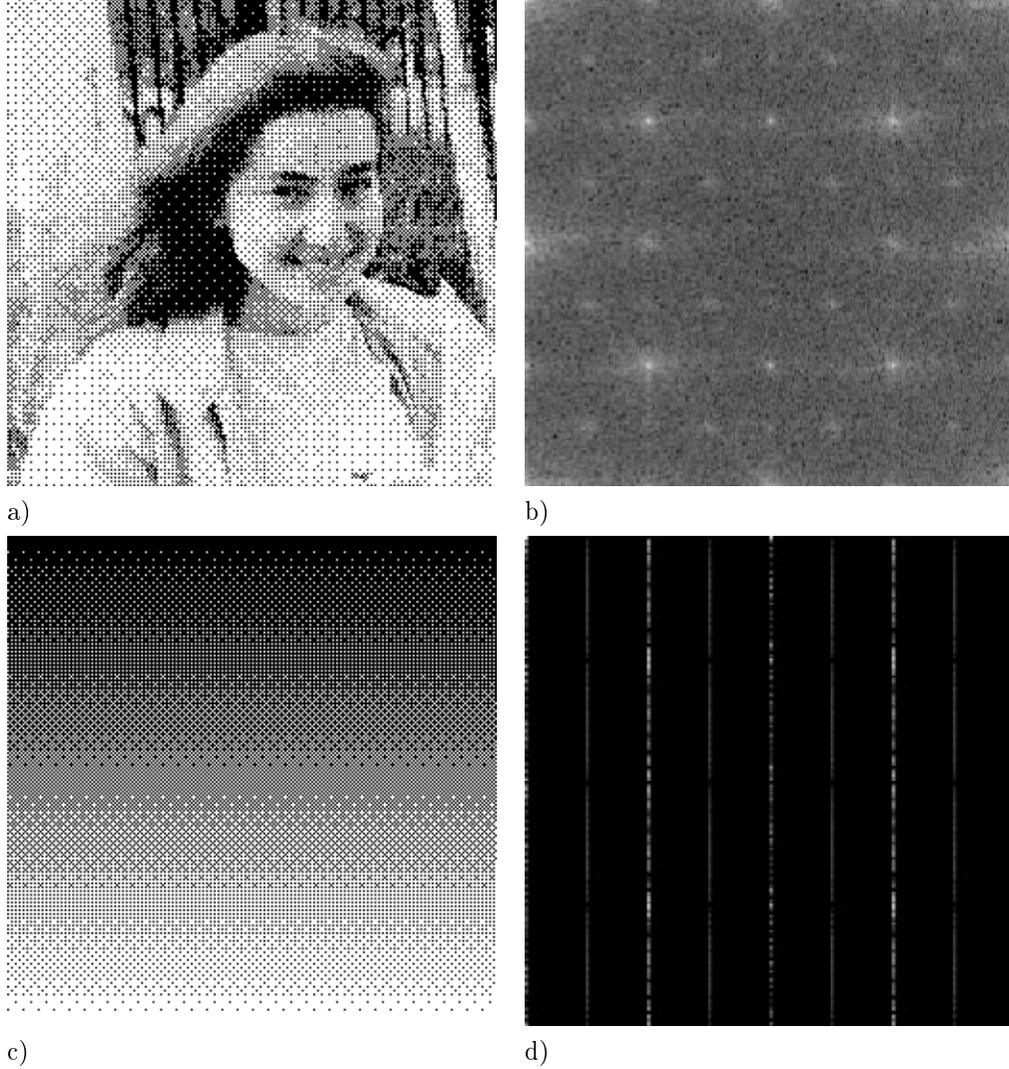
Fig. 3. Ordered dither with a recursive tesselation matrix (Eq. (4)):
        Halftone representations of test images (left);
        the magnitude spectra of the corresponding noise images (right).
            a) Portrait of Anya Pogosyants
            b) Magnitude spectrum of the noise image (min = 0.16, max = 9.5)
            c) Gray scale ramp
            d) Magnitude spectrum of the noise image (min = 0, max = 9.7)

Floyd and Steinberg [64, 65] proposed a digital halftoning technique called *error diffusion (ED)* (a similar but more complex method had been previously published by Schroeder [190]). In error diffusion, $s_{i,j}$ is a *sum of weighted errors,*

$$s_{i,j} = \sum_{\tau_1=0}^{\ell-1} \sum_{\tau_2=0}^{2(\ell-1)-\ell\delta_{\ell-1,\tau_1}} w_{\tau_1,\tau_2}\,\epsilon_{i-(\ell-1)+\tau_1,j-(\ell-1)+\tau_2}. \tag{7}$$

In the definition above,

$$\delta_{i,j} = \begin{cases} 0 & \text{if } i \neq j, \\ 1 & \text{if } i = j, \end{cases} \tag{8}$$
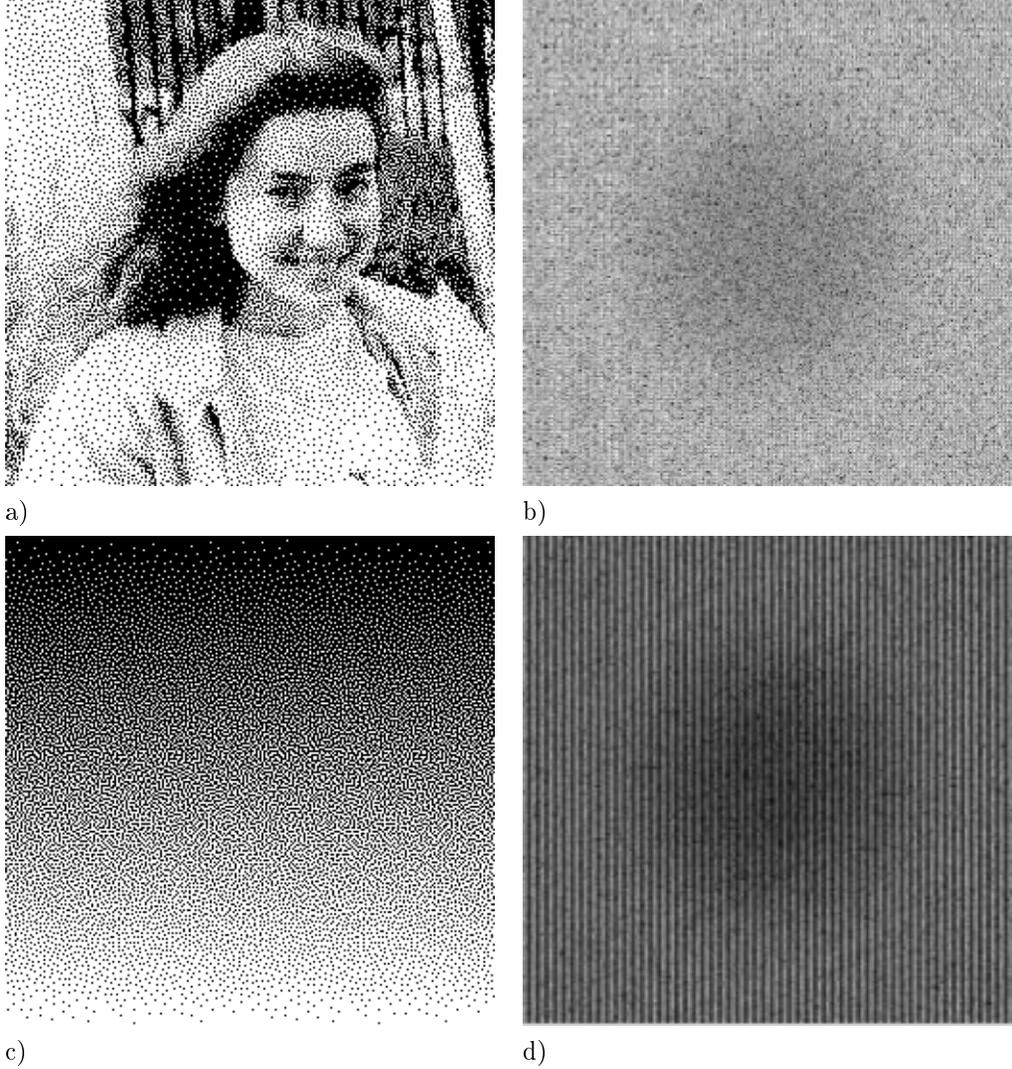
Fig. 4. Ordered dither with a blue noise mask (void-and-cluster):
Halftone representations of test images (left);
the magnitude spectra of the corresponding noise images (right).
 a) Portrait of Anya Pogosyants
 b) Magnitude spectrum of the noise image (min $= 0.14$, max $= 6.2$)
 c) Gray scale ramp
 d) Magnitude spectrum of the noise image (min $= 0$, max $= 6.4$)

is the Kronecker delta function, and w_{τ_1, τ_2} are *weights*, or *error diffusion coefficients*, elements of a wedge-shaped $\ell \times (2\ell - 1)$ matrix W, which is occasionally called the *error diffusion kernel* [233]. By W being "wedge-shaped" we mean that $w_{\ell-1, \tau_2} = 0$ for $\tau_2 = \ell - 1, \ell, \ell + 1, \ldots, 2(\ell - 1)$ (error diffusion algorithms are sometimes classified by the number of non-zero weights [218]). The outputs $b_{i,j}$ are computed line-by-line, from left to right, and the values of $\epsilon_{i,j}$ outside the image are assumed to be zeros. Figures 5 (a) and (c) show images produced by the *classical (four-weight) Floyd–Steinberg error diffusion algorithm* [65]: $\ell = 2$ and

$$W = \begin{pmatrix} 1/16 & 5/16 & 3/16 \\ 7/16 & \times & \end{pmatrix}, \tag{9}$$
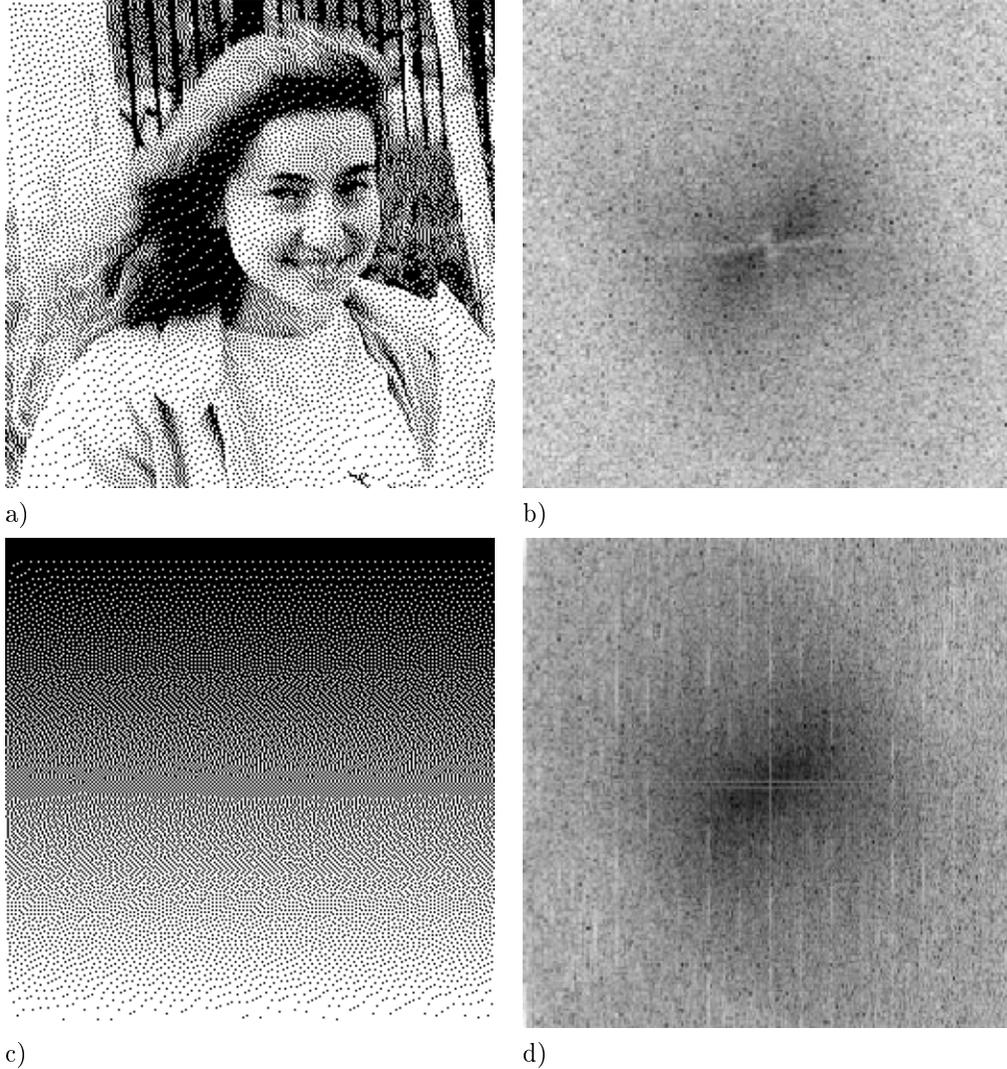
Fig. 5. Classical Floyd–Steinberg error diffusion (Eq. (9)):
Halftone representations of test images (left);
the magnitude spectra of the corresponding noise images (right).
a) Portrait of Anya Pogosyants
b) Magnitude spectrum of the noise image (min = 0.12, max = 6.0)
c) Gray scale ramp
d) Magnitude spectrum of the noise image (min = 0.15, max = 7.2)

where the symbol $\times$ indicates position of $w_{\ell-1,\ell-1}$.

Subsequent modifications of ED employed the following main approaches: design a different kernel W [56, 96, 218]; change the order in which the pixels are processed [34, 218, 224, 232, 253] (this usually involves a change of W as well; sometimes, features of other digital halftoning techniques are also incorporated [34, 253]); randomize W [113, 218]; make W input-dependent [48, 233, 234]; substitute a binary quantizer with a modulated and/or randomized threshold for the nearest-level one [18, 49, 51, 109, 184, 218]; combine error diffusion with another digital halftoning technique [18, 47, 53, 74, 111, 118, 184, 202]; add optimization based on a vision system model [113, 160, 163, 208]; design an iterative (multi-pass) technique based on error diffusion [162, 163]. Several important algorithms emerged.

Ulichney [218] (Chapter 8) studied *error diffusion on a serpentine raster*, also known as *serpentine error diffusion (SED)*. In this algorithm, the ouput image is also computed line-by-line, but pixels in the lines with odd numbers are processed right-to-left (pixels in the even-numbered lines are processed left-to-right, as usual). In SED,

$$s_{i,j} = \sum_{\tau_1=0}^{\ell-1} \sum_{\tau_2=0}^{2(\ell-1)-\ell\delta_{\ell-1,\tau_1}} w_{\tau_1,\tau_2} \epsilon_{i-(\ell-1)+\tau_1, j-(1-2(i \bmod 2))((\ell-1)-\tau_2)}. \tag{10}$$

Images produced by four-weight SED with

$$W = \begin{pmatrix} 3/16 & 5/16 & 1/16 \\ 7/16 & \times & \end{pmatrix}, \tag{11}$$

recommended by Ulichney, can be seen in Figures 6 (a) and (c).

Sandler et al. [184] explained the advantage of SED (unlike ordinary error diffusion, it allows each output pixel to depend on results of computations performed on all previously processed pixels without ℓ having to reach N_2) and considered SED with three deterministic non-zero weights instead of four. Figures 7 (a) and (c) display binary images produced using their

$$W = \begin{pmatrix} 10/38 & 14/38 & 0 \\ 14/38 & \times & \end{pmatrix}. \tag{12}$$

Ulichney [218] recommended *SED with 50% random weights*,

$$W(i,j) = \begin{pmatrix} 3/16 + \mathbf{r}_0(i,j) & 5/16 + \mathbf{r}_1(i,j) & 1/16 - \mathbf{r}_0(i,j) \\ 7/16 - \mathbf{r}_1(i,j) & \times & \end{pmatrix}, \tag{13}$$

where $\mathbf{r}_0(i,j)$ and $\mathbf{r}_1(i,j)$ are values of independent random variables uniformly distributed on $[-1/64, 1/64]$ and $[-5/64, 5/64]$ respectively. For brevity, we will refer to this technique as *randomized SED (RSED)*. Figures 8 (a) and (c) contain binary images produced by RSED.

Eschbach [47] combined error diffusion with another digital halftoning technique, *pulse-density modulation (PDM)*, first proposed in [50]. Halftone images produced by the resulting hybrid algorithm can be seen in Figures 9 (a) and (c). The areas where $1/4 < g_{i,j} < 3/4$ were treated by ED with W from Eq. (9), and the rest of the image was processed by PDM as follows. Summation of $g_{i,j}$ (dark areas) or $(1 - g_{i,j})$ (light areas) over diamond-shaped regions of the image was being performed; once the sum reached or exceeded 1, a pulse (1 or 0, respectively) was placed in the center of gravity of the current region. The error was then computed and diffused. Eschbach recommended use of ED to process regions touching the areas with $1/4 < g_{i,j} < 3/4$ as well, in order to break up the seams you can see at the switching points, Fig. 9 (c). However, this causes highly visible patches to appear in very light and very dark areas adjoining the switching points.

Eschbach [48] then tried error diffusion with

$$W = \begin{cases} \begin{pmatrix} 1/16 & 5/16 & 3/16 \\ 7/16 & \times & \end{pmatrix} & \text{if } \frac{40}{255} + \mathbf{r}_2(i,j) \leq g_{i,j} \leq \frac{215}{255} + \mathbf{r}_3(i,j), \\ \begin{pmatrix} 0 & 1/48 & 1/12 & 1/24 & 1/24 \\ 1/48 & 1/24 & 5/24 & 3/24 & 1/24 \\ 1/12 & 7/24 & \times & & \end{pmatrix} & \text{otherwise,} \end{cases} \tag{14}$$

where $\mathbf{r}_2(i,j)$ and $\mathbf{r}_3(i,j)$ are values of independent random variables uniformly distributed on $[-2/255, 2/255]$. Images produced by this algorithm are shown in Figures 10 (a) and (c).

Eschbach [49] proposed a more complex algorithm, error diffusion with threshold modulation based on a dynamic threshold imprint function. Figures 11 (a) and (c) feature images obtained by this technique (internal parameter $C = 40$).
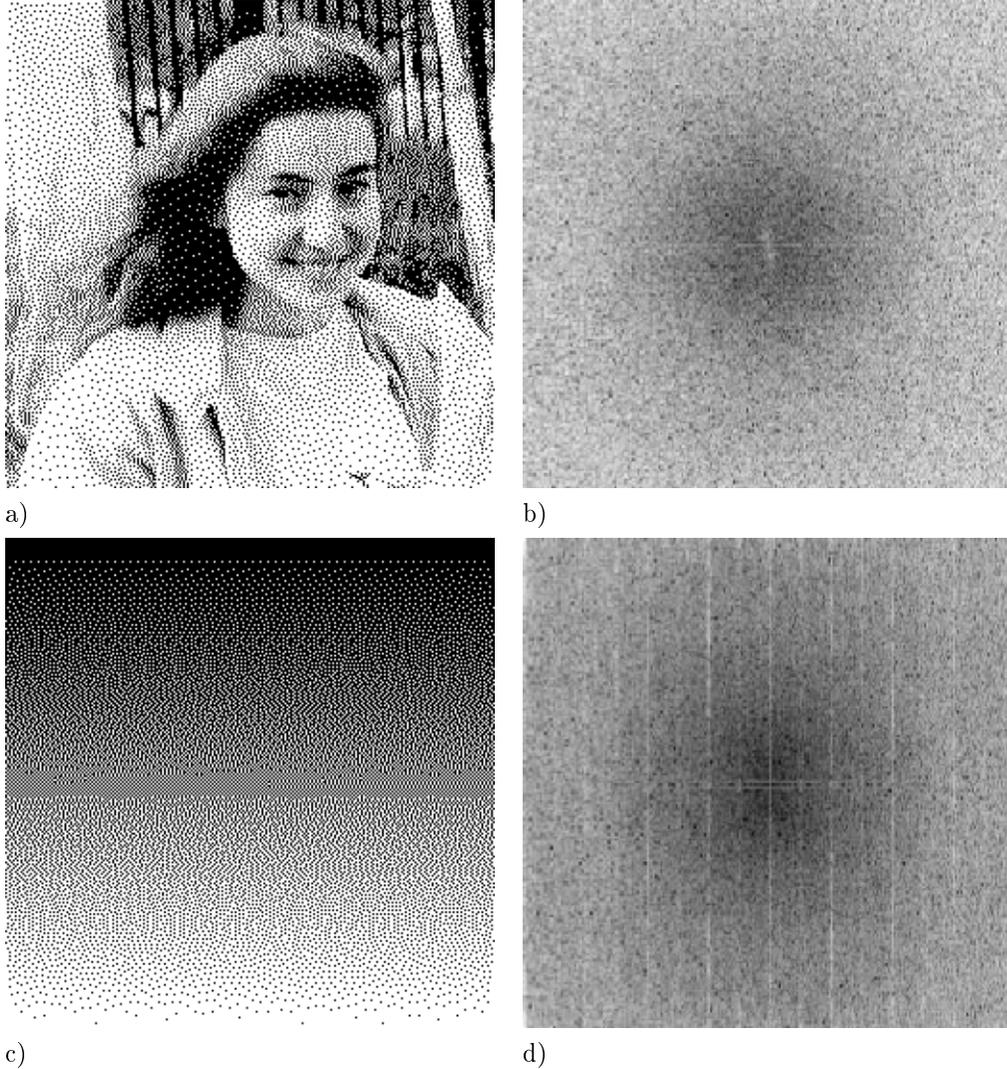
Fig. 6. Four-weight serpentine error diffusion, deterministic weights (Eq. (11)):
Halftone representations of test images (left);
the magnitude spectra of the corresponding noise images (right).
a) Portrait of Anya Pogosyants
b) Magnitude spectrum of the noise image (min = 0.27, max = 6.0)
c) Gray scale ramp
d) Magnitude spectrum of the noise image (min = 0.041, max = 7.5)

German physicists from the University of Essen have designed a number of interesting so-called *iterative algorithms* for digital halftoning — the iterative Fourier transform algorithm [22], threshold accepting [187], the iterative convolution algorithm (ICA) [248], gradient-controlled iterative convolution [249], and iterative wavelet transform algorithms [59, 60]. Figures 12 (a) and (c) represent test images halftoned by the iterative convolution algorithm of Zeggel and Bryngdahl (30 iterations; internal parameters $\Delta = 0.29$, $\delta = 0.005$, and $a = 0.4$).

Other digital halftoning algorithms employed patterning [82, 106, 169, 178] (this technique is also known as pulse-surface-area modulation, or PSAM [218]), neural networks [4, 7, 36, 70, 112, 196, 216, 217], direct binary search [3, 5, 126], least-squares model-based halftoning [160, 162, 163], simulated annealing [28], blockwise optimization [245], nonlinear programming [193], fractal

10

a)   b)

c)   d)
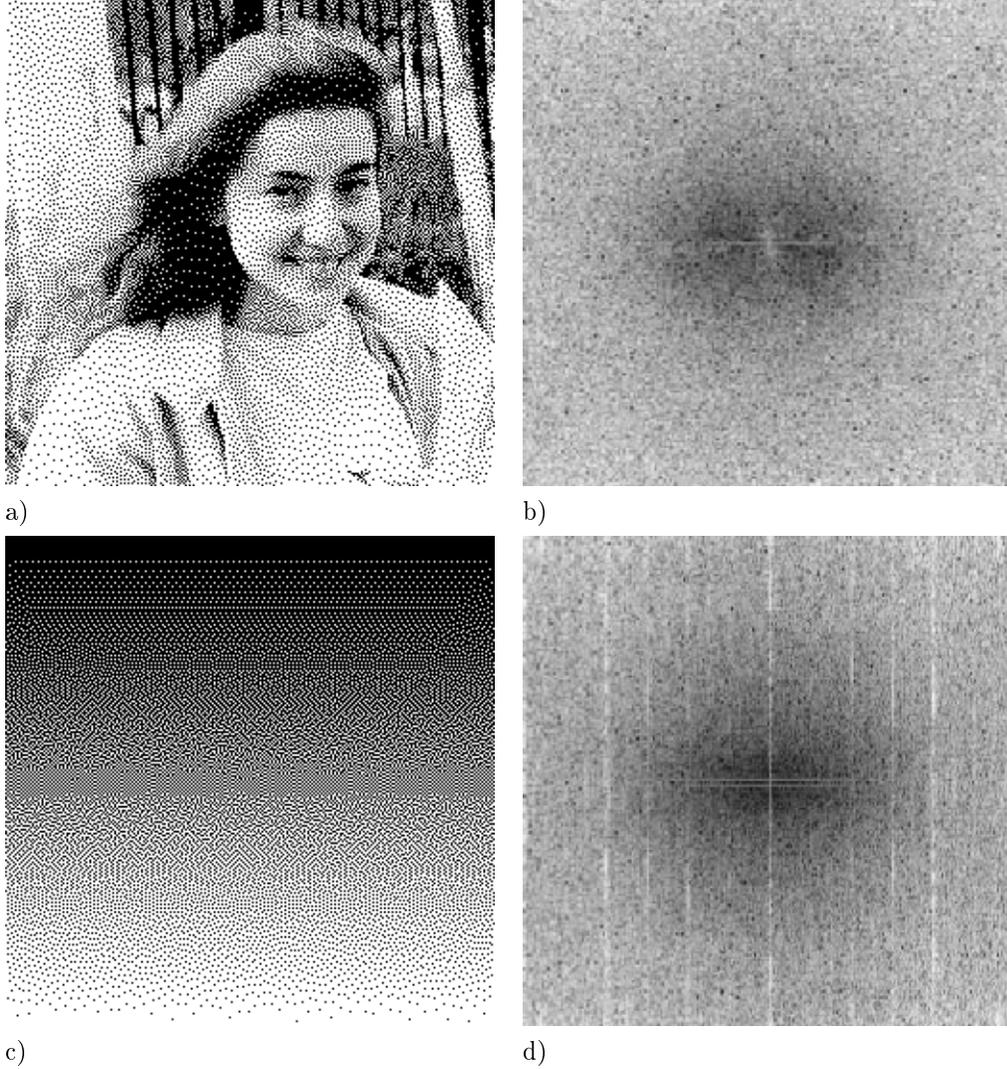
Fig. 7. Three-weight serpentine error diffusion, deterministic weights (Eq. (12)):
        Halftone representations of test images (left);
        the magnitude spectra of the corresponding noise images (right).
            a) Portrait of Anya Pogosyants
            b) Magnitude spectrum of the noise image (min = 0.39, max = 6.0)
            c) Gray scale ramp
            d) Magnitude spectrum of the noise image (min = 0.12, max = 6.6)

analysis [146], evolutionary computation (genetic algorithms) [121, 181], and fuzzy logic [90].

3. Halftone Image Quality Evaluation

No single technique of image quality evaluation has gained universal acceptance [35]. In this section, we will introduce some essential definitions and then consider different approaches to measurement of halftone image quality.

The *two-dimensional discrete Fourier transform (DFT)* $\mathbf{F}$ applied to an $N_1 \times N_2$ matrix X of elements $x_{j,k}$, $j = 0, 1, \ldots, N_1 - 1$, $k = 0, 1, \ldots, N_2 - 1$, produces an $N_1 \times N_2$ matrix $F = \mathbf{F}(X)$ consisting of elements

11
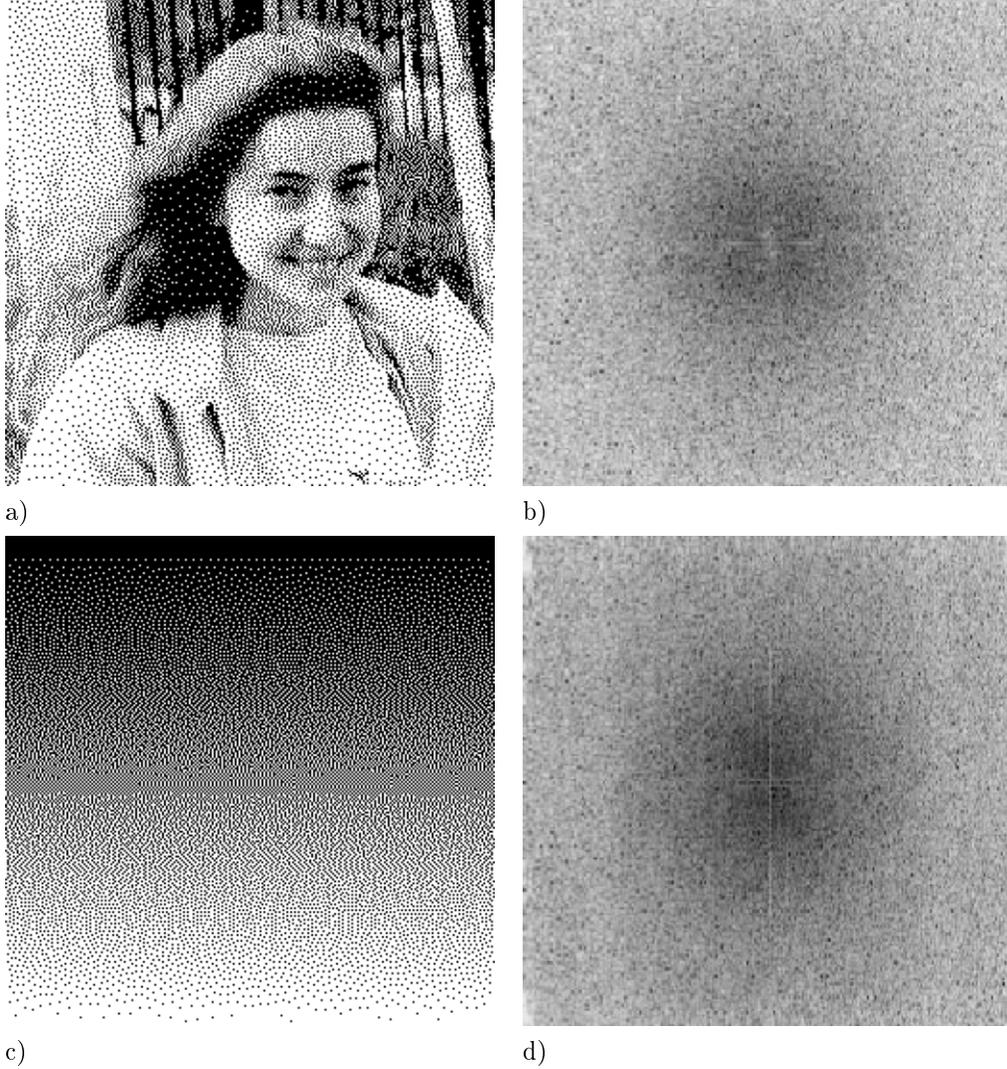
Fig. 8. Four-weight serpentine error diffusion, 50% random weights (Eq. (13)):
Halftone representations of test images (left);
the magnitude spectra of the corresponding noise images (right).
a) Portrait of Anya Pogosyants
b) Magnitude spectrum of the noise image (min = 0.26, max = 6.1)
c) Gray scale ramp
d) Magnitude spectrum of the noise image (min = 0.29, max = 6.8)

$$f_{u,v} = \mathbf{f}_X(u,v) = \sum_{j=0}^{N_1-1} \sum_{k=0}^{N_2-1} x_{j,k} \exp(-i2\pi(uj/N_1 + vk/N_2)), \tag{15}$$

where i denotes the square root of -1; u and v are called *spatial frequencies*. $F = \mathbf{F}(X)$ is sometimes called the *discrete Fourier spectrum* of X [20, 158].

The following paragraph is a quote from [172], p. 237.

"The two-dimensional Fourier transform of an image essentially is a Fourier series representation of a two-dimensional field. For the Fourier series representation to be valid, the field must be periodic. Thus... the original image must be considered to be periodic horizontally and vertically. The right side of the image therefore abuts the left side, and the top and bottom of the image are

12
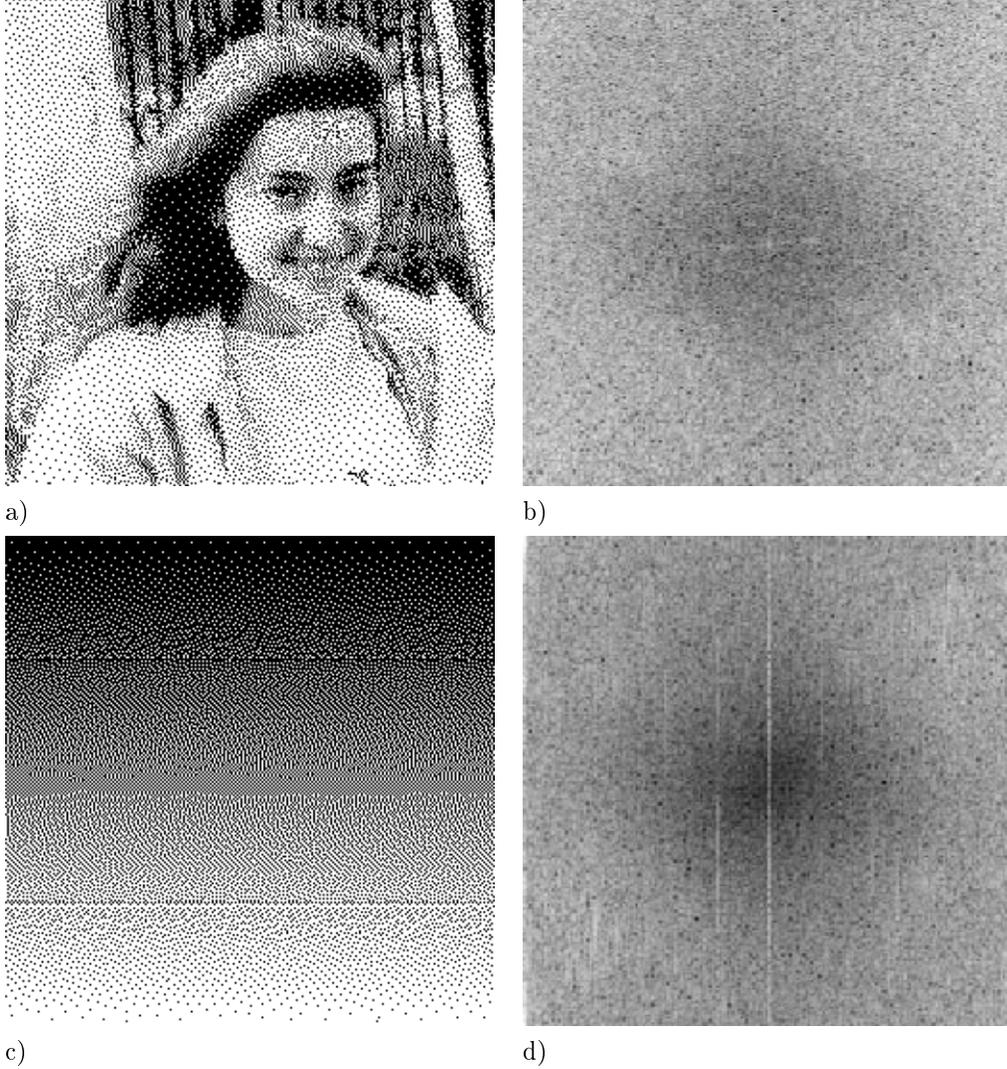
Fig. 9. Error diffusion combined with pulse-density modulation:
Halftone representations of test images (left);
the magnitude spectra of the corresponding noise images (right).
a) Portrait of Anya Pogosyants
b) Magnitude spectrum of the noise image (min = 0.35, max = 6.3)
c) Gray scale ramp
d) Magnitude spectrum of the noise image (min = 0.24, max = 7.2)

adjacent. Spatial frequencies along the coordinate axes of the transform plane arise from these transitions."

The *two-dimensional inverse discrete Fourier transform* $\mathbf{F}^{-1}$ yields $X = \mathbf{F}^{-1}(\mathbf{F}(X))$,

$$x_{j,k} = \mathbf{f}_F^{-1}(j, k) = \frac{1}{N_1 N_2} \sum_{u=0}^{N_1-1} \sum_{v=0}^{N_2-1} f_{u,v} \exp(i2\pi(uj/N_1 + vk/N_2)). \tag{16}$$

We will call the matrix $|\mathbf{F}(X)|$ consisting of

$$|\mathbf{f}_X(u, v)| = \sqrt{(\mathrm{Re}(f_{u,v}))^2 + (\mathrm{Im}(f_{u,v}))^2} \tag{17}$$

13
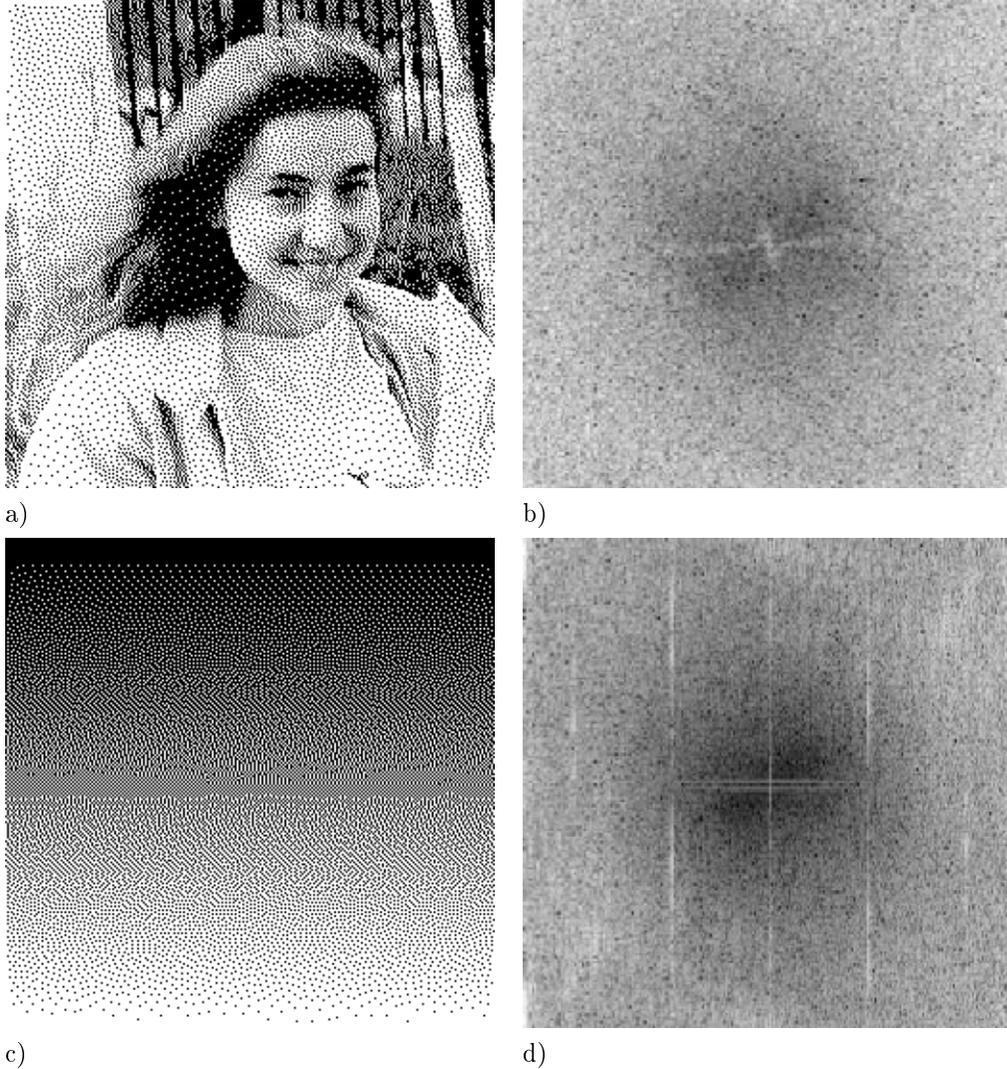
Fig. 10. Error diffusion with intensity-dependent weights (Eq. (14)):
Halftone representations of test images (left);
the magnitude spectra of the corresponding noise images (right).
a) Portrait of Anya Pogosyants
b) Magnitude spectrum of the noise image (min = 0.27, max = 6.1)
c) Gray scale ramp
d) Magnitude spectrum of the noise image (min = 0.27, max = 7.0)

the *two-dimensional discrete magnitude spectrum* of X. $\text{Re}(x)$ is the real part of x, $\text{Im}(x)$ is the imaginary part of x. (Gonzalez and Wintz [76] called $|\mathbf{F}(X)|$ the "discrete Fourier spectrum". The name "magnitude spectrum" is more common [158]. The name "amplitude spectrum" is occasionally used as a synonym of "magnitude spectrum" [158], but some authors assign a different meaning to it [69].) Components $|\mathbf{f}_X(u,v)|$ of the discrete magnitude spectrum will be referred to as *magnitudes* [158, 172] of the corresponding Fourier transform coefficients $f_{u,v}$ (some authors call $|\mathbf{f}_X(u,v)|$ *amplitudes*, Scheermesser and Bryngdahl [187] preferred the word *moduli*).

14

a)   b)

c)   d)
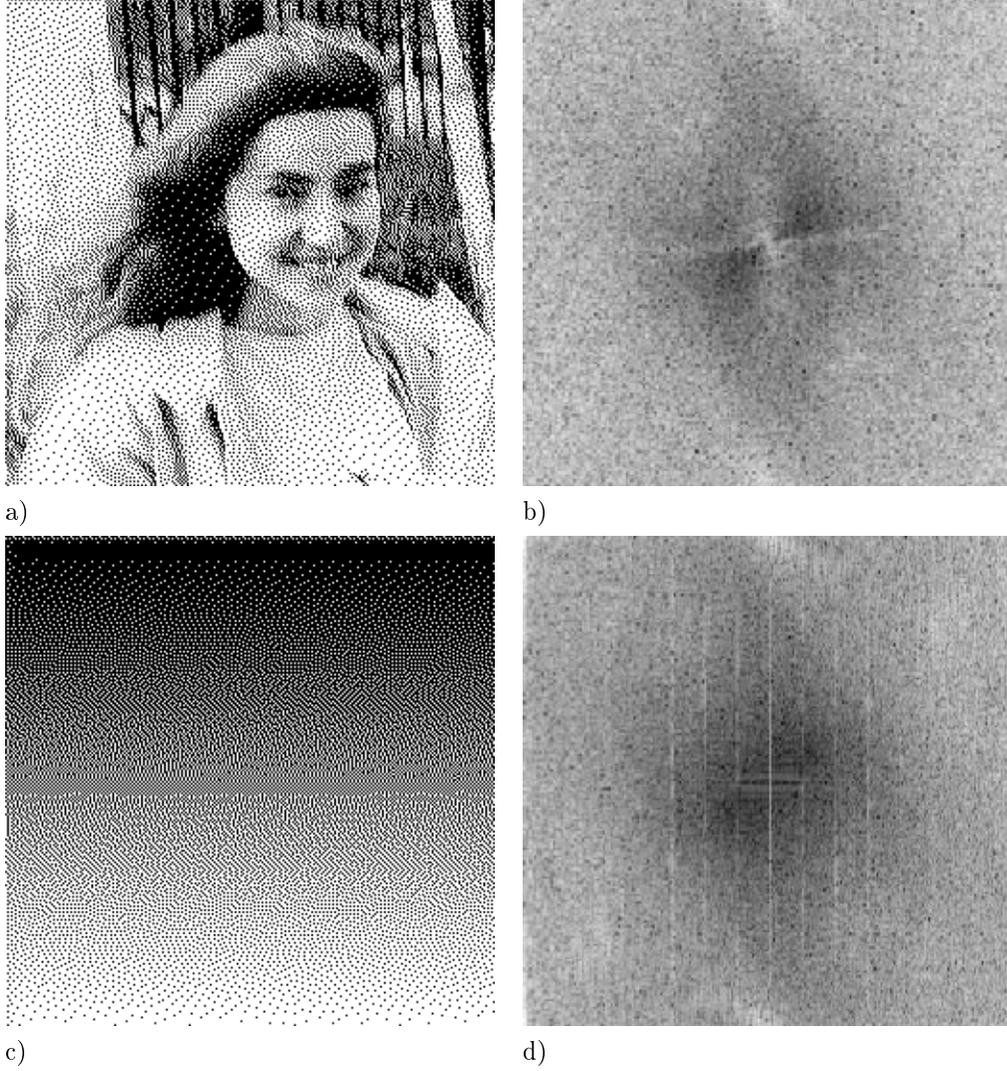
Fig. 11. Error diffusion with threshold modulation using threshold imprints:
Halftone representations of test images (left);
the magnitude spectra of the corresponding noise images (right).
    a) Portrait of Anya Pogosyants
    b) Magnitude spectrum of the noise image (min = 0.31, max = 6.3)
    c) Gray scale ramp
    d) Magnitude spectrum of the noise image (min = 0.08, max = 7.0)

Let

$$\text{tp}(x) = \arctan\left(\frac{\text{Im}(x)}{\text{Re}(x)}\right) - \frac{\pi}{2}\left(\text{sign}\left(\arctan\left(\frac{\text{Im}(x)}{\text{Re}(x)}\right)\right) - \left|\text{sign}\left(\arctan\left(\frac{\text{Im}(x)}{\text{Re}(x)}\right)\right)\right| + \right.$$

$$\left. \text{sign}\left(\text{Im}(x)\right) - \left|\text{sign}(\text{Im}(x))\right|\right), \tag{18}$$

where function arctan is the conventional arctangent function [46] expected to return its value in

15

a)   b)

c)   d)
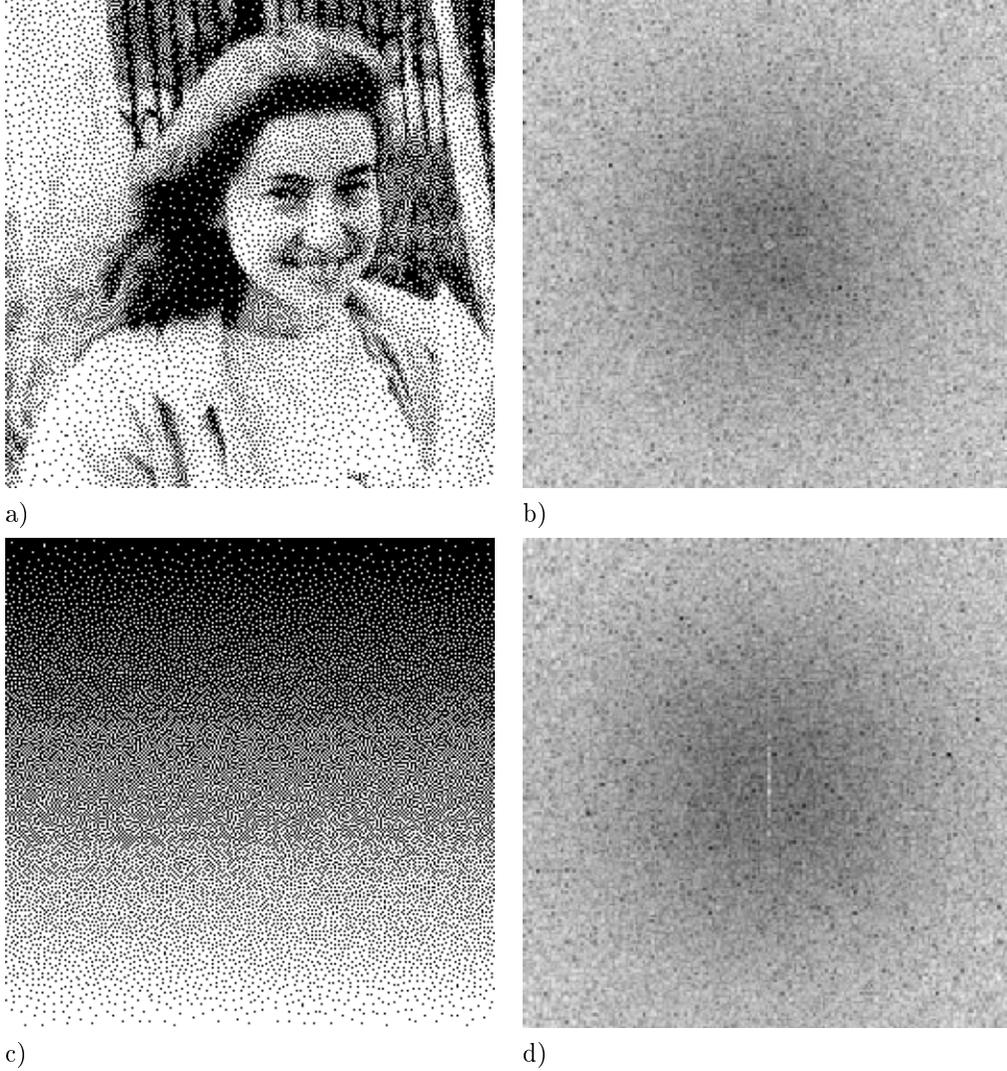
Fig. 12. The iterative convolution algorithm:
Halftone representations of test images (left);
the magnitude spectra of the corresponding noise images (right).
a) Portrait of Anya Pogosyants
b) Magnitude spectrum of the noise image (min = 0.27, max = 6.1)
c) Gray scale ramp
d) Magnitude spectrum of the noise image (min = 0.27, max = 6.3)

the radian measure, $\arctan(x) \in (-\frac{\pi}{2}, \frac{\pi}{2})$ for any real x, and

$$\text{sign}(x) = \begin{cases} 1 & \text{if } x > 0, \\ 0 & \text{if } x = 0, \\ -1 & \text{if } x < 0, \end{cases} \tag{19}$$

is the *signum function.*

$$\phi_X(u,v) = \begin{cases} 0 & \text{if } \operatorname{Re}(f_{u,v}) \geq 0 \text{ and } \operatorname{Im}(f_{u,v}) = 0, \\ \frac{\pi}{2} & \text{if } \operatorname{Re}(f_{u,v}) = 0 \text{ and } \operatorname{Im}(f_{u,v}) > 0, \\ \pi & \text{if } \operatorname{Re}(f_{u,v}) < 0 \text{ and } \operatorname{Im}(f_{u,v}) = 0, \\ \frac{3\pi}{2} & \text{if } \operatorname{Re}(f_{u,v}) = 0 \text{ and } \operatorname{Im}(f_{u,v}) < 0, \\ \operatorname{tp}(f_{u,v}) & \text{otherwise,} \end{cases} \tag{20}$$

are *phases* [76] of $f_{u,v}$. The phases lie in the interval $[0, 2\pi)$. The matrix of phases will be denoted $\Phi(X)$ and referred to as the *two-dimensional discrete phase spectrum* [158].

$$\mathbf{P}(X) = |\mathbf{F}(X)| \circ |\mathbf{F}(X)|, \tag{21}$$

where $\circ$ stands for direct (element-by-element) product of matrices, is the *two-dimensional discrete power spectrum* [158] of X. (Marple [137] prefers the term "periodogram". This choice has to do with the periodogram averaging technique often used to estimate power spectra of analog signals and images subjected to digital processing.)

Broja and Bryngdahl [20] called discrete Fourier spectra $\mathbf{F}(B - G)$ of the noise images the *quantization noise spectra*, or simply the *noise spectra*. However, they visualized only the corresponding magnitude spectra. Section 5 of this paper will cover color visualization of the noise spectra and the corresponding phase spectra.

We visualize the magnitude spectra of the noise images by representing

$$l_{u,v} = \ln(1 + |\mathbf{f}_{B-G}(u,v)|) \tag{22}$$

as grayscale values [76, 172] ranging from "black" $(\min\limits_{u,v} l_{u,v})$ to "white" $(\max\limits_{u,v} l_{u,v})$. Here ln stands for the natural logarithm. Other researchers [56, 246] used more general transformations of the type

$$l_{u,v} = \ln(1 + \beta \mathcal{N}(|\mathbf{f}_{B-G}(u,v)|))/\ln(1 + \beta), \tag{23}$$

where $\mathcal{N}$ is a linear normalization function such that its output is always in $[0, 1]$, and β is a constant between 4 and 70. The exact value of β is given by the user and depends on the spectrum that has to be visualized.

For the visualization purposes, the quadrants of the Fourier transform are rearranged to move the origin $((0,0)$, the dc component) to the center of the image in compliance with the standard practice [76, 172]. (In the previous sentence and the rest of the paper, the popular abbreviation *dc* stands for "direct current".) The origin shift is performed as follows. Whenever we are about to calculate $\mathbf{F}(X)$ (X is an $N_1 \times N_2$ matrix, as before), $F' = \mathbf{F}'(X)$ consisting of elements

$$f'_{u,v} = \mathbf{f}'_X(u,v) = \sum_{j=0}^{N_1-1} \sum_{k=0}^{N_2-1} (-1)^{j+k} x_{j,k} \exp(-i2\pi(uj/N_1 + vk/N_2)), \tag{24}$$

is computed instead. As a result, the low-frequency components are gathered near the center of the spectrum, and the high-frequency ones are moved away from the center. Then

$$x_{j,k} = \mathbf{f}_F^{-1}(j,k) = \frac{(-1)^{j+k}}{N_1 N_2} \sum_{u=0}^{N_1-1} \sum_{v=0}^{N_2-1} f'_{u,v} \exp(i2\pi(uj/N_1 + vk/N_2)). \tag{25}$$

Several authors [94, 157, 170, 210] have reported that the organization of image phase information appears far more critical to visual perception than the image properties measured by the power spectrum. In particular, if the phases of $\mathbf{f}_X(u,v)$ are randomized while the magnitudes stay the same, then the inverse Fourier transform may yield an image having little resemblance to X. Although the use of the magnitude spectra as means of image quality evaluation may appear to be limited due to these results (important information contained in the phases is being disregarded), one might argue that

$$B' = G + \mathbf{F}^{-1}(\mathcal{C}(\mathbf{F}(B - G))), \tag{26}$$

17

where $\mathcal{C}$ denotes a phase change operation, is not very likely to be binary.

Visual *textures* are defined as aggregates of image pixels or simple patterns [102], also known as *texels* [188]. Texels are not to be confused with *textons* [102], elongated blobs (e.g., rectangles, ellipses, or line segments) with a number of specific properties. Yellott [244] discovered very distinct binary textures that have identical Fourier power spectra and very similar statistical properties. Section 6 will provide new data on how relatively significant magnitudes and phases of the quantization noise images are.

Figures 1–12 (b) and (d) show grayscale representations of the magnitude spectra of the noise images for the image-algorithm combinations covered in Section 2. Color visualization of the noise spectra and the corresponding phase spectra will be covered in Section 5.

Allebach [2] pioneered evaluation and design of digital halftoning algorithms on the basis of *vision system models* in 1981. By then, important results had been obtained in a number of psychophysical experiments concerned with visual detectability of *gratings*. So-called *simple gratings* are two-dimensional patterns with the intensity function described by the expression

$$I(x, y) = I_0 + \mathcal{P}(2\pi f_0 \cdot (x \cos \theta - y \sin \theta)), \tag{27}$$

where I_0 is some constant intensity, $\mathcal{P}$ is a periodic function with period 1, f_0 is the fundamental frequency, and the bars of the grating are oriented at angle θ to the vertical y-axis. Note that sinusoidal gratings have very simple magnitude spectra, each consisting of two non-zero components symmetric with regard to the origin, once the quadrants are properly rearranged. The main parameters measured in the psychophysical detection experiments are known as two types of *contrast sensitivity* [183]. The physical *contrast* of simple images such as sinusoidal gratings or single patches of light on a uniform background is well defined and agrees with the perceived contrast, but this is not so for complex images [167]. *Contrast metrics* are extensively studied [72, 168, 214].

We are interested in numerical *distortion measures* $d_\mathcal{V}(G, B)$ for halftone image quality assessment ($\mathcal{V}$ in the subscript means that a measure may depend on the image viewing conditions; in the rest of the paper, this subscript will be dropped). The rest of the section is devoted to examination of different approaches to development of more or less meaningful distortion measures.

Campbell et al. [25, 26] showed that the contrast sensitivity depends on θ. The sensitivity is greatest and nearly equal for $\theta = 0°$ or $90°$ (vertical or horizontal gratings) and decreases monotonically to a minimum at $\theta = 45°$ where the sensitivity is about 3 dB less. Halftoning algorithms are known to take advantage of this fact by favoring diagonal correlated artifacts over horizontal and vertical ones. For this reason, we will be primarily interested in distortion measures that take this anisotropy into account, directly (by relying upon appropriate vision system models) or indirectly (by sufficiently asymmetric windows being involved in the process of their computation). (Numerous techniques of image quality evaluation assuming radial symmetry of the vision system have been proposed and studied [17, 70, 81, 128, 135, 150, 153, 154, 212, 218, 227, 252].)

Let X be the input of a linear shift-invariant operator [94] representing a channel of the vision system, and let Y be this channel's output. Then the corresponding *modulation transfer function (MTF)* $\mathbf{H}$ can be defined [172] to be an $N_1 \times N_2$ matrix such that

$$|\mathbf{F}(Y)| = \mathbf{H} \circ |\mathbf{F}(X)|. \tag{28}$$

Components of $\mathbf{H}$ will be denoted by $\mathbf{h}(u, v)$. (Jain [95] gave a different definition of the MTF — he normalized it with regard to $\mathbf{h}(0, 0)$.)

Sakrison [183] proposed a multi-channel vision system model that would help to determine transmission rates (in bits/pixel) for visually lossless coding of images. In our case, however, the rate is fixed, so we would like to modify this model in order to obtain a meaningful distortion measure $d(G, B)$ based upon known properties of human vision. The results of this measure's

application must strongly correlate with those of subjective evaluation tests. (Techniques of subjective testing are discussed in [35, 123, 135, 147, 172, 183].)

First, let's compute $z_{j,k} = \varphi(G, B, j, k)$ for $j = 0, 1, \ldots, N_1 - 1$, $k = 0, 1, \ldots, N_2 - 1$ to account for ganglion cell adaptation to changing levels of background illumination, and let Z be the matrix of $z_{j,k}$. Sakrison [183] recommended

$$\varphi(G, B, j, k) = \varphi(g_{j,k}, b_{j,k}) = \lg(\mathcal{L}(b_{j,k})) - \lg(\mathcal{L}(g_{j,k})), \tag{29}$$

where lg stands for the logarithm base 10, and $\mathcal{L}$ is a transformation needed to express intensity in terms of *luminance*, i.e., luminous flux emitted per unit solid angle (steradian) and unit projected area of source [100], measured in candelas per m², cd/m²), thus accounting for the lighting conditions. Sakrison warned that the logarithmic approximation of the nonlinear part of the vision system is valid only if the values of $|\mathcal{L}(b_{j,k}) - \mathcal{L}(g_{j,k})|$ are small compared to $|\mathcal{L}(g_{j,k})|$. In other words, the vision system is assumed to be working in its *photopic region*, i.e., the image has to be well-lit for the model to work. There may be a need to modify the function $\varphi(G, B, j, k)$ in order to incorporate the influence of *gamma correction* [66] or its analog for printers, *tone scale adjustment (TSA)* [218], also known as *dot gain compensation* [41]. Roetling and Holladay [177] proposed the popular *dot-overlap model* as means of accounting for device distortions. It was then studied and modified by a number of researchers [203, 205]. Pappas et al. [163] showed that the dot overlap model can be inadequate for some printers and recommended direct photometric measurement. For laser printers, the output is known to depend on the toner level [184], which further complicates the process of tone scale adjustment. Generally, for devices unable to display G without resorting to halftoning, adjustment and verification of any vision system model remain complex tasks. We will discuss TSA some more in the next section. When no modification of $\varphi(G, B, j, k)$ can successfully compensate for the device distortions, other means of adding a device model should be considered.

Z becomes input to multiple channels with narrow-band modulation transfer functions $\mathbf{H}'_{\nu,\kappa}$ defined by their elements

$$\mathbf{h}'_{\nu,\kappa}(u, v) = \frac{\exp\{-2[(\tilde{\theta}(u, v) - \Theta_\kappa)/\Theta_1]^2\} + \exp\{-2[(\pi - |\tilde{\theta}(u, v) - \Theta_\kappa|)/\Theta_1]^2\}}{\sqrt{1 + [1.8(\tilde{\omega}_r(u, v) - \Omega_\nu)/\Omega_\nu]^2}}, \tag{30}$$

where Ω_ν (expressed in cycles/degree) are the *radial center frequencies* of the channels,

$$\Omega_\nu = 4.5 \cdot (3.5)^\nu, \quad \nu = 0, \pm 1, \pm 2, \ldots, \tag{31}$$

and Θ_κ are their *angular center frequencies*

$$\Theta_\kappa = \kappa\pi/9, \quad \kappa = 0, 1, \ldots, 8. \tag{32}$$

The *angular bandwidth* of each channel is $\pm\Theta_1/2$. The *radial bandwidths* are equal to $\pm\Omega_\nu/1.8$, $\nu = 0, \pm 1, \pm 2, \ldots$. Note that we allow $\mathbf{h}'_{\nu,\kappa}(u, v)$ to be non-zero outside the band, i.e., the channels overlap. Other researchers studied multi-channel models with non-overlapping (orthogonal) channels [150, 212]. Such models allow successful resolution of infinitely close frequencies near the band edges, contradicting the classical experimental results that led to development of the multi-channel concept in the first place [180].

In Eq. (30),

$$\tilde{\theta}(u, v) = \theta(u, v) - \frac{\pi}{2}(\mathrm{sign}(\theta(u, v)) - |\mathrm{sign}(\theta(u, v))|), \tag{33}$$

where

$$\theta(u, v) = \arctan(\omega_y(v)/\omega_x(u)), \tag{34}$$

$\omega_x(u)$ and $\omega_y(v)$ being *spatial frequencies expressed in cycles/degree*.

In Eq. (30),

$$\tilde{\omega}_r(u,v) = \frac{\omega_r(u,v)}{\mathbf{s}(\theta(u,v))}, \tag{35}$$

where

$$\omega_r(u,v) = \sqrt{([\omega_x(u)]^2 + [\omega_y(v)]^2)}, \tag{36}$$

and

$$\mathbf{s}(\theta(u,v)) = \frac{1-w}{2}\cos(4\theta(u,v)) + \frac{1+w}{2}. \tag{37}$$

In Eq. (37), $w = 0.7$ is a *symmetry parameter*. It was Daly [38], who first suggested that $\tilde{\omega}_r(u,v)$ is used (instead of $\omega_r(u,v)$), in order to account for the radial asymmetry of the system. He modified the earlier, simpler model of Mannos and Sakrison [135]. That model had a single linear shift-invariant channel. Daly excluded the nonlinear part that required computation of the cube root of luminance and made the MTF flat at low frequencies. Daly's approach was applied to introduce orientational dependency into other models. Kolpatzik and Bouman [113] used it to modify Näsänen's contrast sensitivity function [153] they took to be the MTF. Analoui and Allebach [5] did the same thing to an MTF derived from the data of Campbell, Carpenter, and Levinson [24].

For images subtending small angles,

$$\omega_x(u) \approx \frac{\pi\mu(u - N_1/2)}{180 N_1 \arctan(1/D)}, \tag{38}$$

$$\omega_y(v) \approx \frac{\pi\mu(v - N_2/2)}{180 N_2 \arctan(1/D)}, \tag{39}$$

where D is the *viewing distance*, expressed in inches (the *normal viewing distance* is usually taken to be 10 inches [209]), and μ dpi is the resolution of the image.

From

$$\max_{u,v}\omega_r(u,v) = \omega_r(0,0) \approx \frac{\pi\mu}{180\sqrt{2}\arctan(1/D)} \tag{40}$$

and

$$\min_{u+v>0}\omega_r(u,v) \approx \frac{\pi\mu}{180\max(N_1, N_2)\arctan(1/D)} \tag{41}$$

we can determine that the channels that really matter are those with

$$\left\lfloor 1 + \log_{3.5}\left(\frac{\pi\mu}{180\max(N_1, N_2)\arctan(1/D)}\right)\right\rfloor \le \nu \le \left\lceil\log_{3.5}\left(\frac{\pi\mu}{360\sqrt{2}\arctan(1/D)}\right)\right\rceil. \tag{42}$$

For a 256×256 image printed at 100 dpi and viewed at the normal viewing distance, Inequality (42) becomes $-2 \le \nu \le 2$, so 45 channels are involved. Figure 13 illustrates the shape of their MTFs (intensity is proportional to $\mathbf{h}'_{\nu,\kappa}(u,v)$).

For each channel,

$$F''_{\nu,\kappa} = \mathbf{H}'_{\nu,\kappa} \circ \mathbf{F}'(Z) \tag{43}$$

is calculated. Note that we could find $|\mathbf{f}'_Z(u,v)|$ and $\phi'_Z(u,v)$ by substituting $f'_{u,v}$ for $f_{u,v}$ in Eqs. (17) and (20), respectively. Then, from

$$Z'_{\nu,\kappa} = (z'_{\nu,\kappa}(u,v)) = \mathbf{H}'_{\nu,\kappa} \circ |\mathbf{F}'(Z)| \tag{44}$$

elements of $F''_{\nu,\kappa}$ could be obtained by the equation

$$f''_{\nu,\kappa}(u,v) = z'_{\nu,\kappa}(u,v)\cos(\phi'_Z(u,v)) + iz'_{\nu,\kappa}(u,v)\sin(\phi'_Z(u,v)). \tag{45}$$

20
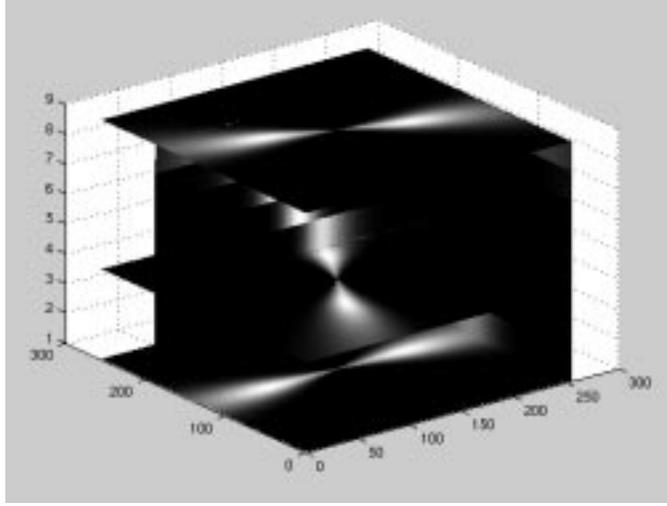
a)
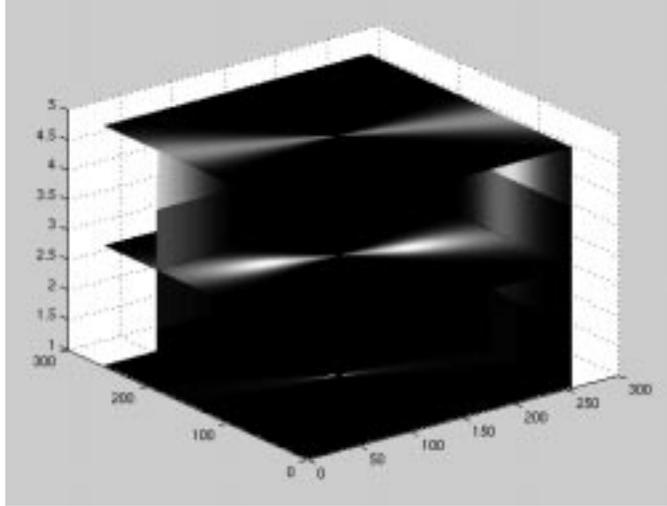
b)

Fig. 13. MTFs of linear shift-invariant channels in the modified Sakrison model:
a) Coordinate system with the axes $u + 1$, $v + 1$, $\kappa + 1$ ($\nu = 0$);
b) Coordinate system with the axes $u + 1$, $v + 1$, $\nu + 3$ ($\kappa = 8$).

Let $Z''_{\nu,\kappa}$ be matrices consisting of

$$z''_{\nu,\kappa}(j,k) = (-1)^{j+k} \mathbf{f}^{-1}_{F''_{\nu,\kappa}}(j,k). \tag{46}$$

The responses of the channels are

$$\mathbf{t}_{\nu,\kappa} = \sum_{j=0}^{N_1-1} \sum_{k=0}^{N_2-1} \left[\frac{z''_{\nu,\kappa}(j,k)}{s(j,k)} \right]^6, \tag{47}$$

where $s(j,k)$ are elements of $S(X)$, a matrix that describes how the decrease in noise stimulus sensitivity depends on the distance between the stimulus and a background patch with substantial gradient. One option offered by Sakrison is let

21

$$s(j,k) = \sqrt{\frac{1}{N_1 N_2} \sum_{x=0}^{N_1-1} \sum_{y=0}^{N_2-1} \left[\psi(x,y) \exp\left(\frac{4320(\ln 0.35)\arctan(1/D)}{\pi\mu} \sqrt{(j-x)^2 + (k-y)^2} \right) \right]^2},$$

<div align="right">(48)</div>

where $\psi(x,y)$ form a filtered version of G, the filter having a broad isotropic pass band through the midrange of spatial frequencies (say, $2.0 \div 20$ cycles/degree), with the absolute values of elements of its MTF increasing for a while with radial frequency to make $\psi(x,y)$ approximate the *magnitude of the gradient* of G. The other option is, set $s(j,k) = 1$ for all j, k, thus ignoring the background gradient problem altogether.

The Sakrison model involves thresholding $\mathbf{t}_{\nu,\kappa}$ and computing the logical OR of the outputs to determine if noise is detected. I have yet to find a function of $\mathbf{t}_{\nu,\kappa}$ that would be a good distortion measure $d(G,B)$, i.e. match results of subjective evaluation of halftone images. However, the Sakrison model is based on large volume of data gathered in multiple psychophysical experiments (see references in [183]), which makes it important, in my opinion. Hall and Hall [81] cited evidence in favor of placing a low-pass filter in front of the logarithmic part, which, in its turn, would be followed by a high-pass filter. Once orientational dependency is added to their model, an interesting alternative to the Sakrison model may emerge. More psychophysical data raising questions as to the site(s) and nature of the vision system nonlinearity have been published [42, 43, 152]. Given that the issue is closely related to the aforementioned studies of contrast in complex images, one should expect *models of pattern masking* like the one by Watson and Solomon [228], based on contrast gain control, to be incorporated into distortion measures in the future.

Bock et al. [19] proposed the so-called *distortion measure adapted to human perception (DMHP)* involving weighted multiplication of separate error assessments for edges, textures, and flat regions. Alas, this measure does not depend on the viewing conditions (lighting, resolution, viewing distance, etc.) — in particular, sizes of filters used to separate images into regions are expressed in pixels and fixed. Hosaka [88] and Eskicioglu [52] developed multidimensional measures of image quality based on quadtree decomposition of the original image into certain activity regions. Eskicioglu reported that his dc-shift-invariant measure captures notions like "blockiness" and "blurriness". Daly proposed an interesting technique for computation of so-called *difference maps* [39], which was later modified by Taylor et al. [211].

Ulichney [218] considered radially averaged power spectra of constant level representations. He defined *blue noise* as high-frequency noise with a flat radially averaged power spectrum, and postulated that "blue noise is pleasant". Ulichney's definition seemed too narrow to be adequate, so other researchers attempted to change it, adding more bias in favor of high frequencies [70, 113] and introducing orientational dependency otherwise ignored in the process of radial averaging [113]. Adding to the confusion, FS-1037C [223] defined blue noise as follows: "In a spectrum of frequencies, a region in which the spectral density, i.e., power per hertz, is proportional to the frequency". This means power density increase at the rate of 3dB per octave with increasing frequency. Risch [176] characterized *purple noise* by power density increasing 6dB per octave with increasing frequency (density proportional to the square of frequency). Lau, Arce, and Gallagher [122] defined *green noise* to be "the mid-frequency component of white noise" and studied green noise digital halftoning. An earlier alternative definition of green noise [231] describes "supposedly the background noise of the world" with the power spectrum averaged over several outdoor sites. This version of green noise is similar to *pink noise*, power density of which decreases 3dB per octave with increasing frequency (density proportional to 1/f) over a finite frequency range which does not include the dc component, but an extra hump is added around 500Hz. I propose that the name *violet noise* is given to a spectral region where the spectral density increases with increasing (radial) frequency. This would give us a convenient general definition incorporating purple noise, blue noise

of FS-1037C, modified blue noise from [113], parts of modified blue noise from [70], but not blue noise as defined by Ulichney, or green noise. Ample experimental evidence suggests that good halftoning algorithms produce radially asymmetric violet noise, possibly with flat spectrum parts included. The reverse is not necessarily true (some violet noise algorithms may produce pictures that aren't even binary, and others may render images poorly because of bad phase properties).

Perhaps, the most famous distortion measure used in image quality evaluation is the *mean-square error (MSE)*, often estimated by the formula

$$\mathcal{E} = \frac{1}{N_1 N_2} \sum_{j=0}^{N_1-1} \sum_{k=0}^{N_2-1} e_{j,k}^2. \tag{49}$$

One can estimate the *normalized mean-square error (NMSE)* by computing

$$\mathcal{E}_{\mathcal{N}} = \frac{\sum_{j=0}^{N_1-1} \sum_{k=0}^{N_2-1} e_{j,k}^2}{\sum_{j=0}^{N_1-1} \sum_{k=0}^{N_2-1} g_{j,k}^2}. \tag{50}$$

In many applications the MSE is expressed in terms of a *signal-to-noise ratio (SNR)*, several different definitions of which are known [35, 76, 95, 172]. The MSE is well-known to be incompatible with human sensory perception [6, 103, 135, 136], and explanations of this fact exist [172, 185]. Still, the MSE (SNR) is often used because of its simplicity, and because it is possible to calculate the rate-distortion function and simulate the optimum encoding scheme for it [135].

The *point-transformed mean-square error (PMSE)* [172] is

$$\mathcal{E}_{\mathcal{T}} = \frac{\sum_{j=0}^{N_1-1} \sum_{k=0}^{N_2-1} [\mathcal{T}(b_{j,k}) - \mathcal{T}(g_{j,k})]^2}{\sum_{j=0}^{N_1-1} \sum_{k=0}^{N_2-1} [\mathcal{T}(g_{j,k})]^2}, \tag{51}$$

where $\mathcal{T}$ may stand for a power law transformation of the type $\mathcal{T}(x) = x^{c_0}$, or a logarithmic transformation of the type $\mathcal{T}(x) = c_1 \log_b(c_2 + c_3 x)$, where b is the base of the logarithm, and c_i are constants, $i = 0, 1, 2, 3$.

The *Laplacian mean-square error (LMSE)* [172] is

$$\mathcal{E}_{\mathcal{T}'} = \frac{\sum_{j=1}^{N_1-2} \sum_{k=1}^{N_2-2} [\mathcal{T}'(b_{j,k}) - \mathcal{T}'(g_{j,k})]^2}{\sum_{j=1}^{N_1-2} \sum_{k=1}^{N_2-2} [\mathcal{T}'(g_{j,k})]^2}, \tag{52}$$

where

$$\mathcal{T}'(x_{j,k}) = x_{j+1,k} + x_{j-1,k} + x_{j,k+1} + x_{j,k-1} - 4x_{j,k} \tag{53}$$

is the Laplacian edge-sharpening operator.

The *convolution mean-square error (CMSE)* [172] is a generalization of the LMSE where $\mathcal{T}'$ stands for taking elements of the matrix obtained by convolution of an image and some linear shift-invariant filter, and the ranges of summation depend on the filter dimensions as well as the image ones. Mannos and Sakrison [135] tried the *frequency-weighted PMSE* (their single-channel model used to introduce pixelwise nonlinearity and perform frequency weighting has already been mentioned above).

Marmolin [136] tried several measures of the form

$$\mathcal{E}_{\mathcal{T}''} = \left[\frac{1}{N_1 N_2} \sum_{j=0}^{N_1-1} \sum_{k=0}^{N_2-1} |c_{j,k} \mathcal{T}''(e_{j,k})|^c \right]^{1/c}, \tag{54}$$

with limited success.

Katsavounidis and Kuo [103] proposed to compute the *generalized MSE (GMSE)* as a weighted sum of elements of the *MSE vector*. For the case of $N_1 = N_2 = N = 2^r$, where r is a non-negative integer, they defined these elements to be

$$\mathcal{E}_i = \sum_{j=0}^{2^i-1} \sum_{k=0}^{2^i-1} \left[\sum_{x=0}^{2^{r-i}-1} \sum_{y=0}^{2^{r-i}-1} b_{j \cdot 2^{r-i}+x, k \cdot 2^{r-i}+y} - \sum_{x=0}^{2^{r-i}-1} \sum_{y=0}^{2^{r-i}-1} g_{j \cdot 2^{r-i}+x, k \cdot 2^{r-i}+y} \right]^2, \tag{55}$$

for $i = 0, \ldots, r$. Note that $\mathcal{E}_r = N^2 \mathcal{E}$. No suggestion as to the exact values of weights has been made.

Matsumoto and Liu [138] proposed a metric they called *edge correlation*,

$$\hat{\rho}_e = \frac{1}{N_1(N_2 - 1)} \sum_{j=0}^{N_1-1} \sum_{k=0}^{N_2-2} (g_{j,k+1} - g_{j,k})(b_{j,k+1} - b_{j,k}) +$$

$$\frac{1}{(N_1 - 1)N_2} \sum_{j=0}^{N_1-2} \sum_{k=0}^{N_2-1} (g_{j+1,k} - g_{j,k})(b_{j+1,k} - b_{j,k}). \tag{56}$$

(Larger values of $\hat{\rho}_e$ are supposed to indicate **better** rendition of edges!)

Mitsa [145] studied *maximum local error*. For the case of $N_1 = 5n_1$, $N_2 = 5n_2$, where n_1 and n_2 are some positive integers, this distortion measure can be computed by the formula

$$\Lambda_{\mathcal{A}} = \max_{\substack{j=0,\ldots,n_1-1 \\ k=0,\ldots,n_2-1}} \sqrt{\frac{1}{25} \sum_{x=0}^{4} \sum_{y=0}^{4} \left[\frac{e_{5j+x,5k+y}}{\exp(0.025\mathcal{A}(5j+x, 5k+y))} \right]^2}, \tag{57}$$

where

$$\mathcal{A}(j,k) = \sum_{x=-1+\delta_{j,0}-\delta_{j,N_1-1}}^{1+\delta_{j,0}-\delta_{j,N_1-1}} \sum_{y=-1+\delta_{k,0}-\delta_{k,N_2-1}}^{1+\delta_{k,0}-\delta_{k,N_2-1}} \left| g_{j+x,k+y} - \right.$$

$$\left. \frac{1}{9} \sum_{x'=-1+\delta_{j+x,0}-\delta_{j+x,N_1-1}}^{1+\delta_{j+x,0}-\delta_{j+x,N_1-1}} \sum_{y'=-1+\delta_{k+y,0}-\delta_{k+y,N_2-1}}^{1+\delta_{k+y,0}-\delta_{k+y,N_2-1}} g_{j+x+x',k+y+y'} \right| \tag{58}$$

is a *local activity measure*.

Thurnhofer and Mitra [213] recommended the *weighted MSE (WMSE)*

$$\mathcal{E}_{\mathcal{A}} = \frac{1}{N_1 N_2} \sum_{j=0}^{N_1-1} \sum_{k=0}^{N_2-1} \left[\frac{e_{i,j}}{\exp(0.025\mathcal{A}(j,k))} \right]^2 \tag{59}$$

and the well-known statistical estimate of the *correlation coefficient*,

$$\hat{\rho}_{G,B} = \frac{\sum_{j=0}^{N_1-1} \sum_{k=0}^{N_2-1} (g_{j,k} - \bar{g})(b_{j,k} - \bar{b})}{\sqrt{\sum_{j=0}^{N_1-1} \sum_{k=0}^{N_2-1} (g_{j,k} - \bar{g})^2 \sum_{j=0}^{N_1-1} \sum_{k=0}^{N_2-1} (b_{j,k} - \bar{b})^2}}, \tag{60}$$

where

$$\bar{g} = \frac{1}{N_1 N_2} \sum_{j=0}^{N_1-1} \sum_{k=0}^{N_2-1} g_{j,k} \tag{61}$$

and

$$\bar{b} = \frac{1}{N_1 N_2} \sum_{j=0}^{N_1-1} \sum_{k=0}^{N_2-1} b_{j,k} \tag{62}$$

are the sample means of G and B, respectively. (Higher $\hat{\rho}_{G,B}$ is expected to mean **better** halftoning!)

None of the distortion measures $d(G, B)$ given by Eqs. (49–52, 57, 59) or derived from Eqs. (56, 60), say, by inverting the signs of the metrics, or in a similar fashion, depends on the image viewing conditions, so one should not expect these metrics to correlate with the subjective evaluation results consistently. Comparative study of distortion measures is beyond the scope of this paper.

Sandler et al. [184, 186] proposed to interpret outputs $b_{j,k}$ of a digital halftoning algorithm as values of random variables $\xi_{j,k}$ (Ulichney [218] (Section 3.2) did it earlier for the case of constant level input). Using this interpretation, Sandler et al. [184] developed the following *local quasi-optimality criterion*. Let S be an area of the image, consisting of pixels that are close together (no exact measure of "closeness" specified), and let $T(S)$ be the set of all possible two-element subsets $\{(j_1, k_1), (j_2, k_2)\}$ of S. Let the covariance of ξ_{j_1,k_1} and ξ_{j_2,k_2} be denoted by $\mathrm{cov}(\xi_{j_1,k_1}, \xi_{j_2,k_2})$. Sandler et al. postulated that it is desirable to construct $\xi_{j,k}$ so that the variance

$$V(\sum_S \xi_{j,k}) = \sum_S V(\xi_{j,k}) + 2 \sum_{T(S)} \mathrm{cov}(\xi_{j_1,k_1}, \xi_{j_2,k_2}) \tag{63}$$

is minimum on the condition that the expected values

$$E(\xi_{j,k}) = g_{j,k} \tag{64}$$

for all (j, k) in S.

Ulichney claimed that Eq. (64) (Eq. (3.27) in [218]) is always true in the case of constant level input for halftone processes which do not produce output by thresholding with a deterministic, periodic threshold array. However, it is straightforward to design a counterexample algorithm that cannot be described in terms of ordered dither. Moreover, statistical measurements discussed in Section 6 will show that error diffusion can be considered a counterexample, due to boundary effects.

The authors of the local quasi-optimality criterion pointed out that the underlying assumption that the vision system averages intensity levels of pixels in S with equal weights is just an approximation. For the purposes of digital halftoning algorithm design, they suggested that, "the closer together any two pixels are, the less correlated the corresponding random variables should be (on the condition that their expected values coincide with the inputs)." Radial anisotropy of the vision system can be accounted for by picking a measure of closeness based on non-Euclidean distance. For any given pair of pixels, significance of correlation between the random variables depends on the viewing conditions.

The approach of Sandler et al. fits the results of psychovisual experiments conducted by Burgess et al. [23] and Myers et al. [151]. According to these results, the human observer is strongly influenced by correlated noise, and the detection performance for even a simple task is degraded substantially in its presence. As Myers and Barrett [150] put it, "the human observer acts approximately as an ideal observer who does not have the ability to prewhiten the noise" (the notion of blue noise was not known to them).

A new class of digital halftoning algorithms based on the anti-correlation approach is introduced in the next section.

4. Digital Halftoning by Generalized Russian Roulette

Russian roulette is a well-known game consisting of spinning the cylinder of a revolver loaded with one cartridge, pointing the muzzle at one's own head, and pulling the trigger [140]. Lermontov [124] (Part II, Chapter 3, "The Fatalist") described an experimental study of a primitive version of Russian roulette in 1839. Due to unavailability of actual revolvers (the device was invented around 1835), the number of cylinder chambers n was reduced to one, but the probability $\wp$ that a shot is fired successfully if a cartridge is aligned with the barrel when the trigger is pulled was less than one. In our model, $\wp$ is taken to be one, and the number of loaded cartridges $\tilde{g}$ is allowed to range

between 0 and n. Further generalization is achieved by considering the case of multiple players. We then assign numbers $0, 1, \ldots, n-1$ to the chambers of each revolver cylinder counterclockwise (looking at the muzzle).

We will concentrate on the case of white-blooded players on an $N_1 \times N_2$ square grid. The grid is superimposed over a rectangular part of a geometric plane covered with black snow. Whenever a shot is fired, the corresponding player's blood produces a white pixel. Lines and columns of the grid are enumerated as described in the beginning of Section 2. Let $C_{i,j}$ indicate the revolver cylinder of a player at the position (i, j), and let

$$C_{i,j}[k] = \begin{cases} 1 & \text{if the } k^{\text{th}} \text{ chamber of } C_{i,j} \text{ contains a cartridge,} \\ 0 & \text{otherwise,} \end{cases} \tag{65}$$

for $k = 0, 1, \ldots, n-1$. Let $\text{rand}(n_1..n_2)$ denote a function returning a random integer uniformly distributed on $\{n_1, n_1 + 1, \ldots, n_2\}$, where $n_1 \leq n_2$, and let $\text{int}(x)$ be a function that takes a real number x, and returns an integer obtained by some rounding operation. The line-by-line version of *one-dimensional anti-correlation Russian roulette* can now be described algorithmically as follows.

```
s_{0,0} ← 0; r ← rand(0..n − 1);
for i from 0 to N_1 − 1 do
   for j from 0 to N_2 − 1 do
      {
         for k from 0 to n − 1 do
            C_{i,j}[k] ← 0;
         g̃_{i,j} ← int(g_{i,j}n);
         /* load revolver (i, j): */
         for k from 0 to g̃_{i,j} − 1 do
            {
               k' ← (s_{i,j} + k) mod n;
               C_{i,j}[k'] ← 1;
            }
         /* ensure reduced correlation in 1D: */
         k ← ((k' + 1) mod n);
         if j < N_2 − 1 then s_{i,j+1} ← k;
         else
            if i < N_1 − 1 then s_{i+1,0} ← k;
         /* player (i, j) may now pull the trigger: */
         b_{i,j} ← C_{i,j}[r];
      }
```

The outputs $b_{i,j}$ can be interpreted as values of the corresponding random variables $\xi_{i,j}$ with the expected values

$$E(\xi_{i,j}) = \frac{\tilde{g}_{i,j}}{n} \approx g_{i,j}. \tag{66}$$

Denoting $(i + \delta_{j,N_2-1})$ and $(j+1)(1 - \delta_{j,N_2-1})$ by i' and j' respectively, we can write the covariances

$$\text{cov}(\xi_{i,j}, \xi_{i',j'}) = \frac{1}{n} \sum_{k=0}^{n-1} C_{i,j}[k] C_{i',j'}[k] - \frac{\tilde{g}_{i,j}\tilde{g}_{i',j'}}{n^2} \tag{67}$$

for all integer i, j such that $i \geq 0$, $j \geq 0$, and $ij < (N_1 - 1)(N_2 - 1)$. Our manipulations with k and k' minimize the sums $\sum_{k=0}^{n-1} C_{i,j}[k] C_{i',j'}[k]$.

Delta-sigma (or sigma-delta) modulation [27, 155, 201] is a popular data transformation technique applied in digital signal processing and communication systems. *Single-loop delta-sigma modulation* (more sophisticated configurations are known [33, 84]) over the range [0, 1] (linear transformations cover arbitrary ranges $[\eta_1, \eta_2]$, $\eta_1 < \eta_2$) of the input values $g_i \in [0, 1]$, $i = 1, 2, \ldots, N$, can be described by the formula from [185] that determines the outputs of the procedure,

$$b_i = \begin{cases} 1 & \text{if } g_i + \sum_{k=1}^{i-1}(g_k - b_k) \geq 1/2, \\ 0 & \text{if } g_i + \sum_{k=1}^{i-1}(g_k - b_k) < 1/2, \end{cases} \tag{68}$$

for $i = 1, 2, \ldots, N$.

Anastassiou [6] showed that delta-sigma modulation can be interpreted as one-dimensional error-diffusion, and, conversely, that one-weight error diffusion with

$$W = \begin{pmatrix} 0 & 0 & 0 \\ 1 & \times & \end{pmatrix} \tag{69}$$

can easily be modified to coincide with line-by-line delta-sigma modulation (the error accumulated at the end of one line should be transferred to the beginning of the next line). Figure 14 shows images produced by line-by-line delta-sigma modulation and the magnitude spectra of the corresponding noise images.

Sandler et al. [185] established a relation between delta-sigma modulation and a well-known statistical model, *Poincaré's roulette* [55] (pp. 62–63). This allowed them to prove that the (unbiased) sample mean estimates of averages of consecutive input elements are most efficient in their class (that is, variances of sample means computed from consecutive outputs b_i are minimum among variances of such sample means computed from random binary sequences x_i, $i = 1, 2, \ldots, N$, such that $E(x_i) = g_i$ for all i) for a wide variety of inputs allowing randomization of the encoding procedure. The result followed from the correlation coefficients $\rho(\xi_i, \xi_{i+1})$ being minimum in their class for $i = 1, 2, \ldots, N-1$, where ξ_i is the random variable which b_i is considered to be a value of after randomization.

One-dimensional anti-correlation Russian roulette can simulate single-loop delta-sigma modulation infinitely well if $\lfloor (n-1)/2 \rfloor$ is substituted for r in the algorithmic description above, and the cylinder capacity n goes to infinity. Indeed, the difference between the two algorithms is then due solely to the distortions caused by the function int, and the rounding errors $((\tilde{g}_{i,j}/n) - g_{i,j})$ all go to 0 when $n \to \infty$. If the substitution of $\lfloor (n-1)/2 \rfloor$ for r is not performed, then one-dimensional anti-correlation Russian roulette becomes infinitely close to randomized delta-sigma modulation of Sandler et al. as n approaches infinity. If instead r is computed many times independently, inside the loop over j, just before a trigger is pulled, then we end up performing dithering with white noise.

Randomized discrete error diffusion by generalized Russian roulette is described by

```
r ← rand(0..n − 1);
for i from 0 to N₁ − 1 do
  for j from 0 to N₂ − 1 do
    { /* remember:  ε_{i,j} = 0 if  i < 0,  j < 0, or j ≥ N₂ */
      s_{i,j} ← int (∑_{τ₁=0}^{ℓ−1} ∑_{τ₂=0}^{2(ℓ−1)−ℓδ_{ℓ−1,τ₁}}  w_{τ₁,τ₂} ε_{i−(ℓ−1)+τ₁,j−(ℓ−1)+τ₂}) ;
      for k from 0 to n − 1 do
        C_{i,j}[k] ← 0;
      g̃_{i,j} ← int(g_{i,j}n);
      /* load revolver (i,j) : */
      for k from 0 to g̃_{i,j} − 1 do
        {
```
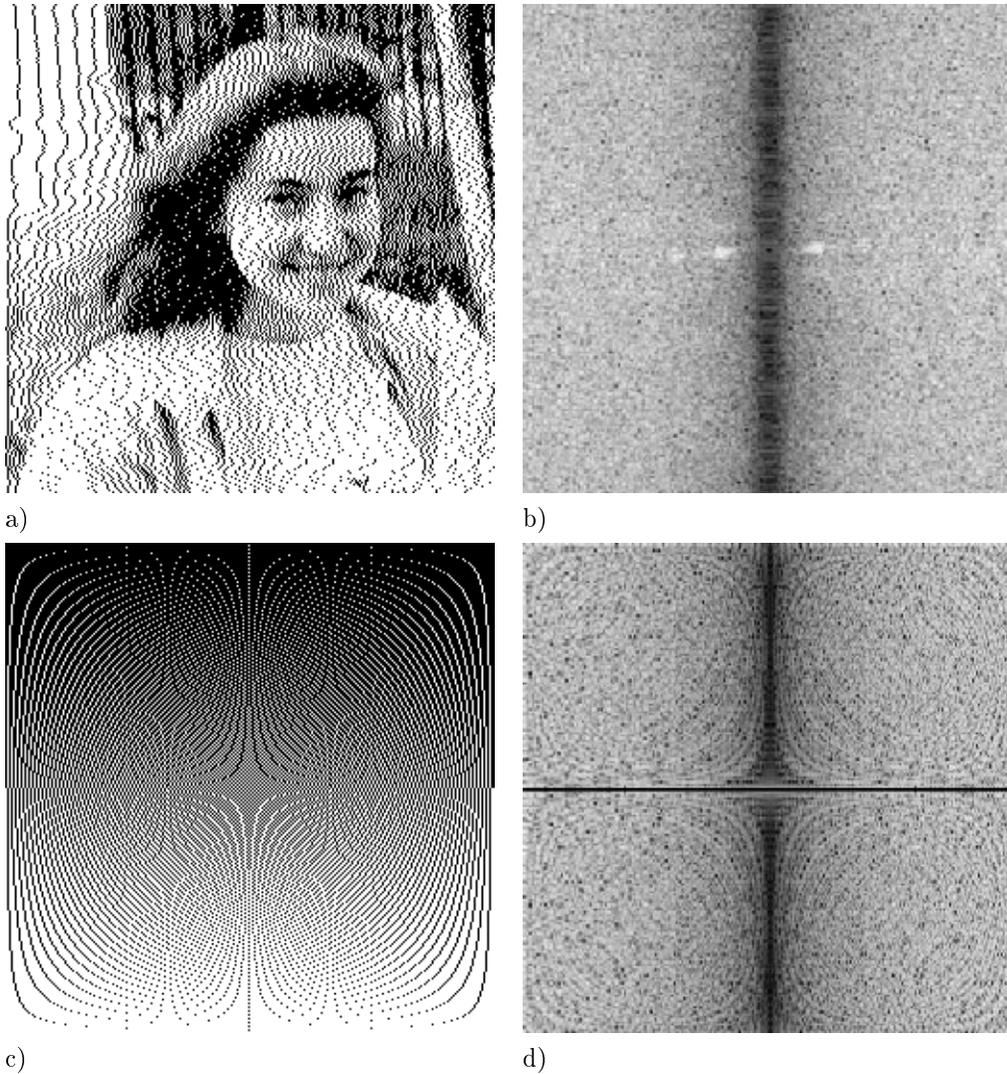
Fig. 14. Line-by-line delta-sigma modulation:
Halftone representations of test images (left);
the magnitude spectra of the corresponding noise images (right).
    a) Portrait of Anya Pogosyants
    b) Magnitude spectrum of the noise image (min = 0.25, max = 5.9)
    c) Gray scale ramp
    d) Magnitude spectrum of the noise image (min = 0.0, max = 6.3)

```
        k' ← s_{i,j} + k;
        if k' < 0 then k' ← k' + n;
        C_{i,j}[k'] ← 1;
      }
  /* compute error: */
  k ← k' + 1;
  if k > r then ε_{i,j} ← k − n; else ε_{i,j} ← k;
  /* player (i,j) may now pull the trigger: */
  b_{i,j} ← C_{i,j}[r];
}
```

When $n \to \infty$, this algorithm reduces to ordinary ED once r is replaced with $\lfloor (n-1)/2 \rfloor$. It can be easily modified to add processing on a serpentine raster. The name of the algorithm does not say "anti-correlation", because the error diffusion coefficients w_{τ_1, τ_2} only approximately tell us how strongly anti-correlated $\xi_{i,j}$ and $\xi_{i-(\ell-1)+\tau_1, j-(\ell-1)+\tau_2}$ should be. Moreover, both generalized Russian roulette algorithms we have considered so far involve loading cartridges so that at most one "gap" consisting of empty chambers is allowed to remain in each loaded revolver cylinder. Results of Sandler et al. [185] suggested that this restriction would not hurt a viewer, whose vision system perceives an image as a single line and averages over consecutive outputs in order to reconstruct averages of consecutive inputs. I am about to show that removal of the restriction facilitates design of better digital halftoning algorithms.

Anti-correlation digital halftoning (ACDH) is a new class of digital halftoning algorithms. It is based on generalized Russian roulette, and multiple gaps are allowed in the revolver cylinders. More control over correlation properties of (unordered) random variable pairs $\{\xi_{i,j}, \xi_{i-(\ell-1)+\tau_1, j-(\ell-1)+\tau_2}\}$ is achieved by using input-dependent *anti-correlation filters* $K = (k_{\tau_1, \tau_2})$. Other techniques incorporated in ACDH are *boundary randomization (BR)* and the *average intensity control (AIC)*. To describe sequential and parallel versions of ACDH in detail, we need more definitions first.

By *average intensity* of an area of a digital image we mean the ratio of the sum of pixel intensities for this area and the overall number of pixels in it. The average intensity control mechanism helps to keep the average intensity of the part of the halftone image already computed closer to the average intensity of the corresponding part of the input image. This is achieved by using the *global histogram of the cartridge distribution* $\mathcal{H}$, an array of

$$\mathcal{H}_k = \sum_{i,j} C_{i,j}[k], \tag{70}$$

$k = 0, 1, \ldots, n-1$.

Local weighted histograms of the cartridge distribution $H(i,j)$ are arrays of

$$H_k(i,j) = \sum_{\substack{\tau_1 \geq 0, \\ \tau_2 \geq 0}} k_{\tau_1, \tau_2} C_{i-(\ell_K-1)+\tau_1, j-(\ell_K-1)+\tau_2}[k], \tag{71}$$

where $\ell_K > 0$ is a constant integer associated with the local anti-correlation filter K.

Let $\mathcal{S}(H(i,j))$ be a permutation of $\{0, 1, \ldots, n-1\}$ such that

$$H_{\mathcal{S}_0(H(i,j))}(i,j) \leq H_{\mathcal{S}_1(H(i,j))}(i,j) \leq \cdots \leq H_{\mathcal{S}_{n-1}(H(i,j))}(i,j), \tag{72}$$

and

$$\mathcal{H}_{\mathcal{S}_x(H(i,j))}(i,j) \leq \mathcal{H}_{\mathcal{S}_y(H(i,j))}(i,j) \tag{73}$$

whenever $x < y$ and $H_{\mathcal{S}_x(H(i,j))} = H_{\mathcal{S}_y(H(i,j))}$. If more than one permutation satifies these conditions, $\mathcal{S}(H(i,j))$ is selected among the eligible permutations at random. Condition (73) is responsible for the AIC.

Let $\tilde{\mathcal{S}}(H(i,j), \tilde{g}_{i,j})$, an *equivalent of $\mathcal{S}(H(i,j))$ with respect to $\tilde{g}_{i,j}$*, be defined as a permutation of $\mathcal{S}(H(i,j))$ such that the elements of subsets $\{\mathcal{S}_0(H(i,j)), \mathcal{S}_1(H(i,j)), \ldots, \mathcal{S}_{\tilde{g}_{i,j}-1}(H(i,j))\}$ and $\{\mathcal{S}_{\tilde{g}_{i,j}}(H(i,j)), \mathcal{S}_{\tilde{g}_{i,j}+1}(H(i,j)), \ldots, \mathcal{S}_{n-1}(H(i,j))\}$ are permuted independently. In other words, all elements that are to the left of $\mathcal{S}_{\tilde{g}_{i,j}}(H(i,j))$ in $\mathcal{S}(H(i,j))$ stay to the left of it in $\tilde{\mathcal{S}}(H(i,j), \tilde{g}_{i,j})$, and all elements to the right of $\mathcal{S}_{\tilde{g}_{i,j}}(H(i,j))$ in $\mathcal{S}(H(i,j))$ stay to the right of it in $\tilde{\mathcal{S}}(H(i,j), \tilde{g}_{i,j})$. $\tilde{\mathcal{S}}(H(i,j), \tilde{g}_{i,j})$ can often be computed faster than $\mathcal{S}(H(i,j))$.

Let $C^{(m)}$ be the *configuration* (state of the revolver cylinders) after the mth iteration, and let $C^{(0)}$ be some starting configuration. Each iteration involves processing of all pixels in some order, which may depend on m and G.

29

Sequential iterative anti-correlation digital halftoning (SIACDH) is a subclass of ACDH defined algorithmically as follows.

$r \leftarrow \mathrm{rand}(0..n-1)$; $m \leftarrow 1$; set $C^{(0)}$; initialize $\mathcal{H}$;

while the last iteration is not over

  { /* remember: all pixels have to be processed */

    for i' **from** 0 **to** $N_1 N_2 - 1$ **do**

      {

        compute pixel coordinates (i,j) depending on i', m and G;

        $\tilde{g}_{i,j} \leftarrow \mathrm{int}(g_{i,j} n)$;

        select K (it may depend on i, j, m, and G);

        compute $H(i,j)$; /* BR: values of $C_{i,j}[k]$ outside the image are random */

        compute $\tilde{\mathcal{S}}(H(i,j), \tilde{g}_{i,j})$;

        /* change the state of cylinder $C_{i,j}$: */

        for k **from** 0 **to** $n-1$ **do**

          {

            $k' \leftarrow \tilde{\mathcal{S}}_k(H(i,j), \tilde{g}_{i,j})$;

            if $k < \tilde{g}_{i,j}$ **then** $C_{i,j}[k'] \leftarrow 1$; **else** $C_{i,j}[k'] \leftarrow 0$;

            update $\mathcal{H}_{k'}$;

          }

      }

    $m \leftarrow m + 1$; /* current $C_{i,j}$ for all (i,j) form configuration $C^{(m)}$ */

  }

/* players may now pull the triggers: */

for i **from** 0 **to** $N_1 - 1$ **do**

  for j **from** 0 **to** $N_2 - 1$ **do**

    $b_{i,j} \leftarrow C_{i,j}[r]$;

The case of one iteration can be reduced to an equivalent of one-dimensional anti-correlation Russian roulette on a space-filling curve by setting $K = (0)$, $\ell_K = 1$ for all pixels. Removal of Condition (73) from the definition of $\mathcal{S}(H(i,j))$ would then disable the AIC, the resulting algorithm getting closer and closer to dithering with white noise as $n \to \infty$.

Parallel iterative anti-correlation digital halftoning (PIACDH) can be explained in terms of each player holding two revolvers, one in each hand (more memory is required). The initial configuration $C^{(0)}$ now describes the original states of revolvers held in the left hands. The first iteration changes the states of revolvers held in the right hands. These states form the next configuration, $C^{(1)}$. Based on $C^{(1)}$, the states of revolvers held in the left hands are modified on the second iteration, and so on. The AIC is off, so Condition (73) is dropped from the definition of $\mathcal{S}(H(i,j))$. If the overall number of iterations is odd, then the players attempt to fire revolvers they are holding in their right hands, otherwise the triggers of revolvers held in their left hands are pulled. Once the cylinders of revolvers currently being loaded are marked $\tilde{C}_{i,j}$, the algorithmic description becomes

  $r \leftarrow \mathrm{rand}(0..n-1)$; $m \leftarrow 1$; set $C^{(0)}$; initialize $\mathcal{H}$;

  while the last iteration is not over

    { /* remember: all pixels have to be processed */

      for i' **from** 0 **to** $N_1 N_2 - 1$ **do**

        {

          compute pixel coordinates (i,j) depending on i', m and G;

          $\tilde{g}_{i,j} \leftarrow \mathrm{int}(g_{i,j} n)$;

          select K (it may depend on i, j, m, and G);

30

```
        compute H(i, j); /* BR: values of C_{i,j}[k] outside the image are random */
        compute 𝒮̃(H(i, j), g̃_{i,j});
        /* change the state of cylinder C̃_{i,j}: */
        for k from 0 to n − 1 do
          {
            k' ← 𝒮̃_k(H(i, j), g̃_{i,j});
            if k < g̃_{i,j} then C̃_{i,j}[k'] ← 1; else C̃_{i,j}[k'] ← 0;
          }
      }
    m ← m + 1;
    swap C_{i,j} and C̃_{i,j} for all (i, j); /* current C_{i,j} for all (i,j) form C^{(m)} */
  }
/* players may now pull the triggers: */
for i from 0 to N_1 − 1 do
  for j from 0 to N_2 − 1 do
    b_{i,j} ← C_{i,j}[r];
```

Efficient implementation of the swaps is straightforward.

Serpentine anti-correlation digital halftoning (SACDH) processes pixels on a serpentine raster, using wedge-shaped input-dependent anti-correlation filters. The starting configuration $C^{(0)}$ corresponds to all revolver cylinders being empty. SACDH is a representative of SIACDH, but only one iteration is performed. In the versions of SACDH I implemented ($n = 255$ and $n = 192$ were tried), BR is performed by taking the values $C_{i,j}[k]$ for (i, j) outside the image to be

$$C_{i,j}[k] = \begin{cases} 1 & \text{if } \mathbf{r}_{BR} < n\Delta, \\ 0 & \text{otherwise,} \end{cases} \tag{74}$$

where

$$\Delta = |\tilde{g}_{i,j} - n/2|/n, \tag{75}$$

and $\mathbf{r}_{BR}$ is a value of a random variable uniformly distributed on $\{0, 1, \ldots, \lceil n/2 \rceil\}$ and computed independently whenever an attempt is made to look up the value of $C_{i,j}[k]$ for (i, j) outside the image. The process of filter selection for my versions of SACDH is described in Appendix A. The asymmetry of the chosen filters is seemingly needed to compensate for the asymmetry of sequential processing. Figure 15 shows halftone images produced by SACDH ($n = 255$) and the magnitude spectra of the corresponding noise images.

When examined visually, the gray scale ramps for the case $n = 192$ did not differ significantly from those for $n = 255$. Section 7 will explain why the version with $n = 192$ was used to test SACDH for presence of transient boundary effects and inherent edge enhancement.

No tone scale adjustment was performed in order to produce 100 dpi halfone representations of the gray scale ramp. Appendix B describes photometric measurements and other research conducted by the author to determine how much tone scale adjustment was needed for printing of the halftone images at different resolutions on HP LaserJet IVsi printers. Figure 16 shows representations of the portrait of Anya Pogosyants created using different digital halftoning algorithms and printed at 300 dpi. Tone scale adjustment function "c1" from Appendix B was applied. Yet another tone scale adjustment function had been applied to the 256×256 version of the portrait of Anya Pogosyants before its 100 dpi halftone representations were generated.

Figure 17 contains halftone representations of the gray scale ramp printed at 300 dpi. Again, TSA function "c1" was applied.

When the pixel at the position (i, j) is being processed by SACDH, the values of the coefficients k_{τ_1, τ_2} of the local anti-correlation filter K signify how strongly we want $\xi_{i,j}$ and
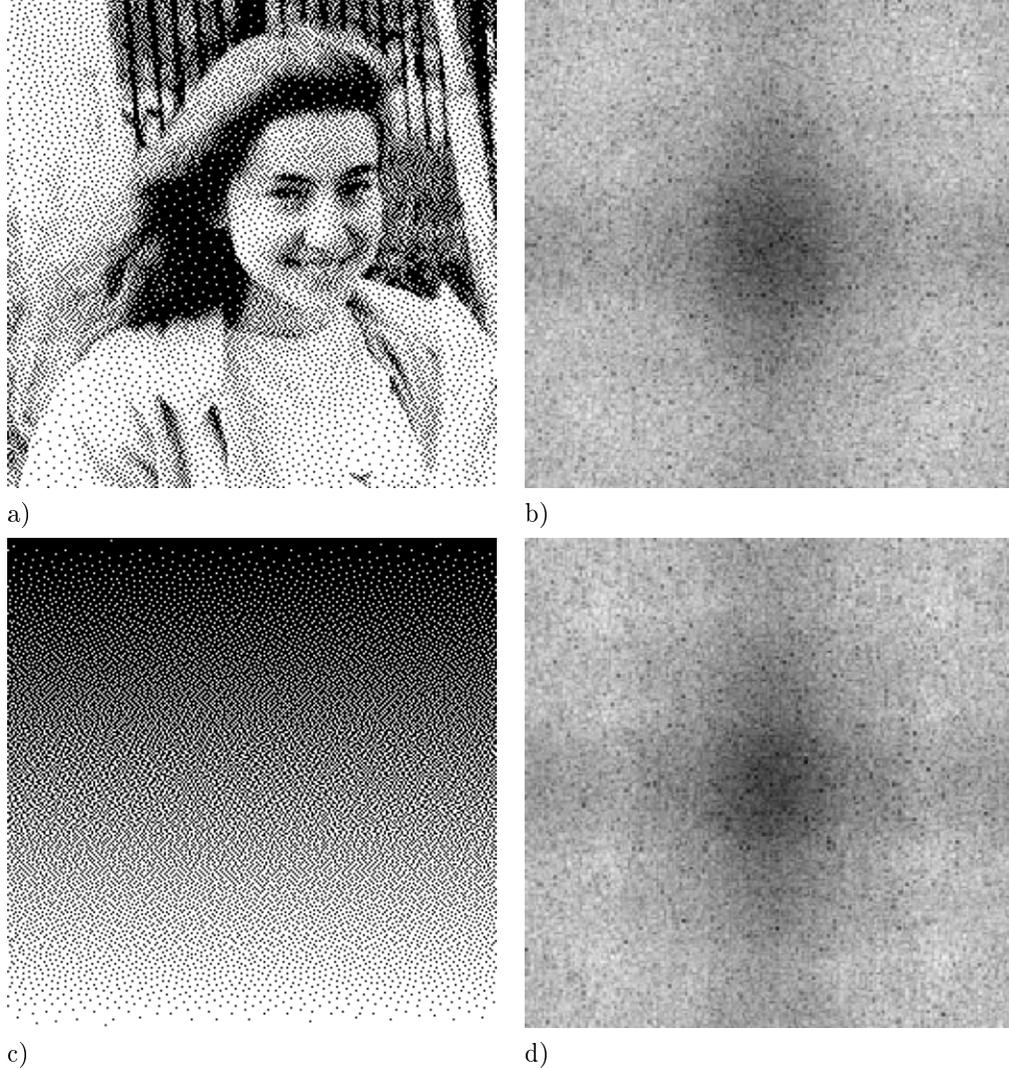
Fig. 15. Serpentine anti-correlation digital halftoning:
Halftone representations of test images (left);
the magnitude spectra of the corresponding noise images (right).
    a) Portrait of Anya Pogosyants
    b) Magnitude spectrum of the noise image (min = 0.15, max = 6.1)
    c) Gray scale ramp
    d) Magnitude spectrum of the noise image (min = 0.16, max = 6.3)

$\xi_{i-(\ell_K-1)+\tau_1, j-(1-2(i \bmod 2))((\ell_K-1)-\tau_2)}$ to be anti-correlated. Note that, while rather strict conditions have to be imposed on error diffusion coefficients w_{τ_1, τ_2} to ensure numerical stability [6, 54, 230], making sure that the computation of sums from Eq. (71) never causes an overflow is enough to achieve stability when designing anti-correlation filters. As a result, it is relatively simple to break up any unwanted regular binary pattern or correlated artifact by adjusting K. But which periodic patterns are "bad"? This is not an easy question to answer, and more definitions are needed before we can tackle the problem.

In halftone images, artificial contours may sometimes appear in the areas with slowly varying [218] or constant [188] input intensity. This effect is called *contouring* [218].

Presence of *correlated artifacts* [218], which are sometimes called "worms" or "zebra stripes" is

a)   b)   c)

d)   e)   f)
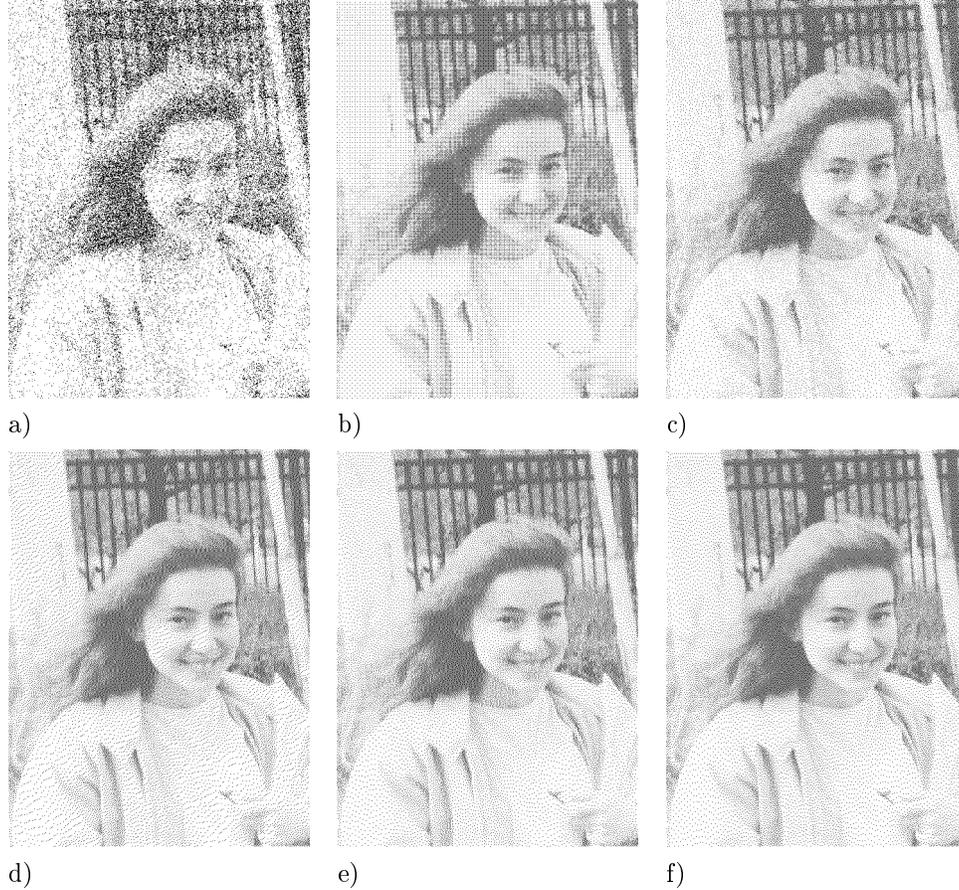
Fig. 16 (Part I). Portrait of Anya Pogosyants, 300 dpi
    a) Dithering with white noise
    b) Ordered dither with a recursive tesselation matrix (Eq. (4))
    c) Ordered dither with a blue noise mask (void-and-cluster)
    d) Classical Floyd–Steinberg error diffusion (Eq. (9))
    e) Four-weight serpentine error diffusion, deterministic weights (Eq. (11))
    f) Three-weight serpentine error diffusion, deterministic weights (Eq. (12))

another problem. It is common for the algorithms that do not generate regular periodic patterns.

In Section 2, we have already mentioned studies on binary textures. Regular periodic patterns generated by halftoning algorithms are called *halftone dot textures* [153]. Texture visibility and texture segregation are extensively studied [102, 153, 156, 188, 189, 244]. Presence of highly visible textures usually means poor rendition of small details of the image.

Figure 18 illustrates a "texture paradox" that affected the design of the SACDH algorithm. While simple periodic patterns often provide visually pleasing representations of constant intensity levels, many of them tend to have very visible borders. This leads to contouring. Figures 3 (a) and (c), 16 (b), and 17 (b) provide numerous examples of that. Not surprisingly, visibility of the texture borders depends on the image resolution and the viewing distance. This is easy to notice, say, by looking at the center of Fig. 18 from different distances and by comparing Fig. 3 (a) and (c) to Fig. 16 (b) and Fig. 17 (b), respectively.

Zeggel and Bryngdahl [248] opined that "the allowed texture for grayvalues of 0.5 is a checker-board pattern". Ulichney used to share this opinion [218], but changed his mind [221], and a comparison of the midsections of Fig. 8 (c) and Fig. 4 (c) clearly shows that. (The halftone images

Fig. 16 (Part II). Portrait of Anya Pogosyants, 300 dpi

g) Four-weight serpentine error diffusion, 50% random weights (Eq. (13))

h) Error diffusion combined with pulse-density modulation

i) Error diffusion with intensity-dependent weights (Eq. (14))

j) Error diffusion with threshold modulation using threshold imprints

k) The iterative convolution algorithm

l) Serpentine anti-correlation digital halftoning

in these pictures were produced using the algorithms designed and liked the most by Ulichney in 1987 and 1993, respectively.)

Let's denote constant grayscale intensity levels by g. I tried to eliminate all periodic patterns that either seemed obnoxious by themselves, or caused contouring at 72 dpi, 100 dpi, or 300 dpi. The checkerboard pattern, the pattern for $g = 3/4$ that can be seen next to the left bottom corner of Fig. 18, and its counterpart for $g = 1/4$ were among such patterns. Note that the problem with the checkerboard pattern at 300 dpi is largely due to the printer distortions [110], and not the "texture paradox" itself. While it proved straightforward to eliminate any given periodic pattern by changing the coefficients of anti-correlation filters, other unwanted textures would often emerge instead, so I had to perform multiple "trial-and-error" cycles similar to those described in [2]. In addition to that, it turned out that some patterns suppressed in the halftone ramp may occasionally surface in test images with more gradient. For the diehard fans of the checkerboard pattern, I recommend using

34
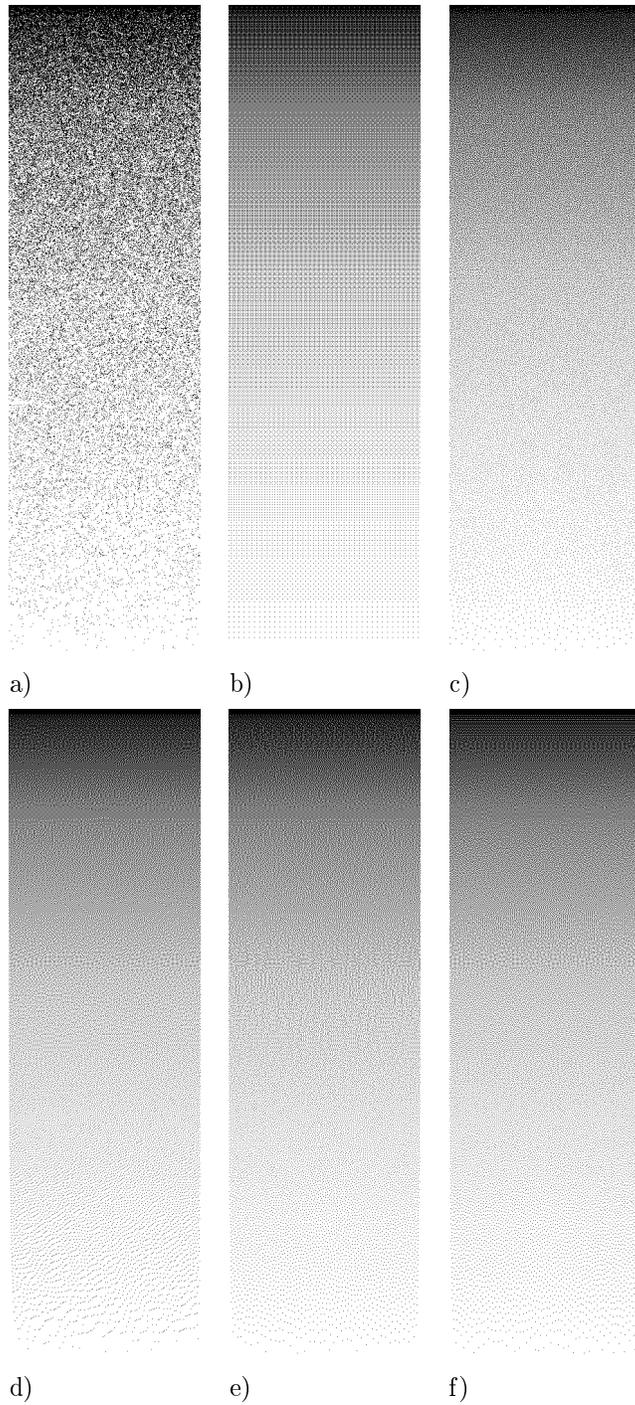
Fig. 17 (Part I). Gray scale ramp, 300 dpi
    a) Dithering with white noise
    b) Ordered dither with a recursive tesselation matrix (Eq. (4))
    c) Ordered dither with a blue noise mask (void-and-cluster)
    d) Classical Floyd–Steinberg error diffusion (Eq. (9))
    e) Four-weight serpentine error diffusion, deterministic weights (Eq. (11))
    f) Three-weight serpentine error diffusion, deterministic weights (Eq. (12))
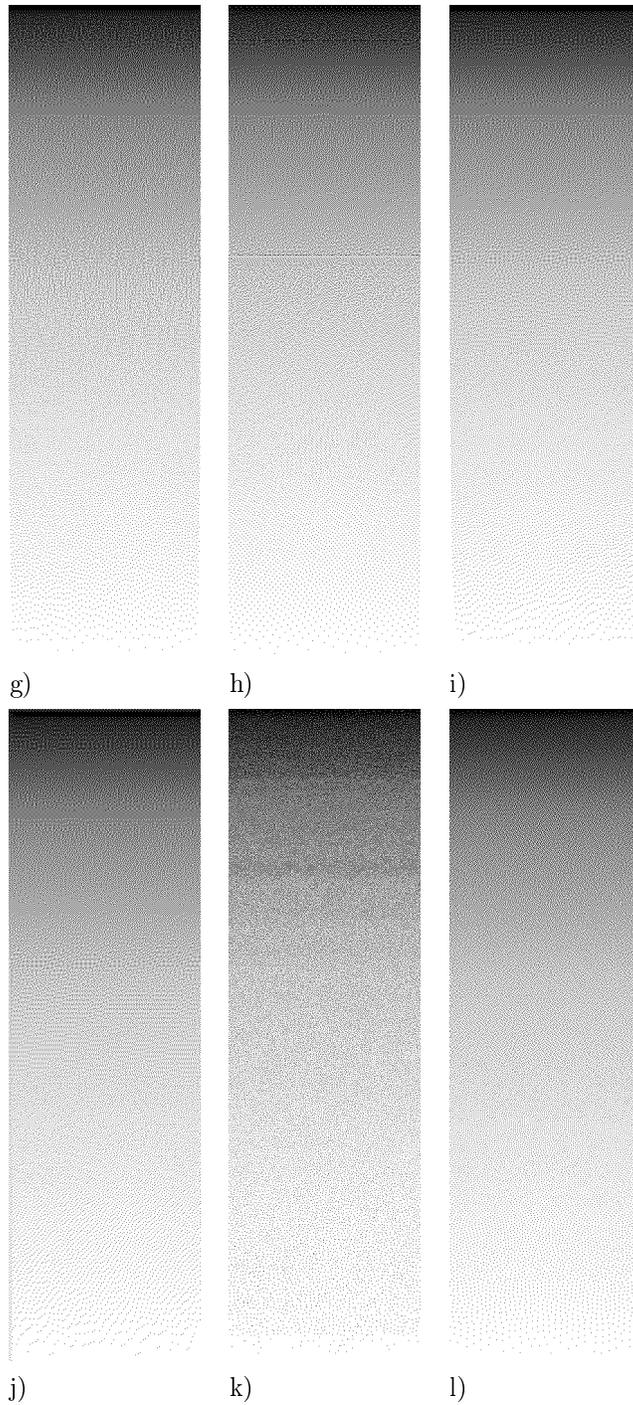
Fig. 17 (Part II). Gray scale ramp, 300 dpi

    g) Four-weight serpentine error diffusion, 50% random weights (Eq. (13))

    h) Error diffusion combined with pulse-density modulation

    i) Error diffusion with intensity-dependent weights (Eq. (14))

    j) Error diffusion with threshold modulation using threshold imprints

    k) The iterative convolution algorithm

    l) Serpentine anti-correlation digital halftoning
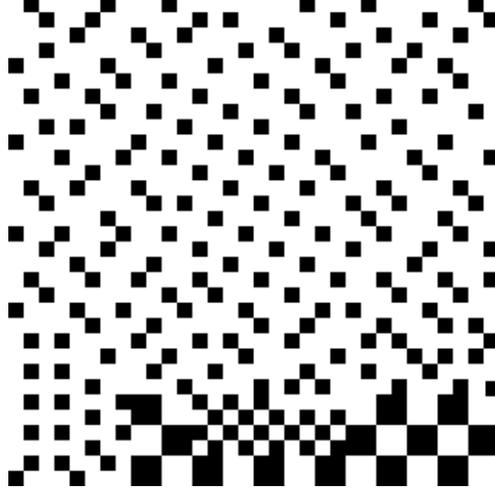
Fig. 18. The "texture paradox": Periodic and aperiodic patterns

$$K = \begin{array}{|c|c|c|c|c|} \hline 14 & 16 & 23 & 7 & 3 \\ \hline 15 & 46 & 65 & 23 & 4 \\ \hline 15 & 62 & \times & & \\ \hline \end{array} \tag{76}$$

when $\Delta < 13/255$, in place of the corresponding filter from Appendix A. My versions of SACDH suppress contouring, worm-like artifacts like those in Figures 8 (c) and 12 (c), and similar fishbone-like artifacts (Fig. 8 (c)) near $g = 1/2$ at the cost of increased granularity in that area.

In the next section, we will discuss what else visual examination of the halftone images can tell us about SACDH and other digital halftoning techniques in connection with the properties of the corresponding noise spectra.

5. The Noise Spectra, the Corresponding Phase Spectra, and Halftone Image Quality

We visualize the phase spectra of the noise images in the HSV color model [66]. Saturation S and value V are both set to 1, and hue is

$$H_{u,v} = 360\phi'_{B-G}(u,v)/2\pi \tag{77}$$

for $u = 0, 1, \ldots, N_1 - 1$, $v = 0, 1, \ldots, N_2 - 1$. Let $\langle x \rangle$ denote the *fractional part* of x. Then the coordinates in the RGB color space (each of them in $[0, 1]$) can be computed as follows.

$$R_{u,v} = \delta_{0,\lfloor H_{u,v}/60\rfloor} + \delta_{5,\lfloor H_{u,v}/60\rfloor} + \langle H_{u,v}/60\rangle\delta_{4,\lfloor H_{u,v}/60\rfloor} + (1 - \langle H_{u,v}/60\rangle)\delta_{1,\lfloor H_{u,v}/60\rfloor}, \tag{78}$$

$$G_{u,v} = \delta_{1,\lfloor H_{u,v}/60\rfloor} + \delta_{2,\lfloor H_{u,v}/60\rfloor} + \langle H_{u,v}/60\rangle\delta_{0,\lfloor H_{u,v}/60\rfloor} + (1 - \langle H_{u,v}/60\rangle)\delta_{3,\lfloor H_{u,v}/60\rfloor}, \tag{79}$$

$$B_{u,v} = \delta_{3,\lfloor H_{u,v}/60\rfloor} + \delta_{4,\lfloor H_{u,v}/60\rfloor} + \langle H_{u,v}/60\rangle\delta_{2,\lfloor H_{u,v}/60\rfloor} + (1 - \langle H_{u,v}/60\rangle)\delta_{5,\lfloor H_{u,v}/60\rfloor}. \tag{80}$$

Note that the luminance of $(R_{u,v}, G_{u,v}, B_{u,v})$ may differ for different $\phi'_{B-G}(u,v)$. This allows it to play a supplementary role in visualization, because the human vision system is more sensitive to changes in luminance than to those in chromaticities [172].

Our approach to color visualization of the discrete Fourier spectra of the noise images is as follows. Let

$$l'_{u,v} = \ln(1 + |\mathbf{f}'_{B-G}(u,v)|) \tag{81}$$

37

for $u = 0, 1, \ldots, N_1 - 1$, $v = 0, 1, \ldots, N_2 - 1$.

$$Y_{u,v} = 0.3 + \frac{0.6 l'_{u,v}}{9.7} \tag{82}$$

will be interpreted as values of luminance in the YIQ color coordinate system [172]. In this system,

$$Y_{u,v} = 0.299 R_{u,v} + 0.587 G_{u,v} + 0.114 B_{u,v}. \tag{83}$$

In Eq. (82), 0.3 and 0.6 are constants empirically selected so that $0 < Y_{u,v} < 1$. (9.7 happens to be the largest value of $l'_{u,v}$ I have encountered so far in the course of my study of the noise spectra.) Let $\tilde{S}_k(u, v)$, $k = 0, 1, \ldots, 5$, be the Euclidean distances (in the RGB color space) from $(Y_{u,v}, Y_{u,v}, Y_{u,v})$ to the lines of intersection of the faces of the RGB cube and the plane $\Pi_{u,v}$ perpendicular to the vector $[0.299, 0.587, 0.144]^\top$ and containing $(Y_{u,v}, Y_{u,v}, Y_{u,v})$. (The symbol $\top$ denotes the *matrix transpose*; we preserve a slight notational distinction between the vectors and the triples describing coordinates of points.)

$$\tilde{S}_{u,v} = \min_k \tilde{S}_k(u, v) \tag{84}$$

play the role of saturation. $\tilde{S}_{u,v}$ depend on $Y_{u,v}$. My experiments showed that if some constant saturation, say, $\min_{0.3 \leq Y_{u,v} \leq 0.9} (\tilde{S}_{u,v})$, is maintained, then the chromaticity changes are too difficult to notice, while, as the next section will demonstrate, the importance of the phase information is high. We compute coordinates $(R_{u,v}, G_{u,v}, B_{u,v})$ of a point in $\Pi_{u,v}$ such that

$$\sqrt{[R_{u,v} - Y_{u,v}]^2 + [G_{u,v} - Y_{u,v}]^2 + [B_{u,v} - Y_{u,v}]^2} = \tilde{S}_{u,v}, \tag{85}$$

and the angle between vectors $[(Y_{u,v}/0.299) - Y_{u,v}, -Y_{u,v}, -Y_{u,v}]^\top$ and $[R_{u,v} - Y_{u,v}, G_{u,v} - Y_{u,v}, B_{u,v} - Y_{u,v}]^\top$ is equal to $\phi'_{B-G}(u, v)$. This is achieved by using the formula

$$\begin{bmatrix} R_{u,v} \\ G_{u,v} \\ B_{u,v} \end{bmatrix} = \mathbf{R}(u, v) \begin{bmatrix} \dfrac{((Y_{u,v}/0.299) - Y_{u,v})\tilde{S}_{u,v}}{\sqrt{((Y_{u,v}/0.299) - Y_{u,v})^2 + 2Y_{u,v}^2}} \\ \dfrac{-Y_{u,v}\tilde{S}_{u,v}}{\sqrt{((Y_{u,v}/0.299) - Y_{u,v})^2 + 2Y_{u,v}^2}} \\ \dfrac{-Y_{u,v}\tilde{S}_{u,v}}{\sqrt{((Y_{u,v}/0.299) - Y_{u,v})^2 + 2Y_{u,v}^2}} \end{bmatrix} + \begin{bmatrix} Y_{u,v} \\ Y_{u,v} \\ Y_{u,v} \end{bmatrix}, \tag{86}$$

where

$$\mathbf{R}(u, v) = \begin{bmatrix} \cos\phi + n_r^2(1 - \cos\phi) & n_r n_g(1 - \cos\phi) - n_b \sin\phi & n_r n_b(1 - \cos\phi) + n_g \sin\phi \\ n_g n_r(1 - \cos\phi) + n_b \sin\phi & \cos\phi + n_g^2(1 - \cos\phi) & n_g n_b(1 - \cos\phi) - n_r \sin\phi \\ n_b n_r(1 - \cos\phi) - n_g \sin\phi & n_b n_g(1 - \cos\phi) + n_r \sin\phi & \cos\phi + n_b^2(1 - \cos\phi) \end{bmatrix} \tag{87}$$

is a matrix representing three-dimensional rotation about the axis $[0.299, 0.587, 0.144]^\top$. In Eq. (87),

$$n_r = \frac{0.299}{\sqrt{0.299^2 + 0.587^2 + 0.144^2}}, \tag{88}$$

$$n_g = \frac{0.587}{\sqrt{0.299^2 + 0.587^2 + 0.144^2}}, \tag{89}$$

$$n_b = \frac{0.144}{\sqrt{0.299^2 + 0.587^2 + 0.144^2}}, \tag{90}$$

and

$$\phi = \phi'_{B-G}(u, v). \tag{91}$$

A test 256×256 two-dimensional discrete phase spectrum with $\phi = \phi'(u, v)$ computed from $\text{Re}(f'_{u,v}) = (v - 128)$ and $\text{Im}(f'_{u,v}) = (128 - u)$ using the appropriate modifications of Eqs. (18) and

38

a)   b)
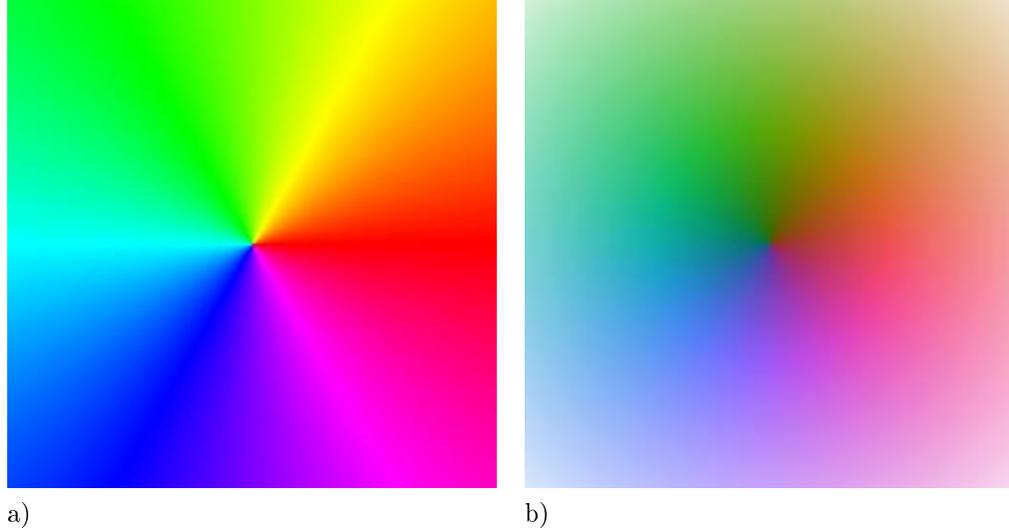
Fig. 19. Visualizations of the test spectra:
a) Phase spectrum
b) Discrete Fourier spectrum

(20) is shown in Figure 19 (a). A test 256×256 discrete Fourier spectrum with the same $\phi'(u, v)$ and

$$l'_{u,v} = \frac{9.7\sqrt{(u - 128)^2 + (v - 128)^2}}{128\sqrt{2}} \tag{92}$$

is visualized in Figure 19 (b).

Figures 20–33 visualize the phase spectra and the discrete Fourier spectra of the noise images corresponding to the image-algorithm pairs studied in Sections 2 and 4.

Quantization with a fixed threshold can be interpreted as ordered dither with a 1×1 dither matrix. Interestingly enough, considering Figures 1 (d), 3 (d), and 4 (d), we observe that dithering of a 256×256 gray scale ramp with a 1×1 dither matrix causes the noise spectrum to have 1 strip of nonzero values, application of an 8×8 matrix forces 8 strips of nonzero values to appear, and dithering with a 128×128 matrix produces 128 parallel strips of nonzero DFT coefficients. Figures 1 (a) and (c) are the extreme cases of contouring, less contouring is seen in Fig. 3 (a) and (c), and virtually no contouring can be seen in Fig. 4 (a) and (c). This improvement is due both to the increase in size of the dither matrix and advances in the matrix design. Figures 1 (b), 3 (b) and 4 (b) illustrate how peaks in the magnitude spectrum of the quanization noise image are first shifted to the higher frequencies and then reduced in size and scattered over the high-frequency region, as the dither technique improves. Figures 20 (a), 22 (a), and 23 (a) form a sequence showing reduction of wavy correlated phase patterns, which are, perhaps, "relatives" of the strips from Figures 20 (c), 22 (c), and 23 (c).

Figures 2 and 21 show that dithering with white noise results in poor rendition of images while leading to almost flat magnitude spectra and clustery phase spectra of the noise images. The noise spectra for the portrait and the ramp show more apparent similarity than those for the same pair of grayscale images subjected to ordered dither. It even seems that a little bit more effort is needed to distinguish between the two halftone images from Fig. 2 than is required for the other portrait-ramp pairs of halftone images in this paper. Note that the quantization noise characteristic for dithering with white noise is not exactly white. This is due to presence of the binary quantizer.

39
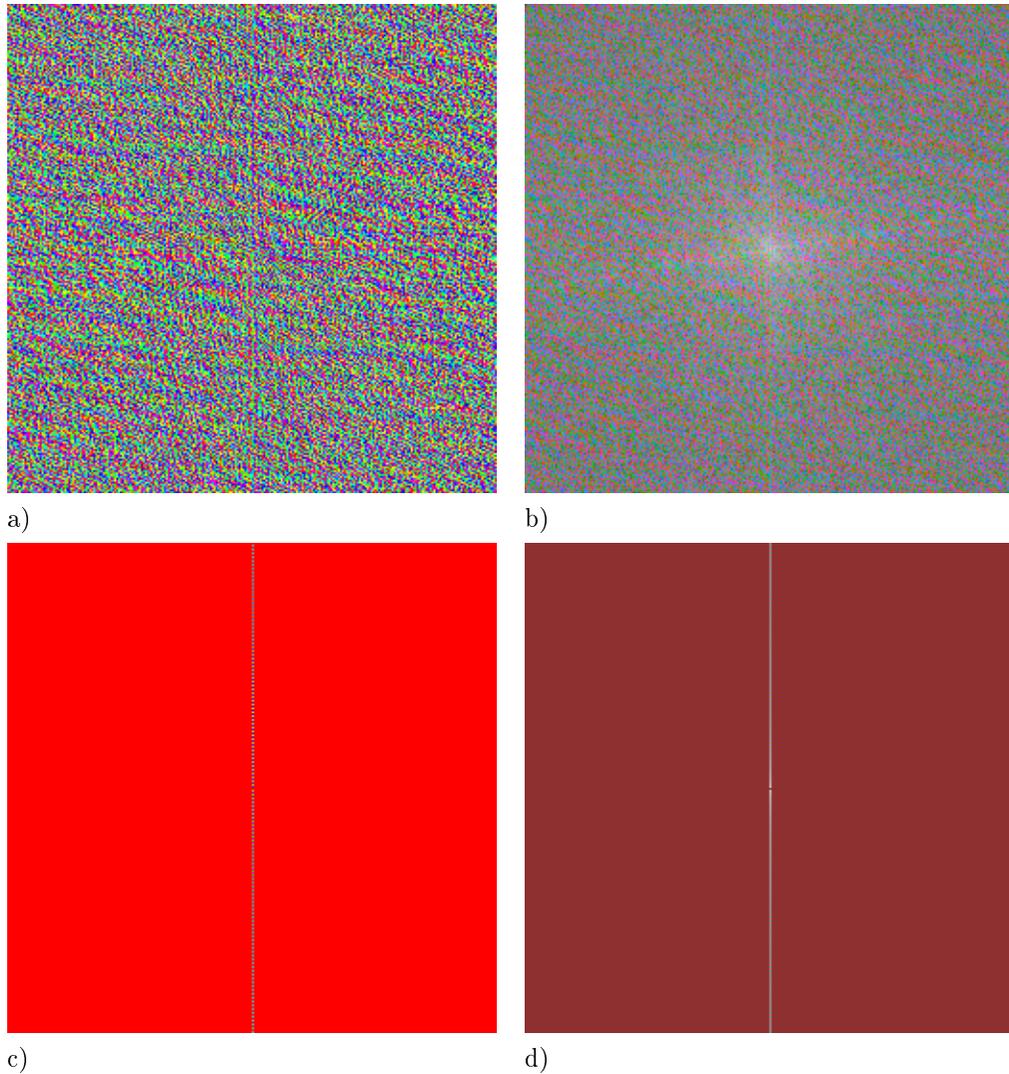
Fig. 20. Quantization with a fixed threshold ($s = 0$):
The phase spectra of the noise images (left);
the discrete Fourier spectra of the noise images (right).
a), b) For the portrait of Anya Pogosyants
c), d) For the gray scale ramp

The versions of the void-and-cluster dither and the iterative convolution algorithm used to make Fig. 4 (a) and (c), Fig. 12 (a) and (c), and Fig. 16 (c) and (k) were designed so that the magnitude spectra are close to being radially symmetric. (These spectra are shown in Fig. 4 (b) and (d), Fig. 12 (b) and (d).) Vertical and horizontal harmonics not being suppressed better than diagonal ones, characteristic worm-like artifacts emerge in both cases. Problems with representation of very dark and very light tones are due to a phenomenon known as the *low-frequency leakage* [147].

Radial asymmetry of the kind seen in the spectra associated with the algorithms based on error diffusion on an ordinary raster (Figures 5, 10, 11, 24, 29, 30) can be linked to presence of diagonal correlated artifacts similar to zebra stripes in the regions of very high and very low average intensity. The problem can be alleviated somewhat by using serpentine raster (Figures 6–8, 25–27) or larger filters (Figures 10 and 29). Sometimes, other problems emerge, the vertical "worms" near $g = 3/4$ (the middle of Fig. 17 (e)) being a good example.
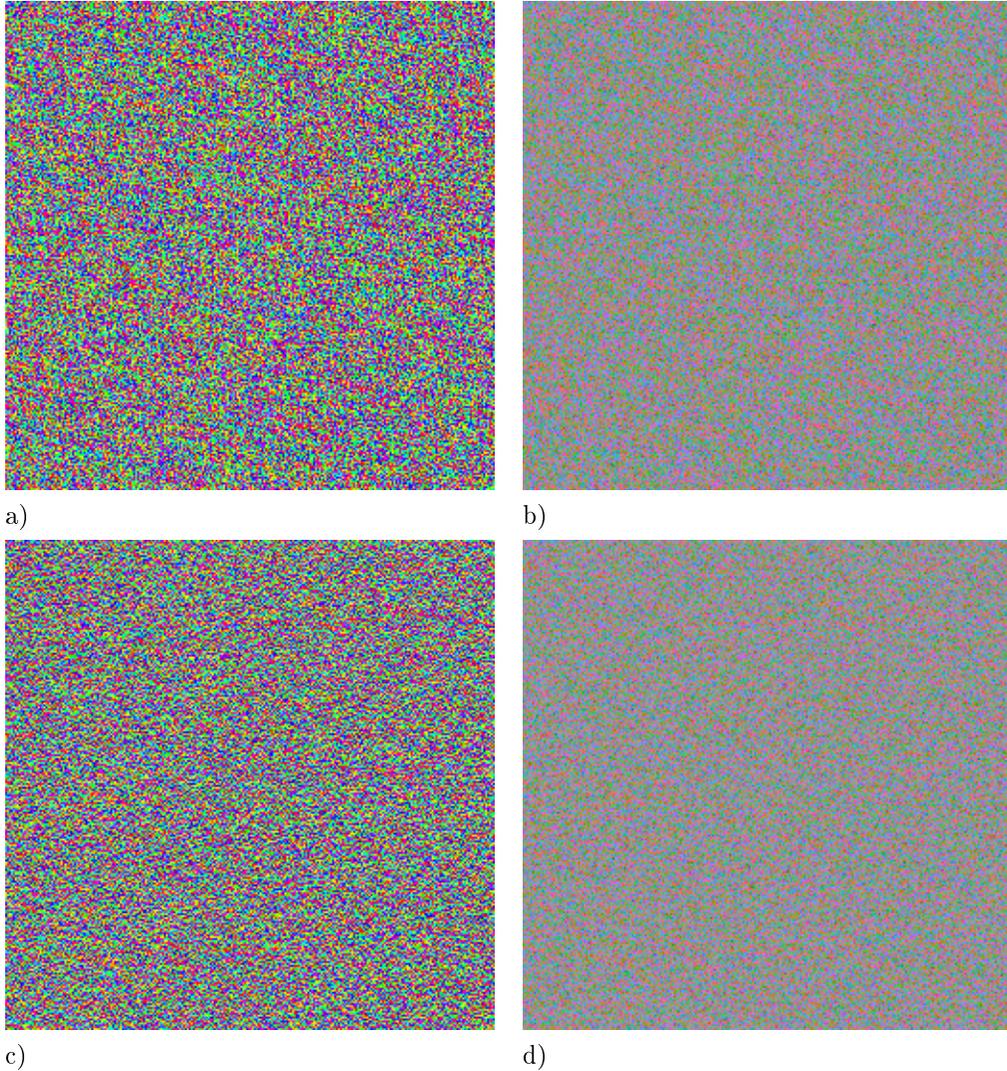
Fig. 21. Dithering with white noise:
The phase spectra of the noise images (left);
the discrete Fourier spectra of the noise images (right).
a), b) For the portrait of Anya Pogosyants
c), d) For the gray scale ramp

Strips of high-amplitude low-frequency components with the same phases visible in Figures 24–27, 29, and 30, appear to mark presence of upleasant *transient boundary effects*. We will talk more about them in Section 7. The light strip in Fig. 9 (d) is related to the texture seams in Fig. 9 (c).

As you can see in Fig. 15, my version of SACDH ($n = 255$) supresses vertical and horizontal harmonics of the magnitude spectra of noise images, so the less visible diagonal correlated artifacts are favored over those oriented vertically or horizontally, and the magnitude spectra are close to being cross-shaped. The noise generated is pretty close to being violet. The images in Figures 15 (a) and (c), 16 (l), and 17 (l) show very little or no contouring. Very dark and very light areas look nice.
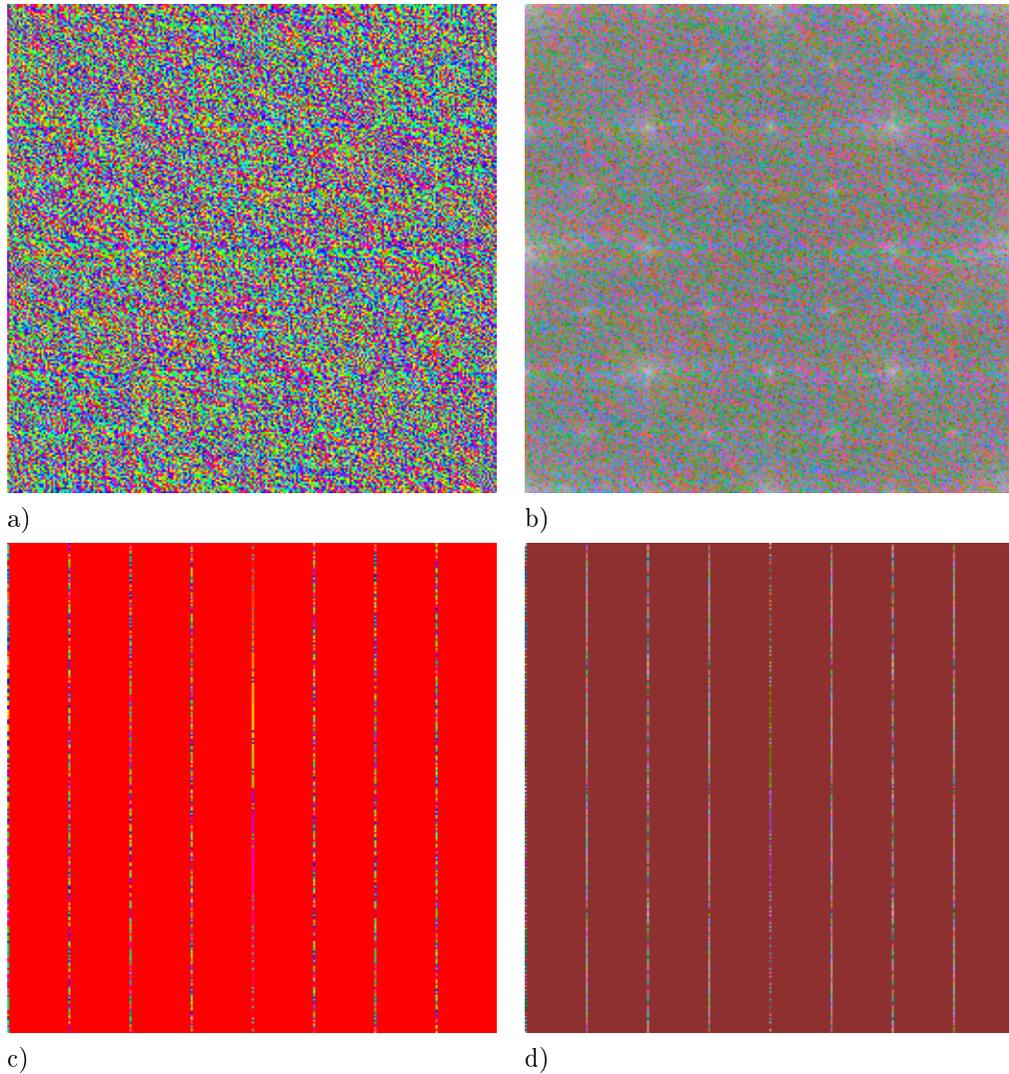
Fig. 22. Ordered dither with a recursive tesselation matrix (Eq. (4)):
    The phase spectra of the noise images (left);
    the discrete Fourier spectra of the noise images (right).
        a), b) For the portrait of Anya Pogosyants
        c), d) For the gray scale ramp

6. Relative Importance of the Magnitudes and the Phases

Figure 34 features hybrid images obtained by replacing magnitudes (phases) of the DFT of one noise image by magnitudes (phases) of another noise image, performing the two-dimensional inverse discrete Fourier transform, adding the result to the original grayscale image, and clipping the output values so that none of them stays below that assigned to "black" or above that assigned to "white".

It appears that the algorithms that produce "good" halftone representations generate quantization noise with "good" magnitudes and "good" phases, while the noise of quantization with a fixed threshold has a discrete Fourier spectrum with "bad" magnitudes and "bad" phases.

Now, suppose that we start with two distinct grayscale digital images and compute the quantization noise matrix as the difference between the binary output produced by a high-quality halftoning algorithm when given one of them as input, and the grayscale data for the other image.
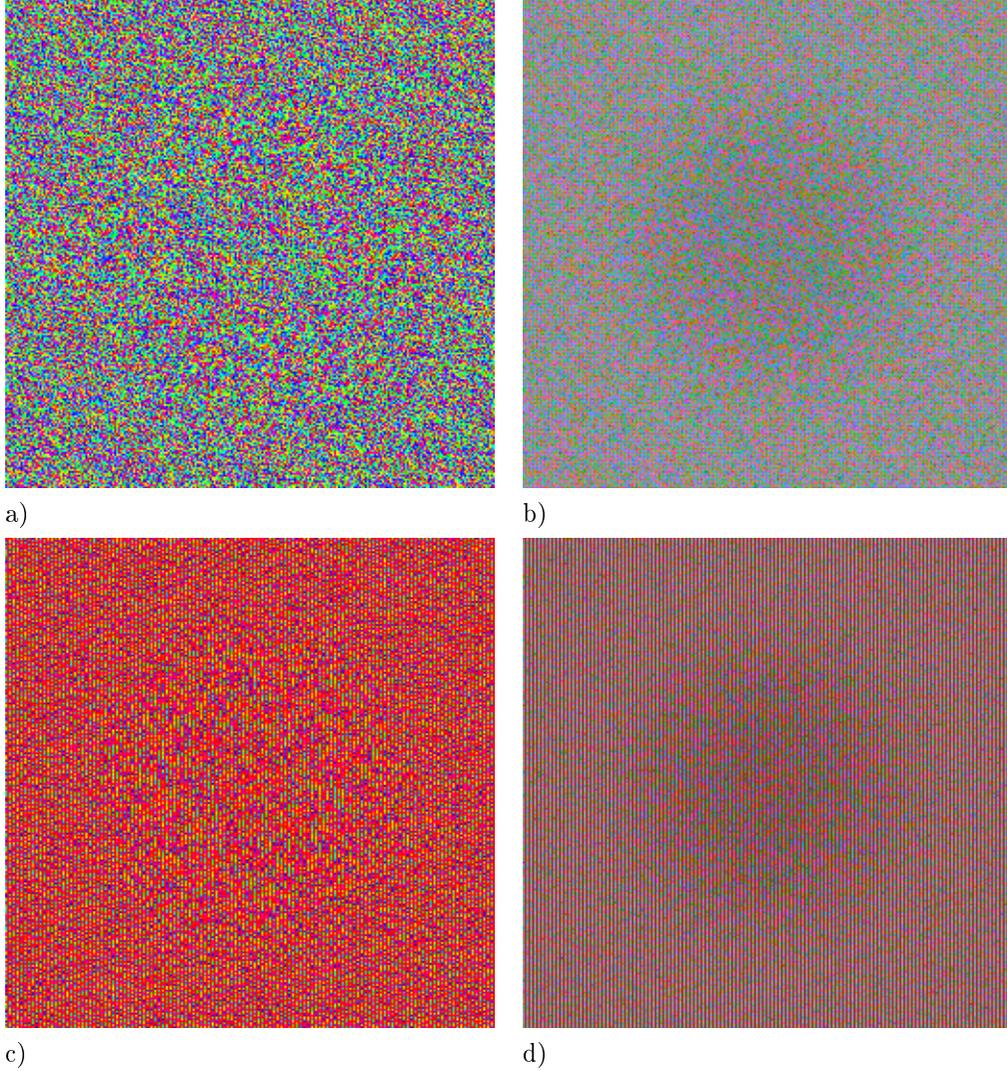
Fig. 23. Ordered dither with a blue noise mask (void-and-cluster):
The phase spectra of the noise images (left);
the discrete Fourier spectra of the noise images (right).
a), b) For the portrait of Anya Pogosyants
c), d) For the gray scale ramp

Fig. 35 shows the noise spectrum that emerges when one pretends that the halftone ramp produced by SACDH ($n = 255$) and shown in Fig. 15 (c) is representing the portrait of Anya Pogosyants. Notice the similarity between Fig. 35 and Fig. 20 (b).

7. Average Intensity Representation, Boundary Effects, and Edge Enhancement

To get an idea of how well average intensities are preserved by different digital halftoning algorithms, I decided to compute global *intensity distortion*

$$M = \sum_{i=0}^{N-1} \sum_{j=0}^{N-1} e_{i,j} \tag{93}$$

for $N \times N$ halftone images representing the input images such that $g_{i,j} = g$ for all $i = 0, 1, \ldots, N-1$, $j = 0, 1, \ldots, N-1$. Computations were performed for $N = 16, 32, 48, \ldots, 464$, $g = 1/64$,

43
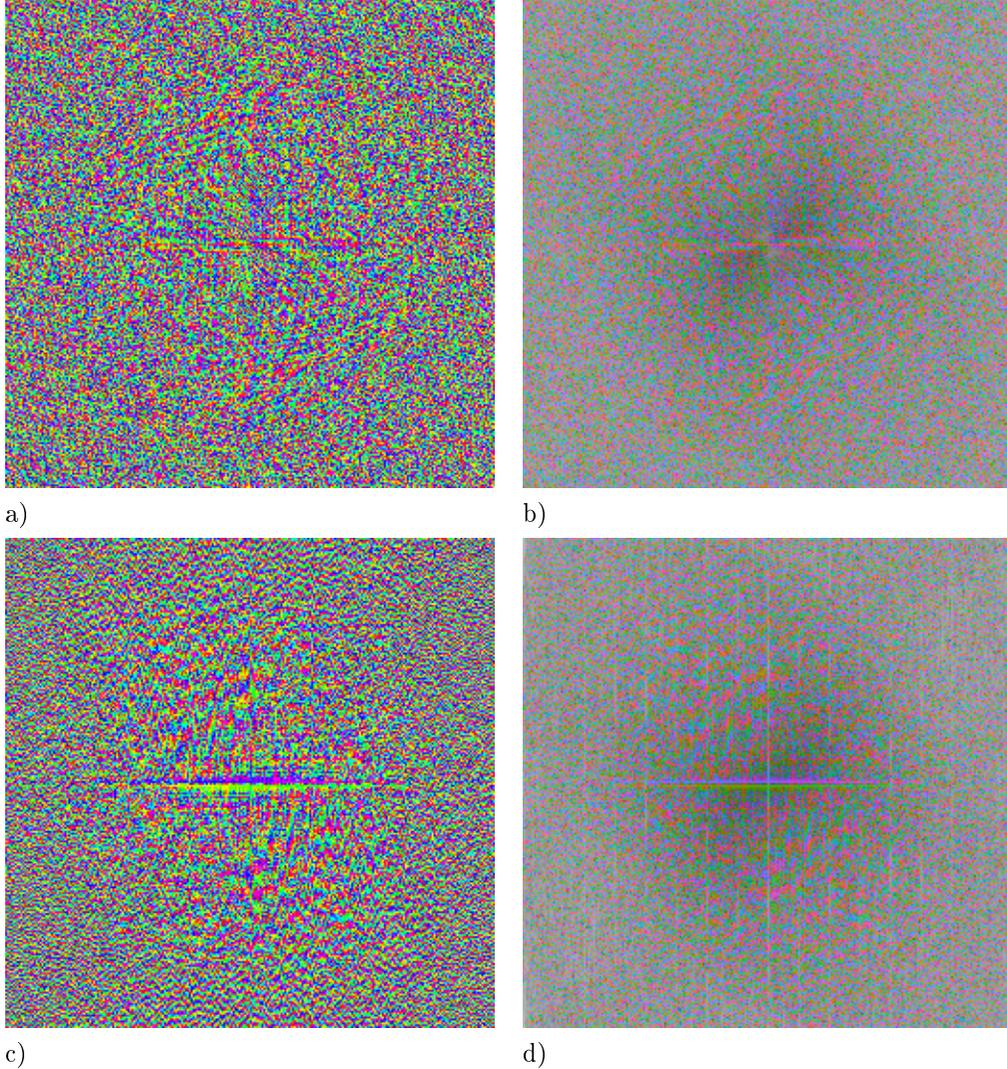
Fig. 24. Classical Floyd–Steinberg error diffusion (Eq. (9)):
The phase spectra of the noise images (left);
the discrete Fourier spectra of the noise images (right).
a), b) For the portrait of Anya Pogosyants
c), d) For the gray scale ramp

$2/64, \ldots, 63/64$. (Zeremba [251] and Shirley [195] developed similar criteria in order to evaluate how well the sampling points are distributed on the image plane.) The results are plotted in Figure 36. The special boundary randomization technique applied to obtain the data for Fig. 36 (e) will be discussed later in this section. This technique is not to be confused with the BR method described earlier, in Section 4.

Intensity distortion for an area of a halftone image is, in essense, the difference between the actual number of white pixels in the area and the number of white pixels needed to preserve the average intensity. The latter may be non-integer. For my computation, I chose the sets of possible values g and N so that this was never the case for the whole image. For SACDH, the number of cylinder chambers n was set to 192 to avoid rounding.

Intensity distortion per pixel

a) b)

c) d)
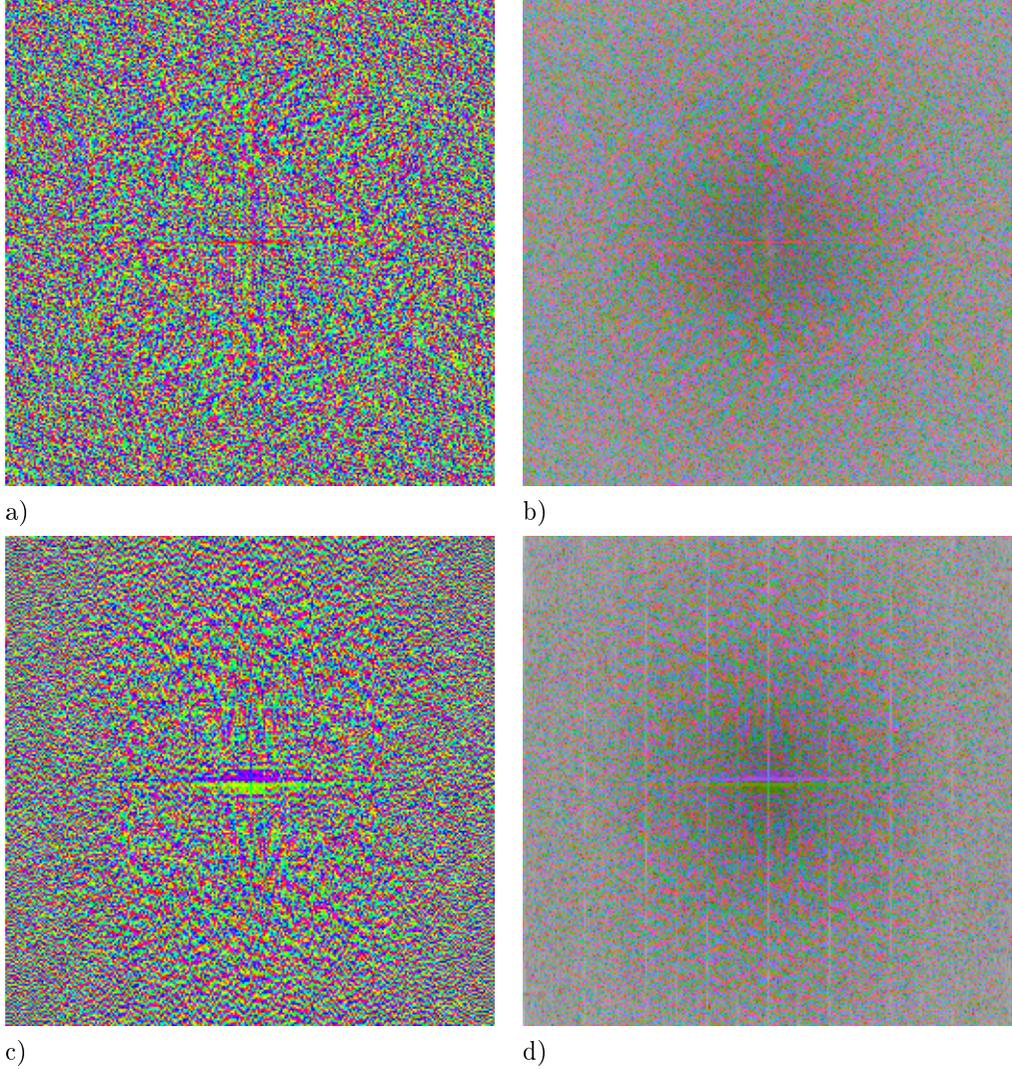
Fig. 25. Four-weight serpentine error diffusion, deterministic weights (Eq. (11)):
The phase spectra of the noise images (left);
the discrete Fourier spectra of the noise images (right).
a), b) For the portrait of Anya Pogosyants
c), d) For the gray scale ramp

$$d = \frac{M}{N^2} \tag{94}$$

was also computed and plotted for some of the algorithms, see Figure 37.

Figures 36 (a) and (b) demonstrate that the absolute value of global intensity distortion for two popular error diffusion algorithms grows approximately linearly in N and $|g - 1/2|$, and the sign of distortion tends to be that of $(g - 1/2)$ most of the time, i.e., the light squares often have too many white pixels in them, and the dark squares tend to contain too few white pixels. I am about to show that this phenomenon is due to the transient boundary effects like the ones seen near the tops of Fig. 5 (c) and Fig. 6 (c). These boundary effects are characteristic of error diffusion [49, 218]. Periodicity seen in Fig. 36 (c) is due to the use of a dither matrix containing each of the values $0, 1, \ldots, \ell_1\ell_2 - 1$. For this particular version of the void-and-cluster algorithm, $\ell_1 = \ell_2 = 128$, so M is zero whenever N is a multiple of 128. The same kind of periodicity causes
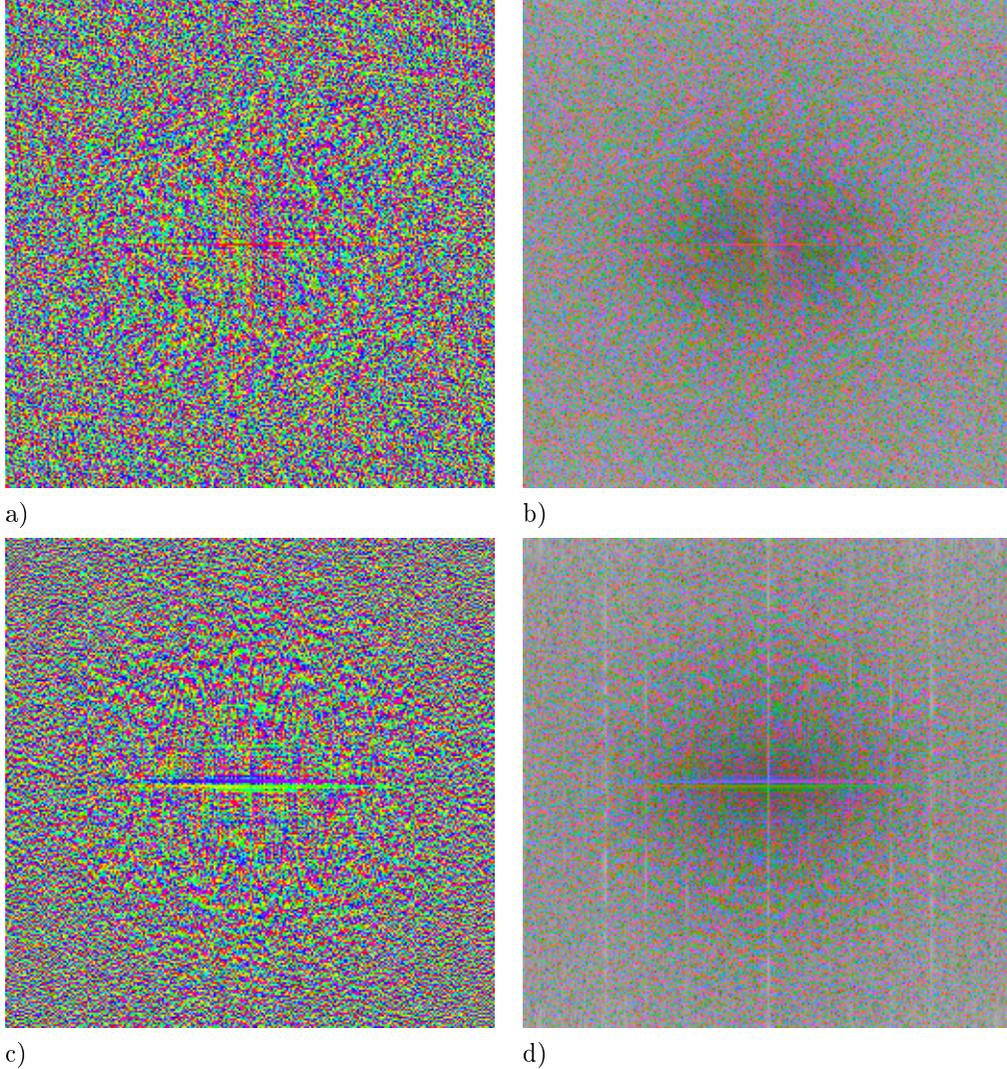
Fig. 26. Three-weight serpentine error diffusion, deterministic weights (Eq. (12)):
The phase spectra of the noise images (left);
the discrete Fourier spectra of the noise images (right).
a), b) For the portrait of Anya Pogosyants
c), d) For the gray scale ramp

our method to indicate absence of intensity distortion when an 8×8 dither matrix from Eq. (4) is used, see Fig. 36 (f). This shows that our primitive measurement technique is not infallible. While the data for SACDH looks good, one should keep in mind that the rounding operation int may cause additional intensity distortion with the absolute value of $N^2/2n$ or more when gn is not an integer. For $N = 464$, $n = 192$, $N^2/2n = 1682/3 \approx 560.67$, and this value is well above those plotted in Fig. 36. The reason of why this is not much of a problem is that this distortion gets spread over the whole image, so the additional intensity distortion per pixel is small everywhere, and, in particular, no extra boundary effects are caused.

Edge enhancement in digital halftoning means distortion of average intensity near the borders separating image areas with different input intensities, such that the average intensity is below the input intensity on the dark side of the edge and above it on the light side of the edge. Presence of quantization noise decreases contrast sensitivity [45], and edge enhancement is widely believed to
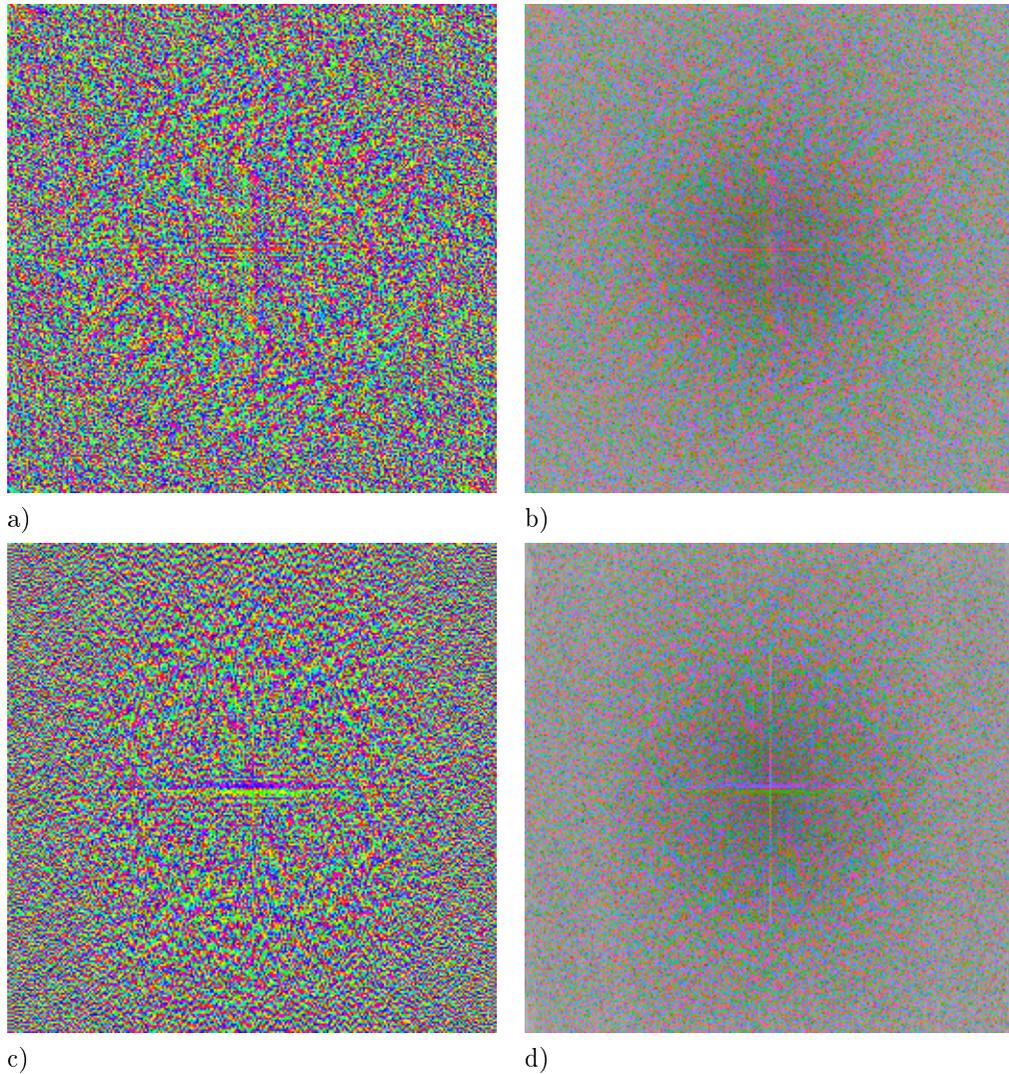
Fig. 27. Four-weight serpentine error diffusion, 50% random weights (Eq. (13)):
The phase spectra of the noise images (left);
the discrete Fourier spectra of the noise images (right).
a), b) For the portrait of Anya Pogosyants
c), d) For the gray scale ramp

be needed to compensate for that [51]. On the other hand, edge enhancement is unwanted when a digital halftoning algorithm is applied in digital holography [57], because, in this case, one is binarizing the Fourier spectrum of the image [191]. Enhancing fluctuations in the Fourier spectrum would thus have the effect of brightening the outer regions of the reconstructed image. In ordinary image visualization and printing, edge enhancement may cause some of the undesirable optical illusions discussed in [79]. This suggests that inherent edge enhancement may also be unwanted in digital halftoning algorithms for medical imaging. In the meanwhile, presence of quantization noise may compensate (undercompensate, overcompensate) for the so-called *Mach-band effect* [175] (when two regions with different gray levels meet at an edge, the eye perceives a light band on the light side of the edge and a dark band on the dark side of the edge; in other words, edges appear to be enhanced even if they aren't). Pappas and Neuhoff [162] opined that "the halftoning algorithm should not compensate for the Mach-band effect".
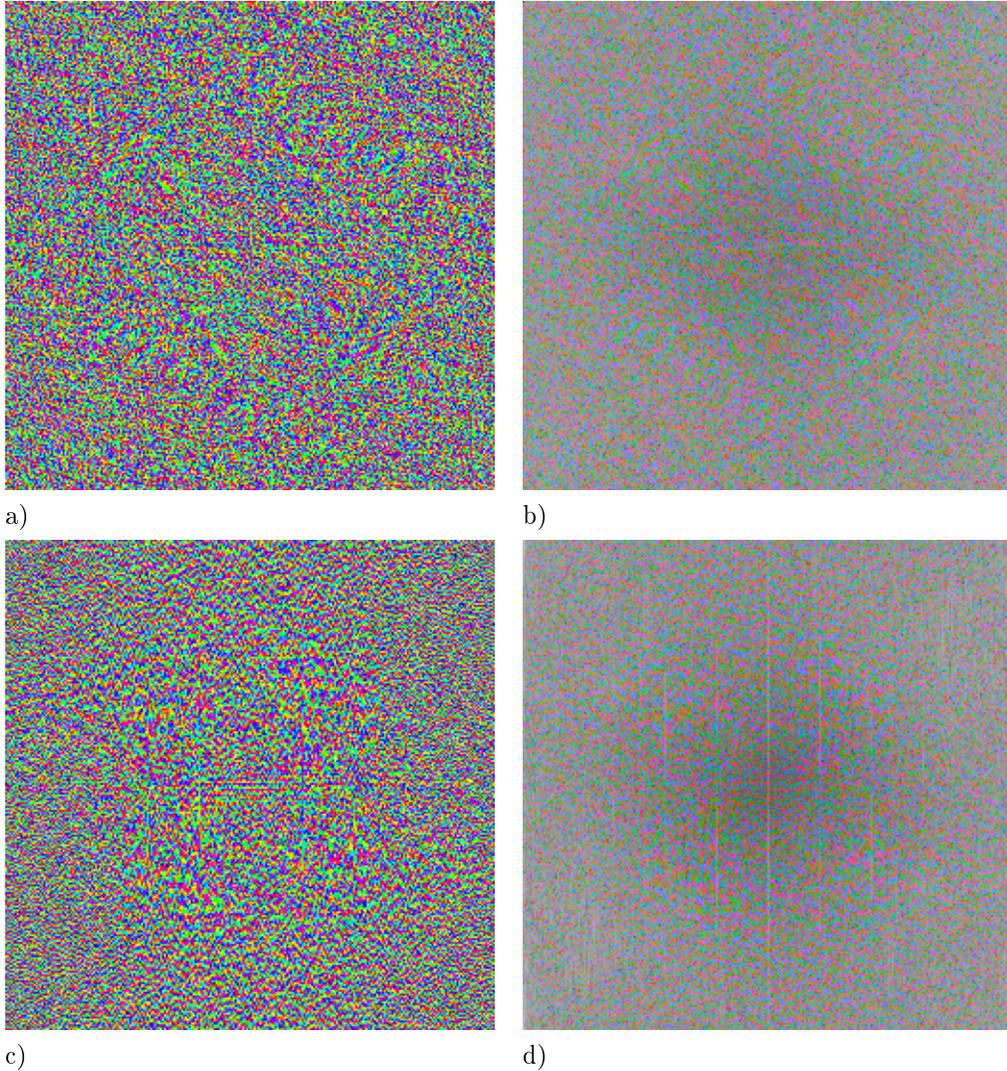
Fig. 28. Error diffusion combined with pulse-density modulation:
The phase spectra of the noise images (left);
the discrete Fourier spectra of the noise images (right).
a), b) For the portrait of Anya Pogosyants
c), d) For the gray scale ramp

Knox [107] showed by measurement that an inherent mechanism for asymmetric edge enhancement was built into the classical Floyd-Steinberg error diffusion algorithm. In a later paper [108], he demonstrated that the edge enhancement was even stronger in the 12-weight error diffusion algorithm by Jarvis, Judice, and Ninke [96], but could not be detected in the halftone images produced using line-by-line delta-sigma modulation. Knox [108] gave a partial explanation of the phenomenon, linking it to a component linear in the input image G being present in the error image. This component is subjected to high-pass filtering. The output of the high-pass filter finds its way into the quantization noise, causing edge enhancement. The mechanisms causing the linear component to appear remained unknown.

Fetthauer and Bryngdahl [57] estimated strength of the linear component for error diffusion on an ordinary raster and used the estimates to modify the original image so that the discrete Fourier spectrum of the noise accompanying error diffusion of the modified image was close to not
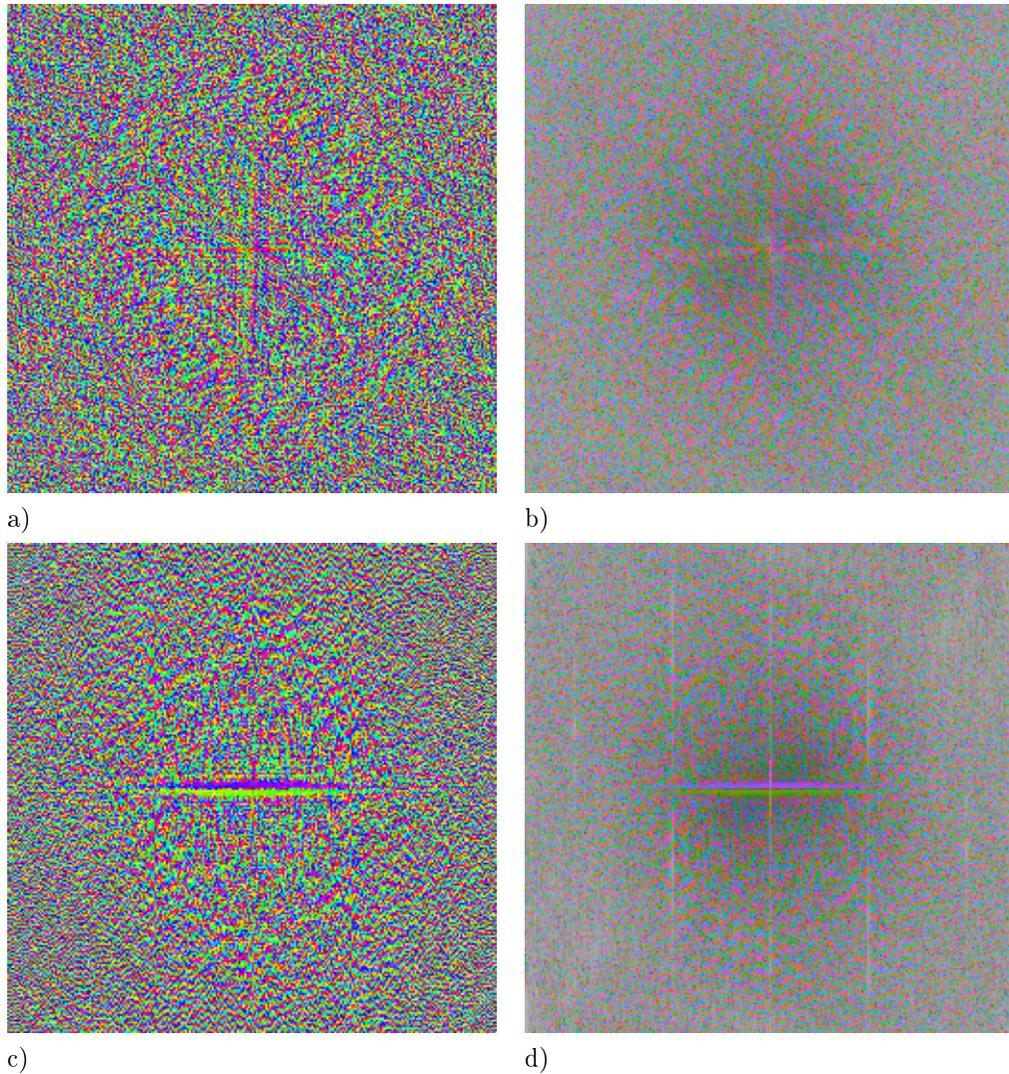
Fig. 29. Error diffusion with intensity-dependent weights (Eq. (14)):
      The phase spectra of the noise images (left);
      the discrete Fourier spectra of the noise images (right).
        a), b) For the portrait of Anya Pogosyants
        c), d) For the gray scale ramp

containing a spectral component proportional to the DFT of the high-pass filtered original image. While the apparent reduction in edge enhancement was achieved, no results of measurements similar to those conducted by Knox [107] for step functions were reported, so it remained unclear just how well their pre-blurring technique worked. The intensity values of the modified image can sometimes wander outside the range $[0, 1]$, causing problems with stability of the error diffusion algorithm.

Subsequent attempts were made [56, 58] to link edge enhancement to a quantization noise component somewhat different from the aforementioned high-pass filtered component of the error image linear in the input image, expose one of the mechanisms causing this quantization noise component to appear, and predict its strength for a particular set of weights for error diffusion on an ordinary raster. These attempts were only partly successful. In particular, it turned out that the strength of the noise component supposedly responsible for edge enhancement is hard to
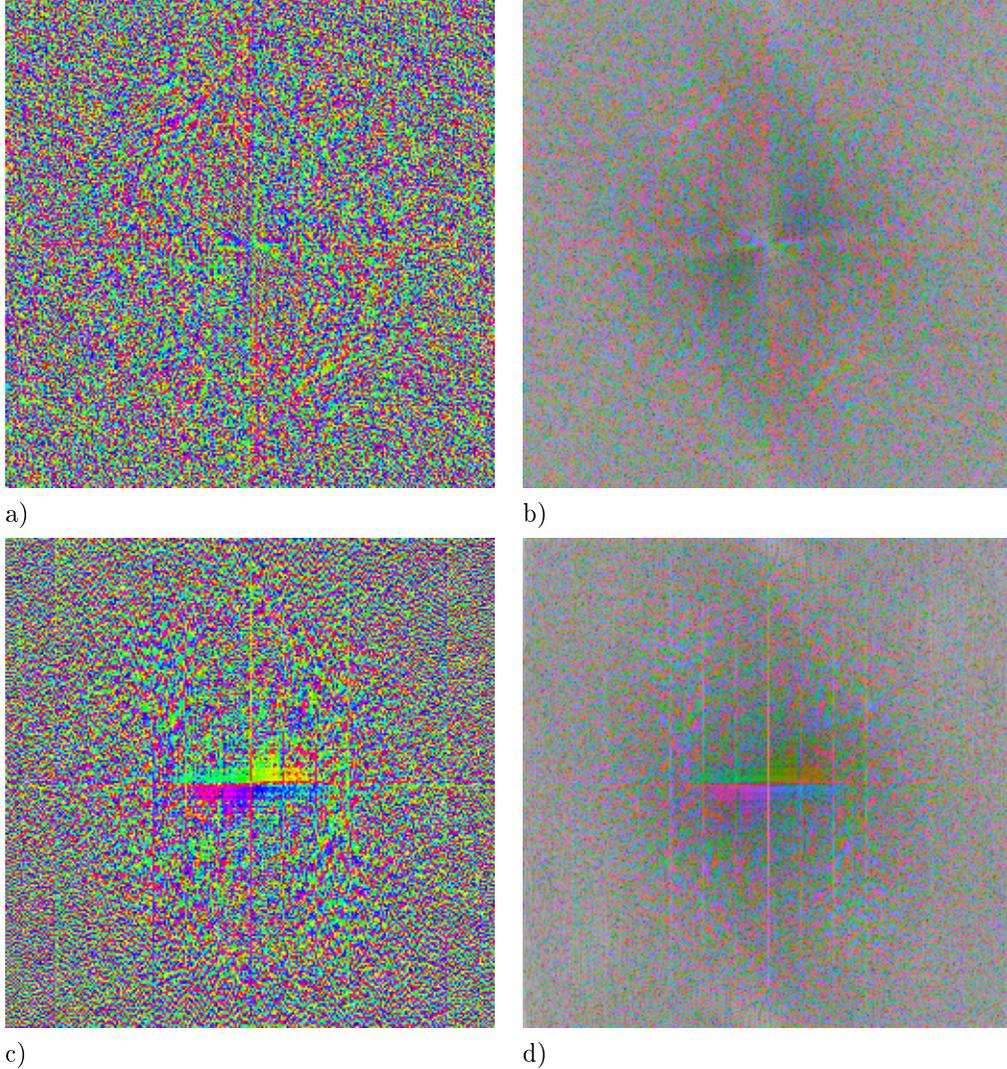
Fig. 30. Error diffusion with threshold modulation using threshold imprints:
The phase spectra of the noise images (left);
the discrete Fourier spectra of the noise images (right).
a), b) For the portrait of Anya Pogosyants
c), d) For the gray scale ramp

predict.

From the results of Sandler et al. [185], it follows that, in line-by-line delta-sigma modulation, the sums $s_{i,j}$ of weighted errors are uniformly distributed on $[-1/2, 1/2)$ for a wide variety of inputs. As a result, the expected values $E(\xi_{i,j})$ remain close to $g_{i,j}$ for all (i,j). This explains why line-by-line delta-sigma modulation causes no detectable edge enhancement.

I studied how the sums $s_{i,j}$ and errors $\epsilon_{i,j}$ are distributed for $N \times N$ constant intensity level representations produced by the classical Floyd–Steinberg error diffusion algorithm with the weights from Eq. (9), and Ulichney's four-weight serpentine error diffusion with the deterministic weights given by Eq. (11). The resulting histograms of the sums and the errors are plotted in Figure 38. The histograms were computed for $g = 1/64, 2/64, \ldots, 63/64$. In Fig. 38, h' stands for "histogram", and the plotted values of h' approximate the corresponding probability densities.

Comparison of Fig. 38 (a) (four-weight SED, $N = 16$) and Fig. 38 (b) (four-weight SED,

a)   b)

c)   d)
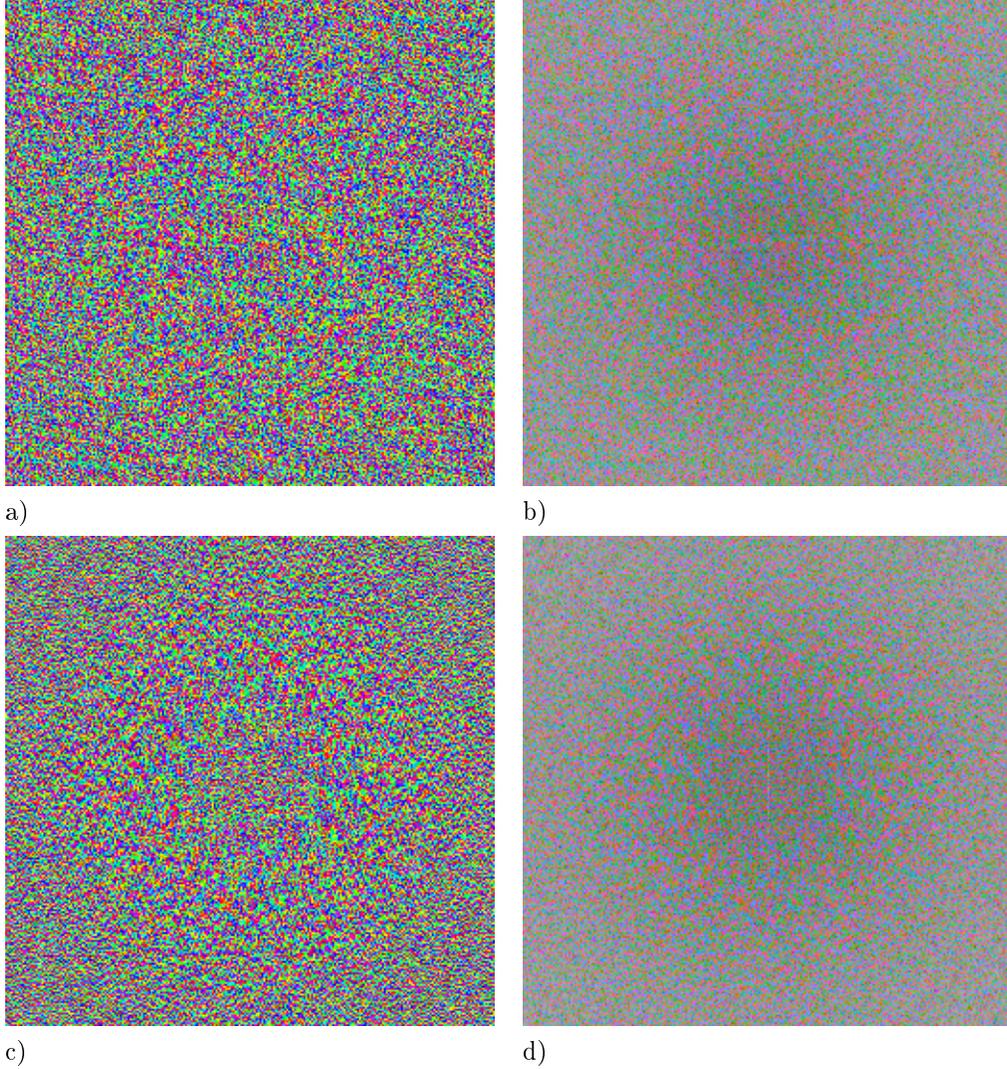
Fig. 31. The iterative convolution algorithm:
The phase spectra of the noise images (left);
the discrete Fourier spectra of the noise images (right).
a), b) For the portrait of Anya Pogosyants
c), d) For the gray scale ramp

$N = 464$) shows that the distributions of $s_{i,j}$ do not become uniform for large N. Instead, highly visible peaks emerge in the distributions for $g = 1/4$, $g = 1/2$, and $g = 3/4$. In the meanwhile, Fig. 37 (a) suggests convergence to other (non-uniform) distributions such that $E(\xi_{i,j}) = g$. For the case of the constant input $g \in [0, 1]$, Eqs. (1,2,5) yield

$$\epsilon_{i,j} = g + s_{i,j} - \lfloor g + s_{i,j} + 1/2 \rfloor, \tag{95}$$

i.e., $\epsilon_{i,j}$ are linked to $s_{i,j}$ so that the distributions of errors are uniquely determined by the distributions of the sums of weighted errors. Comparison of Figures 38 (b) and (c) confirms that.

Near the borders of areas with different input intensities, transitions between different non-uniform distributions of $s_{i,j}$ and $\epsilon_{i,j}$ occur. In particular, whenever the binary quantizer errors are diffused from the pixels with the input intensity g_1 to a pixel at some fixed position (i', j') with the input intensity $g_{i',j'} = g_2 \neq g_1$, $E(\xi_{i',j'})$ may differ significantly from g_2, so the average intensity

51
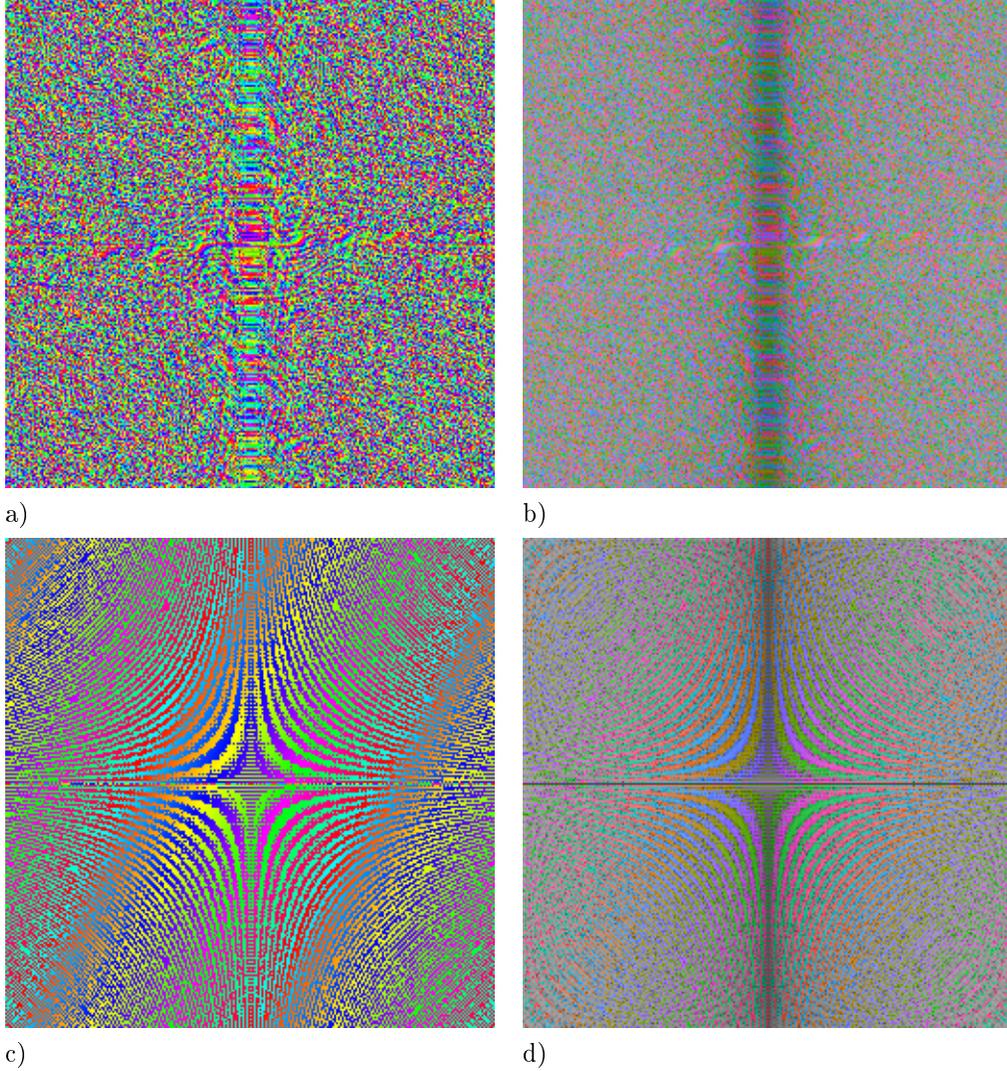
Fig. 32. Line-by-line delta-sigma modulation:
The phase spectra of the noise images (left);
the discrete Fourier spectra of the noise images (right).
a), b) For the portrait of Anya Pogosyants
c), d) For the gray scale ramp

distortion may occur. Indeed, even if the flow of error diffusion went through a large area with the input intensity g_1 before it reached the neighborhood of (i', j'), all it would mean is that $s_{i',j'}$ is distributed so that $E(\xi_{i',j'})$ would be close to g_1 if $g_{i',j'}$ were equal to g_1. But we assumed that $g_{i',j'} = g_2$ is not equal to g_1, so $E(\xi_{i',j'})$ does not have to be close to g_2.

The intensity distortion data plotted in Fig. 36 (e) was obtained by using boundary randomization as follows. Instead of setting the errors outside the image to zero, I computed them as uncorrelated random numbers with the distribution depending on g according to the histogram in Fig. 38 (c). The linearity in g disappeared, and the absolute values of intensity distortion were reduced up to three times. The reduction was especially drastic for the values of g close to zero and one. Alas, the transient boundary effects were not completely eliminated, apparently because the errors generated by error diffusion would not be uncorrelated.

Extending the approach of Knox [107], I measured edge enhancement in $N \times N$ halftone
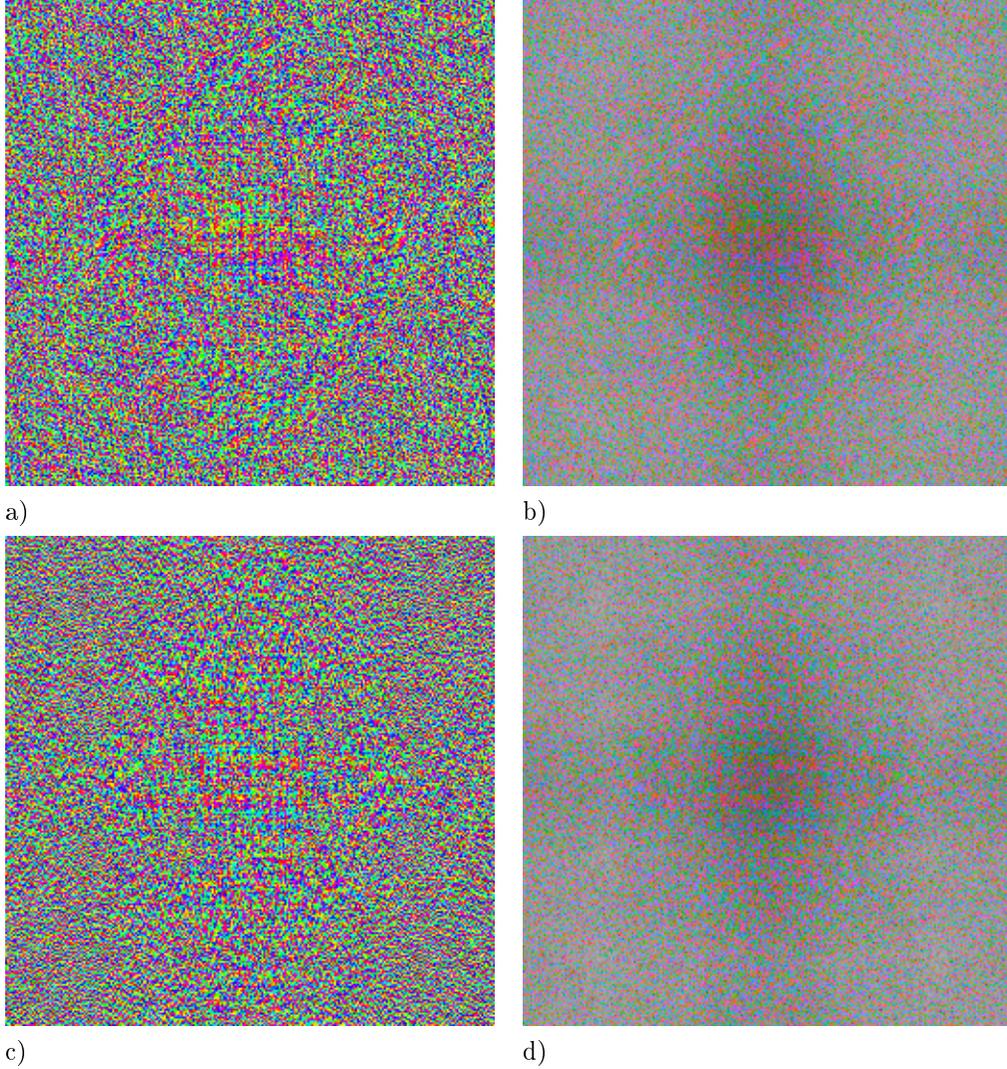
Fig. 33. Serpentine anti-correlation digital halftoning:
The phase spectra of the noise images (left);
the discrete Fourier spectra of the noise images (right).
a), b) For the portrait of Anya Pogosyants
c), d) For the gray scale ramp

images obtained from the digital images of vertical and horizontal grayscale steps using different halftoning algorithms. The input intensity values for the vertical steps were computed according to the formula

$$g_{i,j} = \begin{cases} \frac{1-h}{2} & \text{if } j < N/2, \\ \frac{1+h}{2} & \text{otherwise,} \end{cases} \tag{96}$$

and the input intensity values for the horizontal steps were computed as

$$g_{i,j} = \begin{cases} \frac{1-h}{2} & \text{if } i < N/2, \\ \frac{1+h}{2} & \text{otherwise,} \end{cases} \tag{97}$$

for $h = -1, -31/32, \ldots, 0, \ldots, 31/32, 1$. N was set to 256. Intensity distortion per pixel was computed for the columns of the halftone vertical step images and for the lines of the halftone

Fig. 34. Hybrid images generated starting with the portrait of Anya Pogosyants:
  a) Noise magnitudes: Quantization with a fixed threshold ($s = 0$);
     Noise phases: Three-weight serpentine ED, deterministic weights
  b) Noise magnitudes: Three-weight serpentine ED, deterministic weights;
     Noise phases: Quantization with a fixed threshold ($s = 0$)
  c) Noise magnitudes: SACDH;
     Noise phases: Three-weight serpentine ED, deterministic weights
  d) Noise magnitudes: Three-weight serpentine ED, deterministic weights;
     Noise phases: SACDH

horizontal step images. The results are plotted in Figures 39–44. "Black" means intensity distortion per pixel of -0.25 or less, "white" means intensity distortion per pixel of 0.25 or higher. The plots are made using Maple, which performs bilinear interpolation between the data points. Note that I studied edge enhancement only for the steps with the intensity values symmetric with respect to $1/2$.

As you can see in Figures 39 and 43, error diffusion on an ordinary raster is accompanied by asymmetric edge enhancement of both vertical and horizontal grayscale steps. The edge enhancement seen on the left side of the vertical steps in Fig. 39 is due solely to $w_{0,2} = 3/16$ being nonzero.
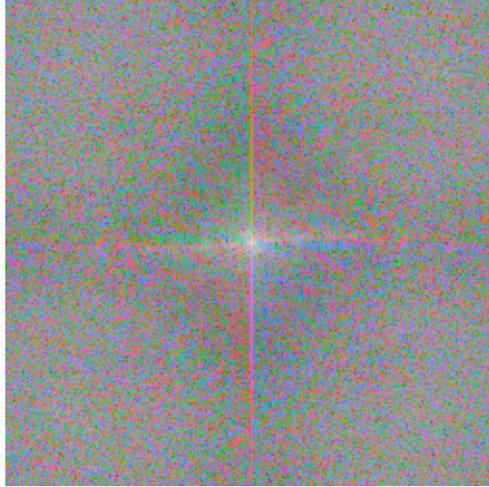
Fig. 35. The noise spectrum for the case of the portrait of Anya Pogosyants
represented by a halftone ramp (SACDH)

The coefficients to the right of column $(\ell - 1)$ allow such algorithms to "see" the approaching edge.

The serpentine raster ensures symmetric edge enhancement of the vertical steps, see Figures 40 (a), 41 (a), and 42 (a). However, the resulting one-pass error diffusion algorithms with wedge-shaped kernels cannot "anticipate" horizontal steps. This is illustrated by Figures 40 (b), 41 (b), and 42 (b). Note that the edge enhancement is not significantly stronger for the three-weight SED algorithm (Fig. 41) than for the four-weight one (Fig. 40). It appears that the three-weight algorithm enhances the horizontal steps more, and the vertical ones less than the four-weight algorithm does.

Fig. 44 shows that serpentine ACDH does not lead to enhancement of symmetric grayscale steps. In addition to that, the stripes of alternating dark and light dots marking the cases of strong correlation in the columns (rows) are not present in Fig. 44, while being easy to spot in Figures 39–43. This confirms that SACDH is good at suppressing vertical and horizontal correlated artifacts.

In Figures 39–44, intensity distortion per pixel for the rows and columns close to the image boundaries was not plotted. This trick allowed us to zoom in on the edges and ignore intensity distortion near the boundaries. Figure 45 shows how intensity distortion linked to the transient boundary effects can sometimes divert attention from, or even completely hide edge enhancement. Figure 46 demonstrates that this is not a problem in the case of SACDH for two obvious reasons. There is no edge enhancement to hide, and no significant intensity distortion occurs near the boundaries.

Whenever edge enhancement is needed to compensate for reduction in contrast sensitivity caused by presence of quantization noise, it can be added to any digital halftoning algorithm, and this extra edge enhancement does not have to be as anisotropic as that embedded in the popular error diffusion algorithms. The rest of this section describes how this is accomplished.

Knuth [111] reformulated the so-called "constrained average" method of Jarvis and Roberts [97] to obtain the following edge enhancement technique.

For $i = 0, 1, \ldots, N_1 - 1$, $j = 0, 1, \ldots, N_2 - 1$, let

M white pixels too many, ED

M white pixels too many, SED

a)

b)

M white pixels too many, V&C

M white pixels too many, SACDH

c)

d)
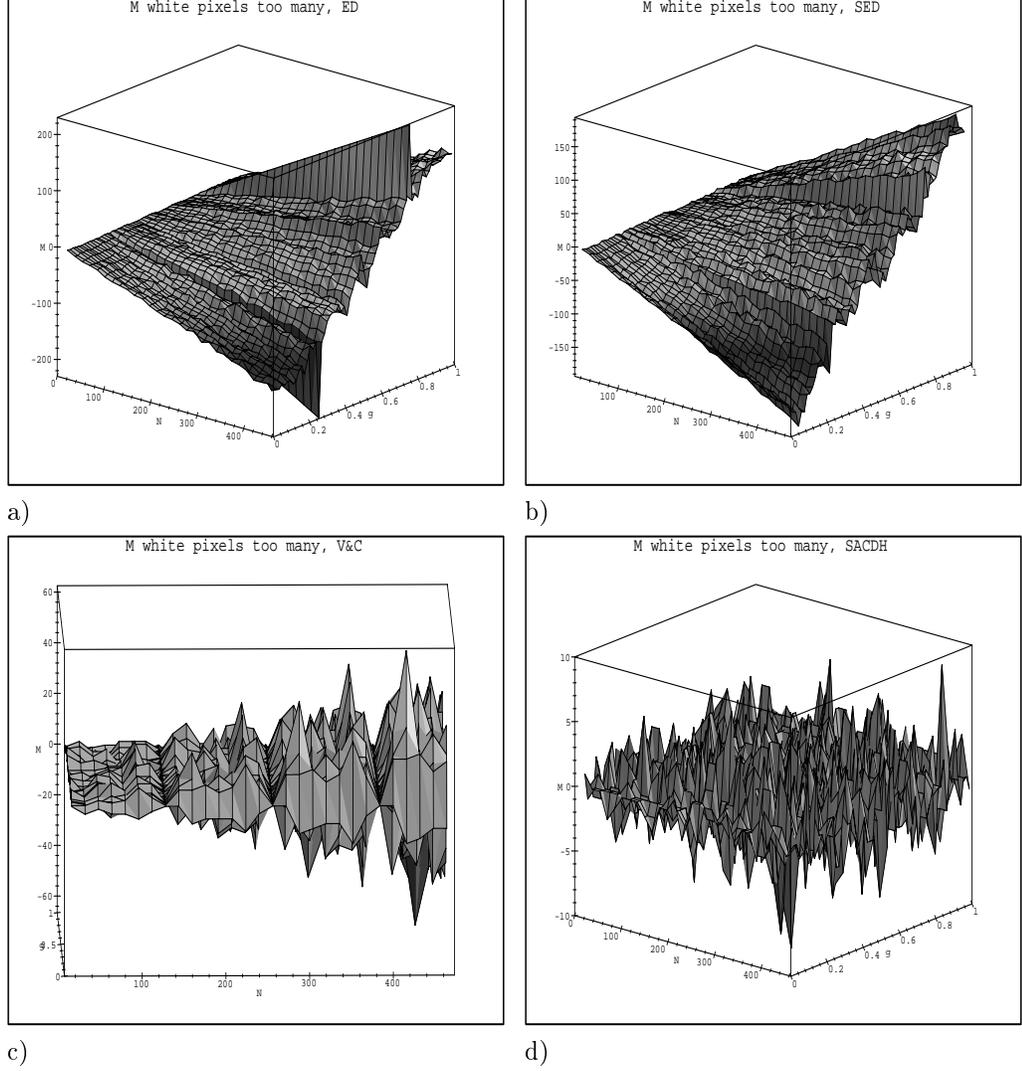
Fig. 36 (Part I). Intensity distortion (Eq. (93)):
a) Classical Floyd–Steinberg error diffusion (Eq. (9))
b) Four-weight serpentine error diffusion, deterministic weights (Eq. (11))
c) Ordered dither with a blue noise mask (void-and-cluster)
d) SACDH ($n = 192$)

Note that

$$\bar{g}_{i,j}(\ell_1, \ell_2) = \begin{cases} \dfrac{1}{\ell_1 \ell_2} \displaystyle\sum_{\tau_1 = -\lfloor \frac{\ell_1}{2} \rfloor}^{\lfloor \frac{\ell_1 - 1}{2} \rfloor} \sum_{\tau_2 = -\lfloor \frac{\ell_2}{2} \rfloor}^{\lfloor \frac{\ell_2 - 1}{2} \rfloor} g_{i + \tau_1, j + \tau_2} & \text{if } \lfloor \frac{\ell_1}{2} \rfloor \leq i < N_1 - \lfloor \frac{\ell_1 - 1}{2} \rfloor \text{ and} \\ & \quad \lfloor \frac{\ell_2}{2} \rfloor \leq j < N_2 - \lfloor \frac{\ell_2 - 1}{2} \rfloor, \\[2mm] g_{i,j} & \text{otherwise.} \end{cases} \tag{98}$$

Note that

$$\bar{g}_{\lfloor N_1/2 \rfloor, \lfloor N_2/2 \rfloor}(N_1, N_2) = \bar{g} \tag{99}$$

is the (global) sample mean of the input image (Eq. (61)). Generally, $\bar{g}_{i,j}(\ell_1, \ell_2)$ are local sample means computed over rectangular areas of the image.

56
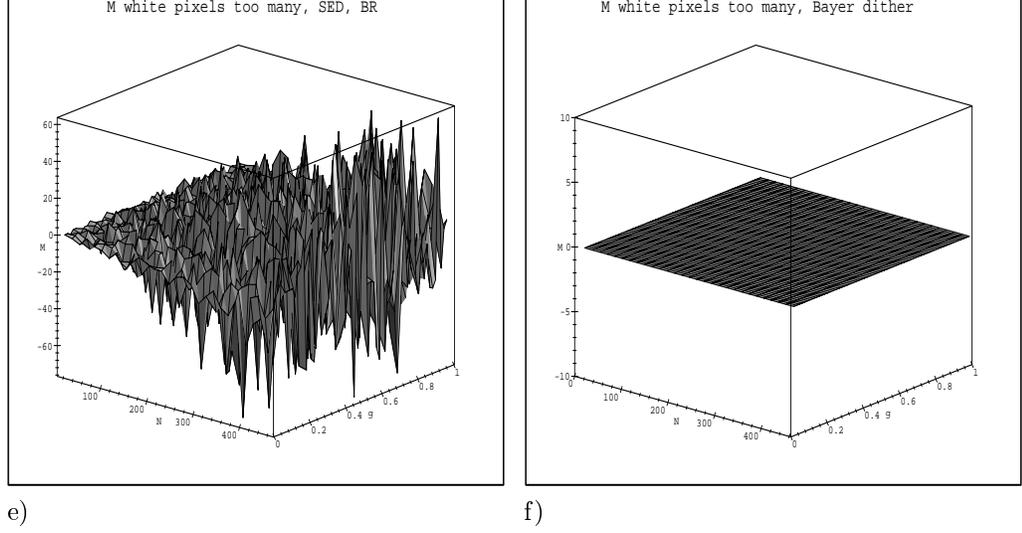
Fig. 36 (Part II). Intensity distortion (Eq. (93)):
     e) Four-weight serpentine error diffusion, deterministic weights, special BR
     f) Ordered dither with a recursive tesselation matrix (Eq. (4))

Knuth, in essence, proposed to replace each input value $g_{i,j}$ with

$$g'_{i,j} = \frac{g_{i,j} - \alpha_1 \bar{g}(3,3)}{1 - \alpha_1} \tag{100}$$

before a digital halftoning algorithm is run. In Eq. (100), α_1 is a constant parameter. Knuth had it set to 0.9. (His actual formulas did not specify how the processing is done near the image boundaries. Eq. (98) incorporates one way to take care of the boundaries. Another simple approach was used to obtain Eq. (58). Eq. (98) also allows ℓ_1 and/or ℓ_2 to be even.)

Let

$$\alpha_2 = \frac{\alpha_1}{1 - \alpha_1}. \tag{101}$$

For $\alpha_1 \neq 1$, Eq. (100) can be rewritten as follows.

$$g'_{i,j} = \frac{g_{i,j}(1 - \alpha_1) + \alpha_1(g_{i,j} - \bar{g}_{i,j}(3,3))}{1 - \alpha_1} = g_{i,j} + \alpha_2(g_{i,j} - \bar{g}_{i,j}(3,3)). \tag{102}$$

From Eq. (102), it is obvious that $g'_{i,j}$ are not guaranteed to stay within the interval $[0,1]$. Many digital halftoning techniques are capable of handling such input, ordered dither and error diffusion among them. However, no ACDH algorithm can process input values outside $[0,1]$, where the meanings of the input intensity values 0 and 1 are as defined in Section 2. Luckily, a simple modification takes care of the problem. The new inputs become

$$g''_{i,j}(\ell_1, \ell_2) = \max\{0, \min\{1, g_{i,j} + \alpha_2(g_{i,j} - \bar{g}_{i,j}(\ell_1, \ell_2))\}\}. \tag{103}$$

Note that the outputs of error diffusion performed on the $N_1 \times N_2$ input images composed of $g'_{i,j}$ and $g''_{i,j}(3,3)$ respectively, for $i = 0, 1, \ldots, N_1 - 1$, $j = 0, 1, \ldots, N_2 - 1$, may be different for the same G and α_2. The corresponding outputs of ordered dither are guaranteed to match.

Figure 47 illustrates how the preprocessing technique described by Eq. (103) can affect the output of SACDH printed at 100 dpi. Only positive values of α_2 lead to edge enhancement, as shown in Figures 47 (d), (e), and (f). $\alpha_2 = 0$ means no preprocessing (see Fig. 15 (a)). If $(-1) \leq \alpha_2 < 0$, the input image is blurred (Figures 47 (b) and (c)). In particular, $\alpha_2 = -1$ means,

57
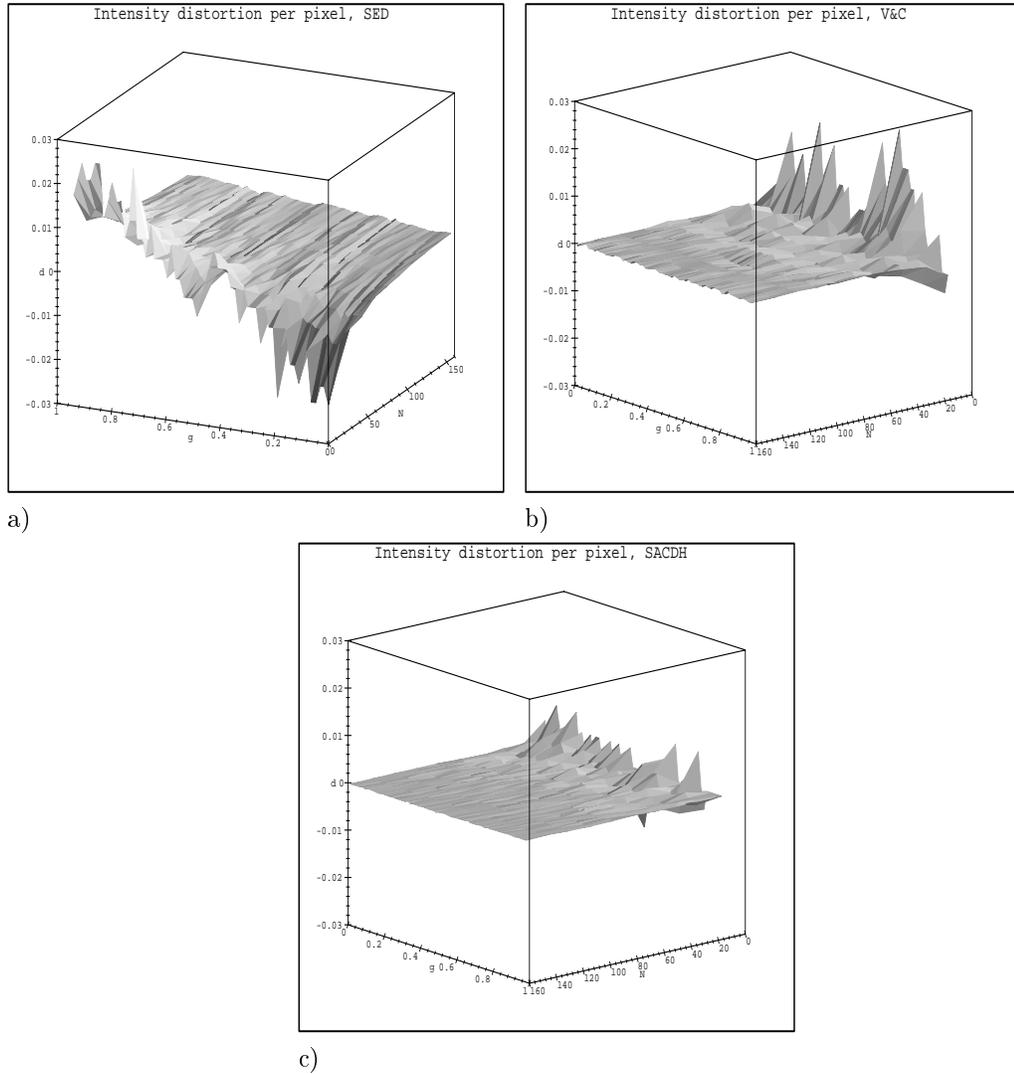
Fig. 37. Intensity distortion per pixel (Eq. (94)):
       a) Four-weight serpentine error diffusion, deterministic weights (Eq. (11))
       b) Ordered dither with a blue noise mask (void-and-cluster)
       c) SACDH ($n = 192$)

in essence, averaging over $\ell_1 \times \ell_2$ windows (Fig. 47 (b)). Finally, setting α_2 to negative values less than (-1) causes amusing "edge anti-enhancement" (Fig. 47 (a)).

Optimum selection of α_2, ℓ_1, and ℓ_2 may present a formidable challenge, the outcome likely depending on the input image G, the output resolution, other viewing conditions and device properties, etc. Other edge enhancement techniques are known ([172], Section 12.4).

8. Extension to Multilevel Halftoning and Color Quantization

For devices capable of displaying more than two different levels of gray (displays, thermo printers, etc.), *multilevel halftoning* algorithms are designed [10, 11, 21, 114, 117, 141, 143, 171, 190, 199, 207, 218, 250]. Some bilevel halftoning algorithms, such as *patterned serpentine diffusion* [184], can be interpreted as multilevel halftoning with subsequent representation of the pixels by apropriate binary patterns. (An implied scale change occurs.)

It is straightforward to extend ACDH to the multilevel case if the quantization levels are
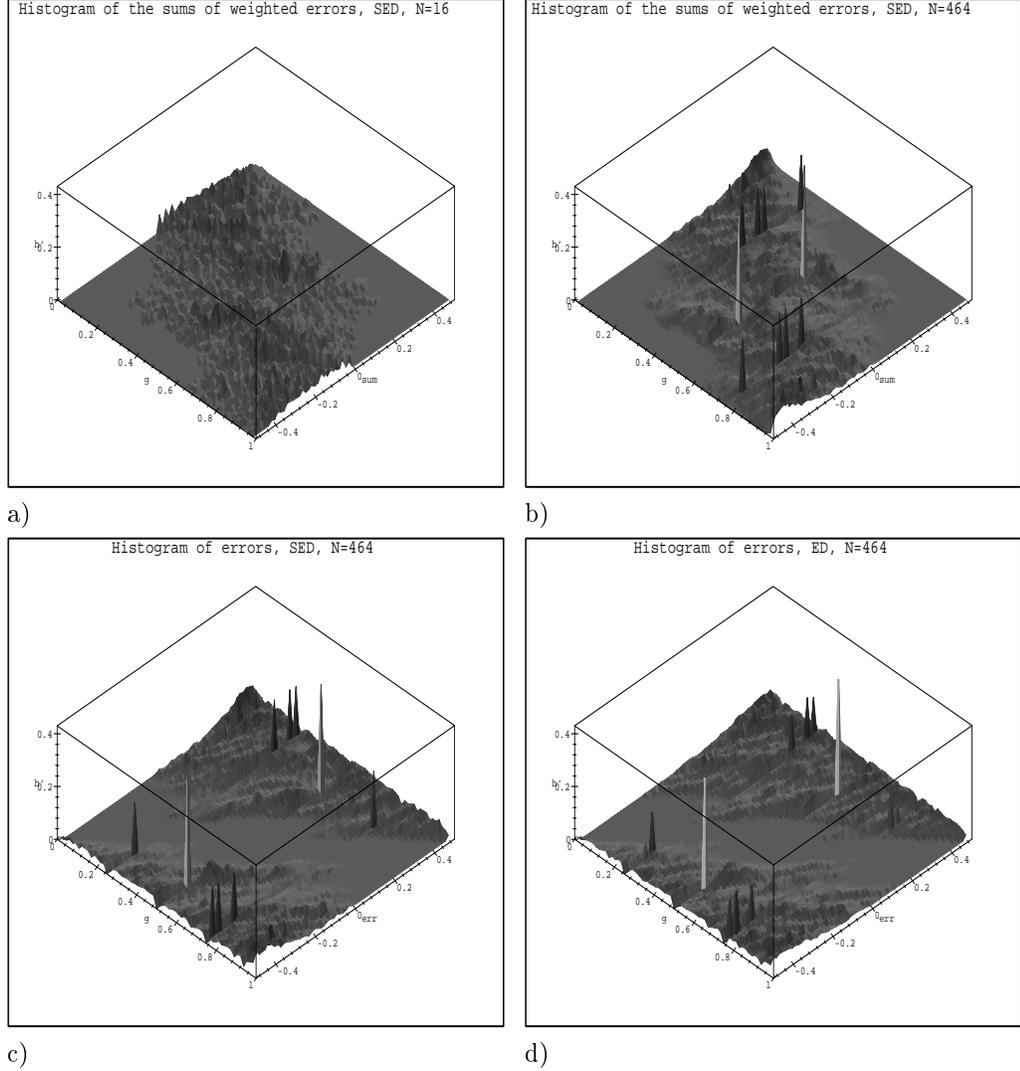
Fig. 38. Histograms of the sums $s_{i,j}$ and the errors $\epsilon_{i,j}$:
      a) Histogram of the sums $s_{i,j}$, four-weight SED (Eq. (11)), $N = 16$
      b) Histogram of the sums $s_{i,j}$, four-weight SED, $N = 464$
      c) Histogram of the errors $\epsilon_{i,j}$, four-weight SED, $N = 464$
      d) Histogram of the errors $\epsilon_{i,j}$, four-weight ED (Eq. (9)), $N = 464$

equidistant, 0 ("black") and 1 ("white") being among them. Let $q > 1$ be an integer, and let $0, 1/q, \ldots, (q-1)/q, 1$ be the equidistant quantization levels. The matrix of $\langle q g_{i,j} \rangle$ becomes the input of a bilevel ACDH algorithm. Then, for $i = 0, 1, \ldots, N_1 - 1$, $j = 0, 1, \ldots, N_2 - 1$, the element of the resulting matrix in the position (i, j) is added to $\lfloor q g_{i,j} \rfloor$. The sums divided by q are the quantization levels we assign to the appropriate pixels of the output image.

If the quantization levels are not equidistant solely because *Weber quantization* [105] is used as means for having coarser quantization in the areas of low contrast sensitivity than in the areas of high contrast sensitivity, then we should translate $g_{i,j}$ to a coordinate system, in which the Weber quantization scale becomes equidistant. Among such coordinate systems, the one, in which all Weber quantization scales are equidistant, is preferred. (A more extensive discussion of the Weber quantization can be found in Appendix B.) The technique described in the previous paragraph is then applied to the transformed input. Alas, this modification cannot be applied when the *Lloyd–*
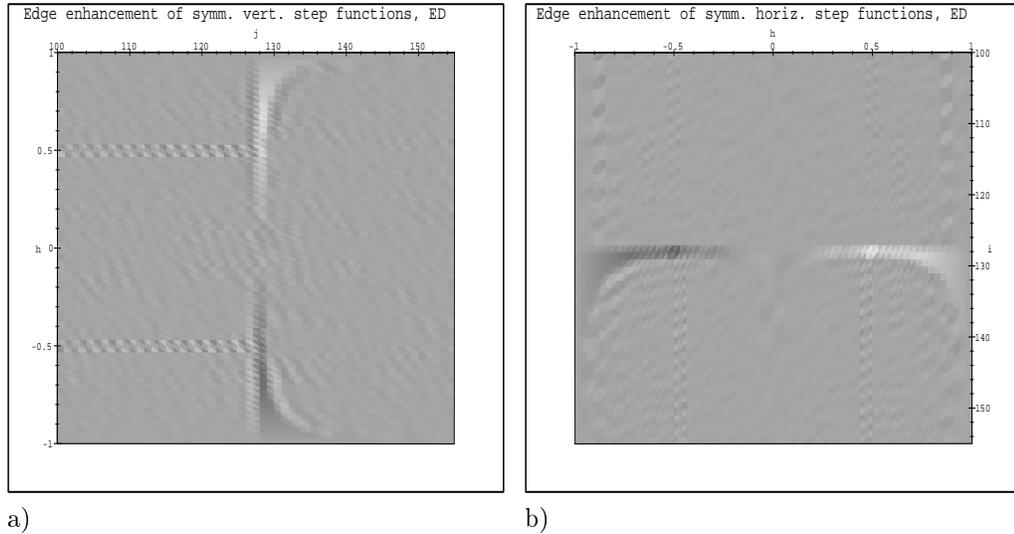
Fig. 39. Edge enhancement: The classical Floyd–Steinberg ED (Eq. (9)), $N = 256$
a) Symmetric vertical grayscale steps
b) Symmetric horizontal grayscale steps
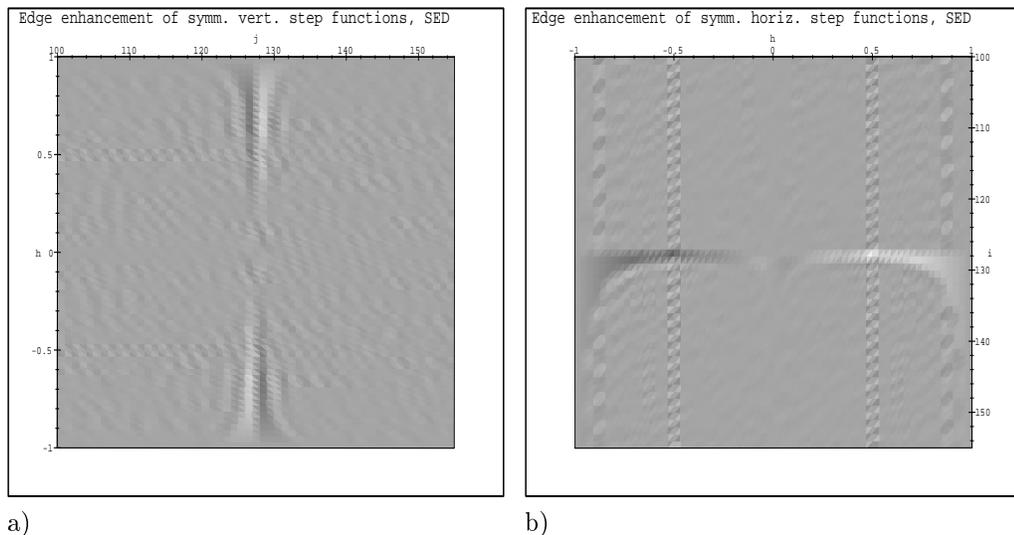
Fig. 40. Edge enhancement: Four-weight SED (Eq. (11)), $N = 256$
a) Symmetric vertical grayscale steps
b) Symmetric horizontal grayscale steps

Max quantization [134, 139] is used, i.e., when the quantization levels are spaced more closely near the peaks of the histogram of $g_{i,j}$. Ideally, these levels for monochrome image quantization should be computed in the system, in which all Weber scales are equidistant. Multilevel error diffusion can work when the quantization levels are selected according to the Lloyd–Max criterion [143]. More research is needed to determine if ACDH can be successfully modified to work in this case.

Techniques used in digital halftoning are often extended to *color quantization* [192, 218], and such terms as *color dithering* [149, 198] and *color halftoning* [104, 142, 194] are sometimes used to describe the resulting algorithms. Color quantization is a separate field of study with its own extensive literature [1, 9, 13, 14, 29, 31, 32, 40, 44, 61, 62, 63, 71, 73, 75, 83, 86, 89, 98, 99, 104, 114, 119, 131, 132, 142, 149, 159, 161, 165, 173, 194, 198, 200, 204, 225, 226, 236, 237, 238, 239,
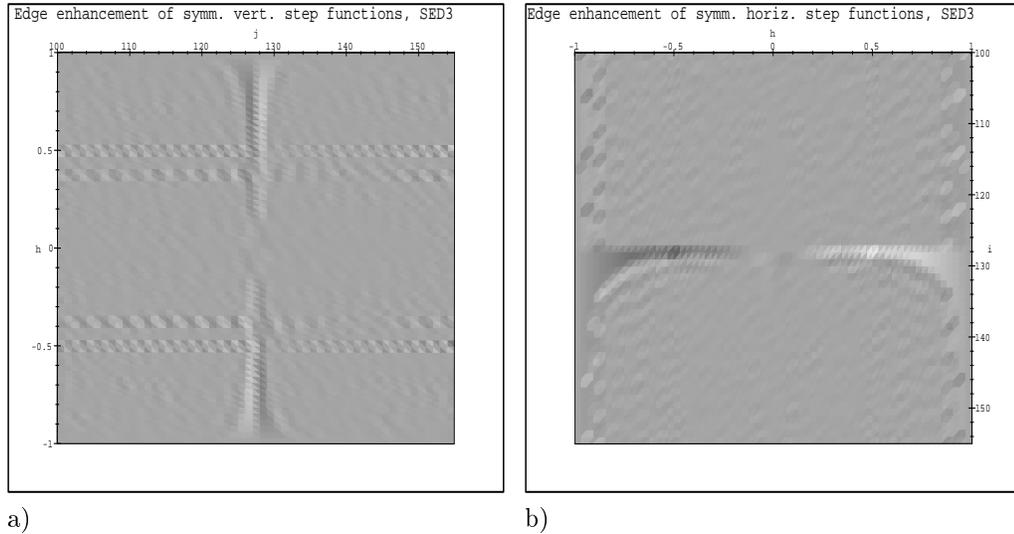
Fig. 41. Edge enhancement: Three-weight SED (Eq. (12)), $N = 256$
a) Symmetric vertical grayscale steps
b) Symmetric horizontal grayscale steps
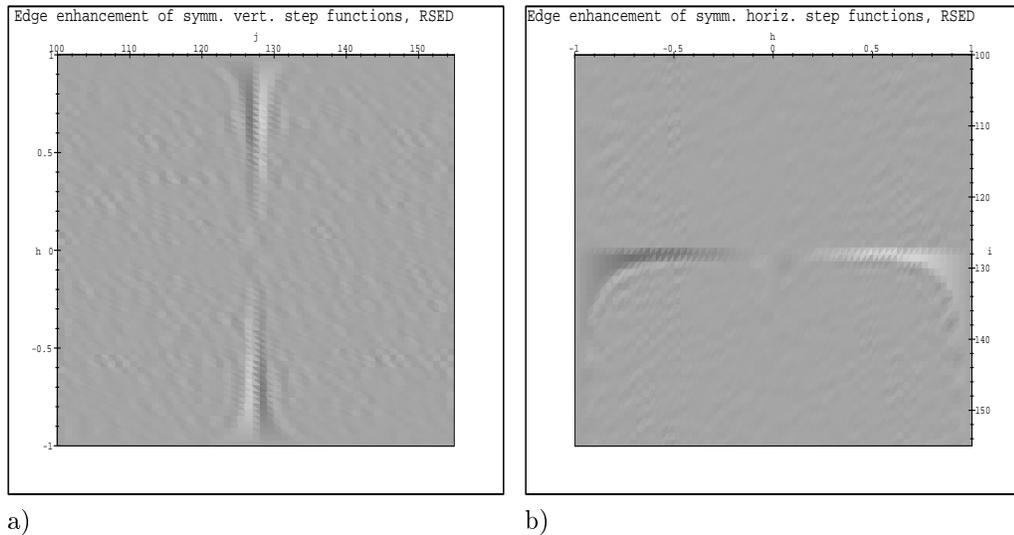
Fig. 42. Edge enhancement: RSED (Eq. (13)), $N = 256$
a) Symmetric vertical grayscale steps
b) Symmetric horizontal grayscale steps

240, 241, 242]. In the recent years, a lot of interest was paid to *color image sequence quantization* [8, 67, 179]. Studies of *color image quality* [30, 92, 116, 148, 197, 215] are often closely related to the color quantization problem.

Two essential steps in color quantization are color palette design [12, 93, 115] and mapping the available color gamut to the color palette. ACDH is easily extendable to the case when the color space is a cube (say, the RGB cube), and the color palette consists of all triples of the form $(k_1/q_1, k_2/q_2, k_3/q_3)$, where q_1, q_2, and q_3 are positive integers, each color coordinate is normalized to fit in $[0, 1]$, $k_1 = 0, 1, \ldots, q_1$, $k_2 = 0, 1, \ldots, q_2$, and $k_3 = 0, 1, \ldots, q_3$. Namely, we can apply multilevel ACDH algorithms from the class described in this section to the color component arrays. For each pixel, the three independently computed levels are interpreted as the coordinates of a

61
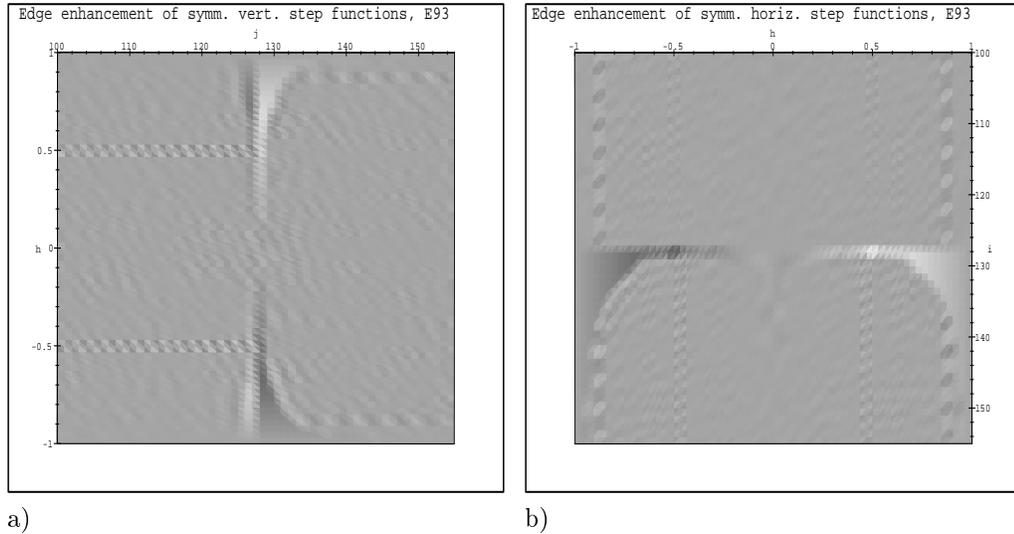
Fig. 43. Edge enhancement: ED with intensity-dependent weights (Eq. (14)), $N = 256$
a) Symmetric vertical grayscale steps
b) Symmetric horizontal grayscale steps
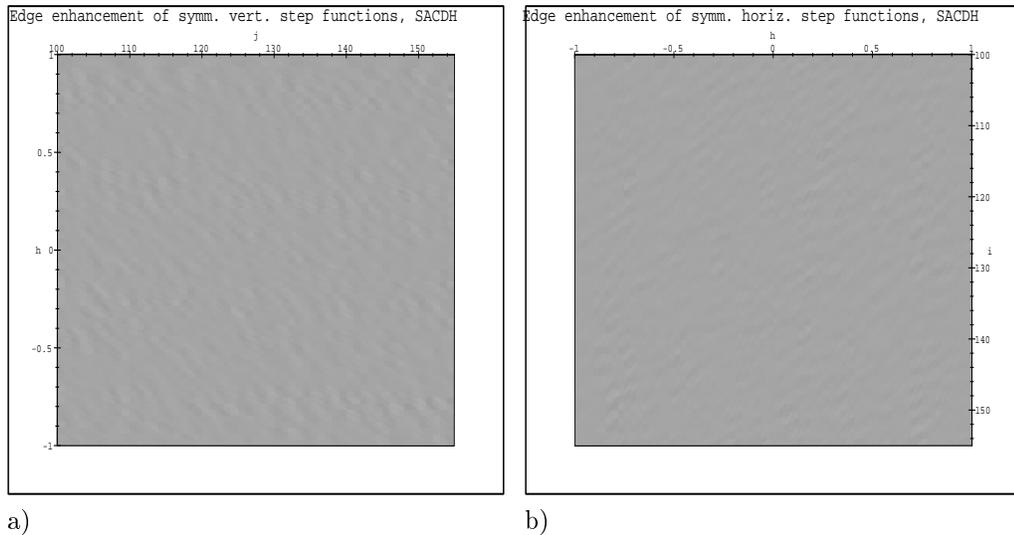
Fig. 44. Edge enhancement: SACDH, $N = 256$
a) Symmetric vertical grayscale steps
b) Symmetric horizontal grayscale steps

palette color. For four-color printing (CMYK), one needs to perform *color separation* before doing halftoning [226], so the same approach may suffice. One should beware the possible *moiré effect* due to the interference of overprinted patterns, though. It is not clear if ACDH can be modified to work in the case of an arbitrary palette. (Error diffusion was extended to this case long ago by Heckbert [86].)

9. Conclusions and Future Research

We introduced a new class of digital halftoning algorithms, anti-correlation digital halftoning (ACDH), and studied a representative of the class, serpentine ACDH. Visual comparison of test images produced by our version of serpentine ACDH and numerous popular benchmark algorithms

a)   b)
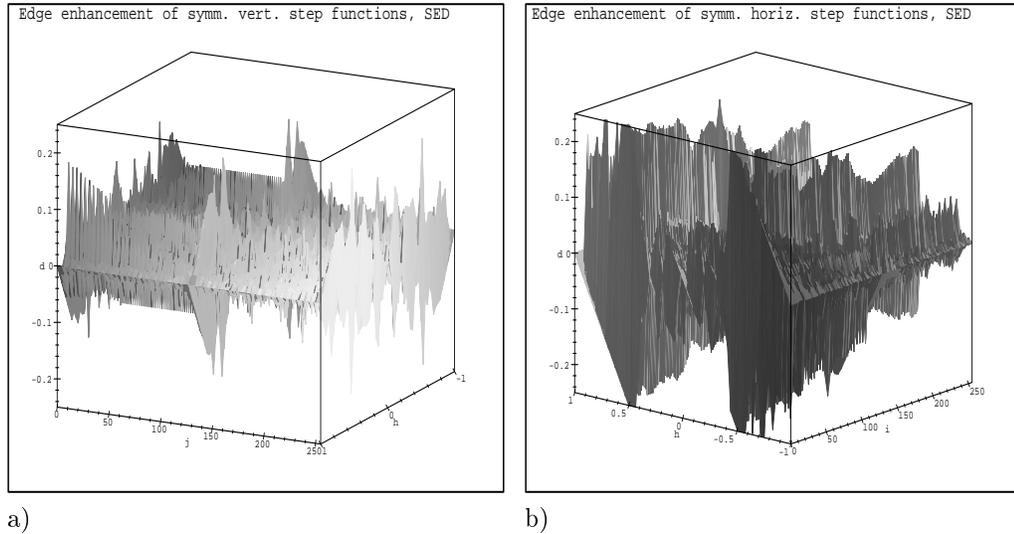
Fig. 45. Intensity distortion per pixel: Four-weight SED (Eq. (11)), $N = 256$
a) Columns of symmetric vertical grayscale steps
b) Rows of symmetric horizontal grayscale steps

a)   b)
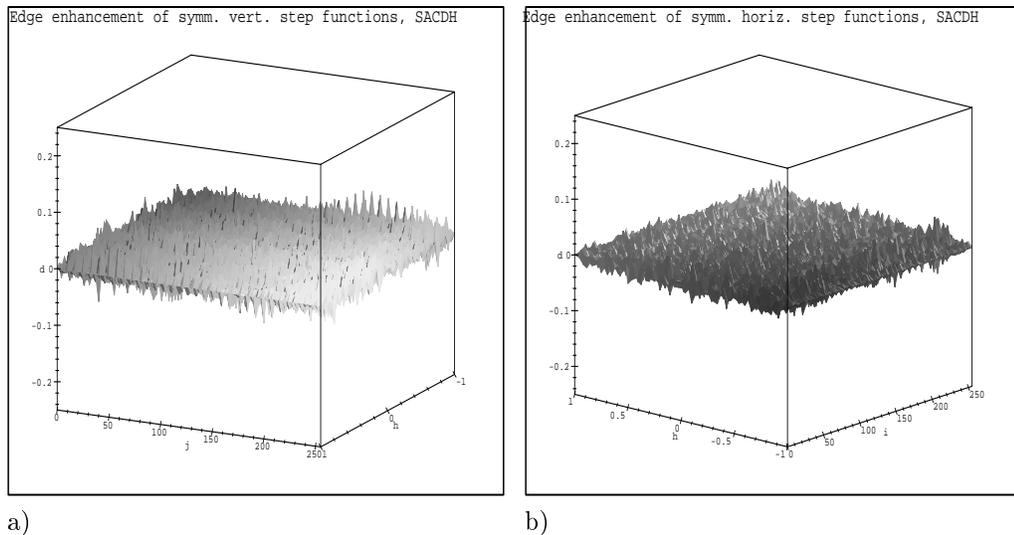
Fig. 46. Intensity distortion per pixel: SACDH, $N = 256$
a) Columns of symmetric vertical grayscale steps
b) Rows of symmetric horizontal grayscale steps

shows that serpentine ACDH causes fewer unpleasant correlated artifacts and less contouring than the benchmark algorithms. The quantization noise spectra associated with serpentine ACDH possess beneficial characteristics related to properties of the vision system. In particular, the inspection of the magnitude spectra showed that the quantization noise associated with serpentine ACDH tends to come close to meeting the requirements of the newly introduced definition of "violet noise". New techniques for color visualization of the noise spectra and the corresponding phase spectra were introduced, and the relative significance of the magnitudes and phases of the discrete Fourier transform of the quantization noise was studied. Unlike some of the benchmark algorithms, serpentine ACDH does not cause significant transient boundary effects. Our measurements indicated that serpentine ACDH does not possess an inherent edge ehancement property, either. They

a)   b)

c)   d)
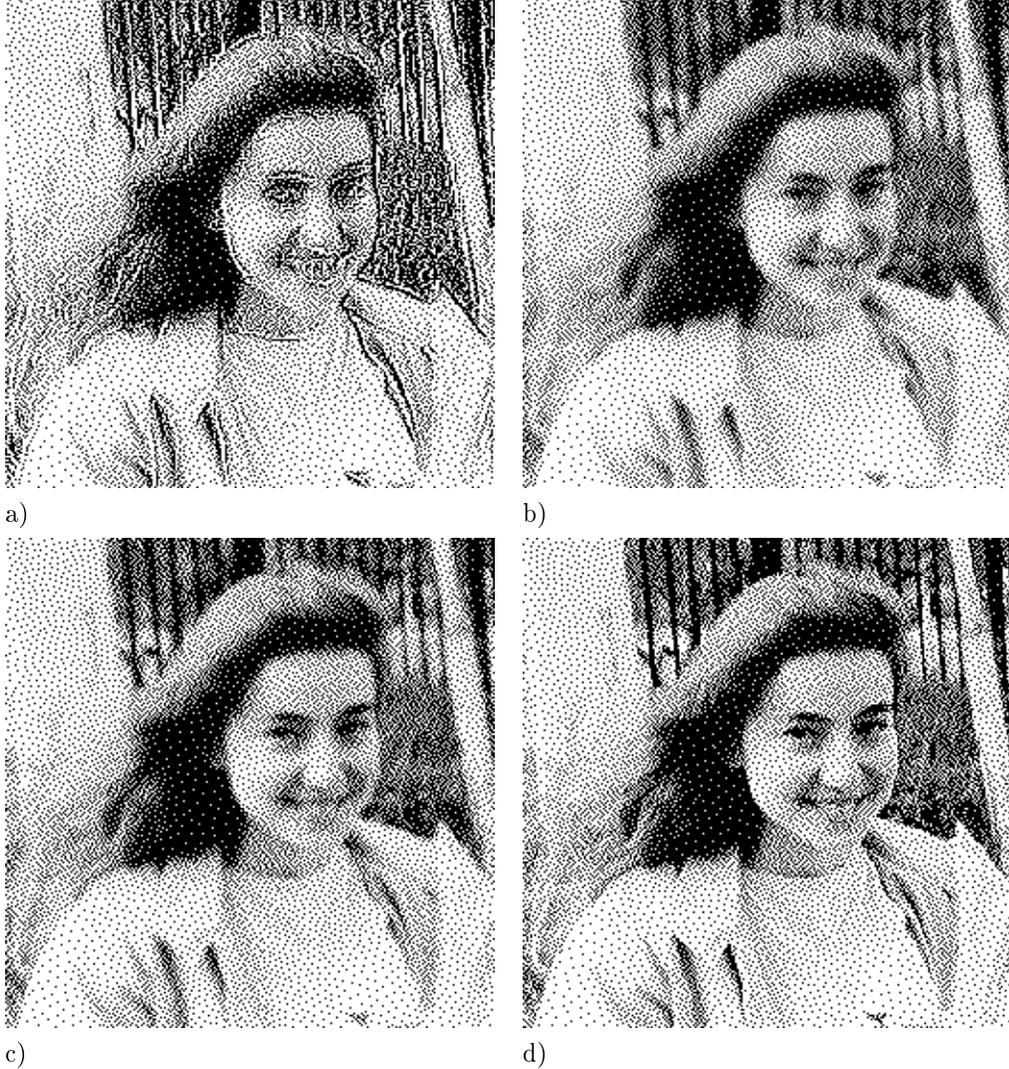
Fig. 47 (Part I). The preprocessed portrait of Anya Pogosyants, SACDH,
100 dpi, $\ell_1 = \ell_2 = 3$: a) $\alpha_2 = -9$; b) $\alpha_2 = -1$; c) $\alpha_2 = -0.5$; d) $\alpha_2 = 1$

also demonstrated that serpentine ACDH is good at reproducing average intensities correctly. We showed that relatively isotropic edge enhancement can be easily added to any digital halftoning algorithm if desired. Other related issues, such as tone scale adjustment, the impact of texture perception on the anti-correlation filter design, and extension of ACDH to multilevel halftoning and color quantization, were discussed.

The prospective directions of the future research are as follows:

1. I am planning to study sequential and parallel iterative (multi-pass) ACDH algorithms. The parallel algorithms using SACDH to determine the initial state of the revolver cylinders and applying cross-shaped anti-correlation filters symmetric with respect to the vertical and horizontal axes and the diagonals are likely to be of special interest, due to the vision system anisotropy.

2. Sequential ACDH algorithms (both one-pass and multi-pass) with the order of pixel processing determined by one or more space-filling curves should be studied.

3. Comprehensive subjective and objective testing of halftone image quality is needed to both evaluate the existing digital halftoning techniques and compare different monochrome vision

64

e)　　　　　　　　　　　　　　　f)

Fig. 47 (Part II). The preprocessed portrait of Anya Pogosyants, SACDH,
100 dpi, $\ell_1 = \ell_2 = 3$: e) $\alpha_2 = 3$; f) $\alpha_2 = 9$

models. Once a reliable and relatively easy-to-compute distortion measure emerges, model-based digital halftoning techniques using halftone images produced by the ACDH algorithms as starting configurations will be developed. These "refinement" techniques are likely to employ hill climbing and/or simulated annealing and perform very high quality halftoning.

4. ACDH algorithms are computationally intensive. I am planning to modify ACDH for designing rectangular binary patterns for look-up-table based halftoning, which is fast. Three-dimensional anti-correlation filters will be used to look at the configurations corresponding to different grayscale levels, for which the binary patterns are about to be generated, so that the correlation between the binary patterns is high for the levels that are close together, and yet the stacking constraint is relaxed. The rectangular constant grayscale input images, from which the binary patterns are going to be generated, will be considered periodic horizontally and vertically as described in Section 3, so no boundary randomization will be involved. The resulting binary patterns will possess the so-called two-dimensional *wrap-around property* [220]. The average intensity distortion measurements discussed in Section 7 show that the ratio of the number of white pixels and the overall number of pixels in a binary pattern may deviate from what the grayscale intensity level prescribes. One way to correct the ratio is to employ a modification of Ulichney's algorithm [221] that removes *minority pixels* (white pixels are the minority pixels if $g < 1/2$, black pixels are the minority pixels otherwise) from the tightest clusters and inserts them into the largest "voids".

5. Visualization of the covariances from Eq. (67) and/or the sums from the right-hand side of this equation may improve our understanding of ACDH. The problem is nontrivial due to the high dimensionality.

6. A comprehensive study of edge enhancement is needed.

7. It would be interesting to establish a firm link between digital halftoning and the information theory. Here's a reference to a related article [182].

Appendix A. Filter selection in SACDH

Anti-correlation filters used in my versions of SACDH are obtained from six similar wedge-shaped basic filters,

$$
K_1 =
\begin{array}{|c|c|c|c|c|c|c|c|c|c|c|c|c|c|c|c|c|c|c|c|c|c|}
\hline
4 & 4 & 5 & 5 & 5 & 5 & 5 & 5 & 6 & 6 & 6 & 6 & 1 & 1 & 0 & 0 & 0 & 0 & 0 & 0 & 0 & 0 \\ \hline
4 & 5 & 5 & 5 & 5 & 5 & 6 & 6 & 6 & 6 & 6 & 6 & 1 & 1 & 1 & 1 & 1 & 0 & 0 & 0 & 0 & 0 \\ \hline
5 & 5 & 5 & 5 & 6 & 6 & 6 & 6 & 7 & 7 & 7 & 7 & 1 & 1 & 1 & 1 & 1 & 1 & 0 & 0 & 0 & 0 \\ \hline
5 & 5 & 5 & 6 & 6 & 6 & 7 & 7 & 7 & 8 & 8 & 8 & 1 & 1 & 1 & 1 & 1 & 1 & 1 & 0 & 0 & 0 \\ \hline
5 & 5 & 6 & 6 & 6 & 7 & 7 & 8 & 8 & 9 & 9 & 9 & 1 & 1 & 1 & 1 & 1 & 1 & 1 & 0 & 0 & 0 \\ \hline
5 & 5 & 6 & 6 & 7 & 8 & 8 & 9 & 10 & 10 & 11 & 11 & 2 & 2 & 1 & 1 & 1 & 1 & 1 & 1 & 0 & 0 \\ \hline
5 & 6 & 6 & 7 & 7 & 8 & 9 & 10 & 11 & 12 & 13 & 13 & 2 & 2 & 2 & 2 & 1 & 1 & 1 & 1 & 1 & 0 \\ \hline
5 & 6 & 6 & 7 & 8 & 9 & 10 & 11 & 13 & 14 & 16 & 20 & 4 & 3 & 3 & 2 & 2 & 1 & 1 & 1 & 1 & 0 \\ \hline
6 & 6 & 7 & 7 & 8 & 10 & 11 & 13 & 15 & 18 & 21 & 21 & 5 & 5 & 4 & 3 & 2 & 1 & 1 & 1 & 1 & 0 \\ \hline
6 & 6 & 7 & 8 & 9 & 10 & 12 & 14 & 18 & 28 & 34 & 45 & 16 & 6 & 5 & 3 & 2 & 2 & 1 & 1 & 1 & 1 \\ \hline
6 & 6 & 7 & 8 & 9 & 11 & 13 & 16 & 21 & 34 & 46 & 64 & 34 & 13 & 5 & 4 & 2 & 2 & 1 & 1 & 1 & 1 \\ \hline
6 & 6 & 7 & 8 & 9 & 11 & 13 & 20 & 21 & 45 & 50 & \times \\ \cline{1-11}
\end{array}
\qquad (104)
$$

$$
K_2 =
\begin{array}{|c|c|c|c|c|c|c|c|c|c|c|c|c|c|c|c|c|c|c|c|c|c|}
\hline
4 & 4 & 5 & 5 & 5 & 5 & 5 & 5 & 6 & 6 & 6 & 6 & 1 & 1 & 0 & 0 & 0 & 0 & 0 & 0 & 0 & 0 \\ \hline
4 & 5 & 5 & 5 & 5 & 5 & 6 & 6 & 6 & 6 & 6 & 6 & 1 & 1 & 1 & 1 & 1 & 0 & 0 & 0 & 0 & 0 \\ \hline
5 & 5 & 5 & 5 & 6 & 6 & 6 & 6 & 7 & 7 & 7 & 7 & 1 & 1 & 1 & 1 & 1 & 1 & 0 & 0 & 0 & 0 \\ \hline
5 & 5 & 5 & 6 & 6 & 6 & 7 & 7 & 7 & 8 & 8 & 8 & 1 & 1 & 1 & 1 & 1 & 1 & 1 & 0 & 0 & 0 \\ \hline
5 & 5 & 6 & 6 & 6 & 7 & 7 & 8 & 8 & 9 & 9 & 9 & 1 & 1 & 1 & 1 & 1 & 1 & 1 & 0 & 0 & 0 \\ \hline
5 & 5 & 6 & 6 & 7 & 8 & 8 & 9 & 10 & 10 & 11 & 11 & 2 & 2 & 1 & 1 & 1 & 1 & 1 & 1 & 0 & 0 \\ \hline
5 & 6 & 6 & 7 & 7 & 8 & 9 & 10 & 11 & 12 & 13 & 13 & 2 & 2 & 2 & 2 & 1 & 1 & 1 & 1 & 1 & 0 \\ \hline
5 & 6 & 6 & 7 & 8 & 9 & 10 & 11 & 13 & 14 & 16 & 16 & 4 & 3 & 3 & 2 & 2 & 1 & 1 & 1 & 1 & 0 \\ \hline
6 & 6 & 7 & 7 & 8 & 10 & 11 & 13 & 15 & 18 & 20 & 21 & 6 & 5 & 4 & 3 & 2 & 1 & 1 & 1 & 1 & 0 \\ \hline
6 & 6 & 7 & 8 & 9 & 10 & 12 & 14 & 18 & 28 & 34 & 44 & 16 & 7 & 5 & 3 & 2 & 2 & 1 & 1 & 1 & 1 \\ \hline
6 & 6 & 7 & 8 & 9 & 11 & 13 & 16 & 20 & 34 & 46 & 64 & 34 & 13 & 6 & 4 & 2 & 2 & 1 & 1 & 1 & 1 \\ \hline
6 & 6 & 7 & 8 & 9 & 11 & 13 & 16 & 21 & 44 & 50 & \times \\ \cline{1-11}
\end{array}
\qquad (105)
$$

$$
K_3 =
\begin{array}{|c|c|c|c|c|c|c|c|c|c|c|c|c|c|c|c|c|c|c|c|c|c|}
\hline
4 & 4 & 5 & 5 & 5 & 5 & 5 & 5 & 6 & 6 & 6 & 6 & 1 & 1 & 0 & 0 & 0 & 0 & 0 & 0 & 0 & 0 \\ \hline
4 & 5 & 5 & 5 & 5 & 5 & 6 & 6 & 6 & 6 & 6 & 6 & 1 & 1 & 1 & 1 & 1 & 0 & 0 & 0 & 0 & 0 \\ \hline
5 & 5 & 5 & 5 & 6 & 6 & 6 & 6 & 7 & 7 & 7 & 7 & 1 & 1 & 1 & 1 & 1 & 1 & 0 & 0 & 0 & 0 \\ \hline
5 & 5 & 5 & 6 & 6 & 6 & 7 & 7 & 7 & 8 & 8 & 8 & 1 & 1 & 1 & 1 & 1 & 1 & 1 & 0 & 0 & 0 \\ \hline
5 & 5 & 6 & 6 & 6 & 7 & 7 & 8 & 8 & 9 & 9 & 9 & 1 & 1 & 1 & 1 & 1 & 1 & 1 & 0 & 0 & 0 \\ \hline
5 & 5 & 6 & 6 & 7 & 8 & 8 & 9 & 10 & 10 & 11 & 11 & 2 & 2 & 1 & 1 & 1 & 1 & 1 & 1 & 0 & 0 \\ \hline
5 & 6 & 6 & 7 & 7 & 8 & 9 & 10 & 11 & 12 & 13 & 13 & 2 & 2 & 2 & 2 & 1 & 1 & 1 & 1 & 1 & 0 \\ \hline
5 & 6 & 6 & 7 & 8 & 9 & 10 & 11 & 13 & 14 & 16 & 16 & 4 & 3 & 3 & 2 & 2 & 1 & 1 & 1 & 1 & 0 \\ \hline
6 & 6 & 7 & 7 & 8 & 10 & 11 & 13 & 15 & 18 & 20 & 21 & 6 & 5 & 4 & 3 & 2 & 1 & 1 & 1 & 1 & 0 \\ \hline
6 & 6 & 7 & 8 & 9 & 10 & 12 & 14 & 18 & 23 & 29 & 32 & 13 & 8 & 5 & 3 & 2 & 2 & 1 & 1 & 1 & 1 \\ \hline
6 & 6 & 7 & 8 & 9 & 11 & 13 & 16 & 20 & 29 & 45 & 64 & 32 & 13 & 6 & 4 & 2 & 2 & 1 & 1 & 1 & 1 \\ \hline
6 & 6 & 7 & 8 & 9 & 11 & 13 & 16 & 21 & 32 & 64 & \times \\ \cline{1-11}
\end{array}
\qquad (106)
$$

$$K_4 = \quad (107)$$

4	4	5	5	5	5	5	5	6	6	6	6	1	1	0	0	0	0	0	0	0	0	0
4	5	5	5	5	5	6	6	6	6	6	6	1	1	1	1	1	0	0	0	0	0	0
5	5	5	5	6	6	6	6	7	7	7	7	1	1	1	1	1	1	0	0	0	0	0
5	5	5	6	6	6	7	7	7	8	8	8	1	1	1	1	1	1	1	0	0	0	0
5	5	6	6	6	7	7	8	8	9	9	9	1	1	1	1	1	1	1	0	0	0	0
5	5	6	6	7	8	8	9	10	10	11	11	2	2	1	1	1	1	1	1	1	0	0
5	6	6	7	7	8	9	10	11	12	13	13	2	2	2	2	1	1	1	1	1	1	0
5	6	6	7	8	9	10	11	13	20	16	16	4	3	3	2	2	1	1	1	1	1	0
6	6	7	7	8	10	11	13	15	18	20	21	6	5	4	3	2	1	1	1	1	1	0
6	6	7	8	9	10	12	20	18	23	32	32	13	8	5	3	2	2	1	1	1	1	1
6	6	7	8	9	11	13	16	20	32	45	64	32	13	6	4	2	2	1	1	1	1	1
6	6	7	8	9	11	13	16	21	32	64	×											

$$K_5 = \quad (108)$$

1	1	1	1	1	1	1	1	1	1	1	1	1	1	0	0	0	0	0	0	0	0	0
1	1	1	1	1	1	1	1	1	1	1	1	1	1	1	1	1	0	0	0	0	0	0
1	1	1	1	1	1	1	1	1	1	1	1	1	1	1	1	1	1	0	0	0	0	0
1	1	1	1	1	1	1	1	1	1	1	1	1	1	1	1	1	1	1	0	0	0	0
1	1	1	1	1	1	1	1	1	1	1	1	1	1	1	1	1	1	1	0	0	0	0
1	1	1	1	1	1	1	1	1	1	1	1	1	1	1	1	1	1	1	1	1	0	0
1	1	1	1	1	1	1	1	1	1	1	1	1	1	1	1	1	1	1	1	1	1	0
1	1	1	1	1	1	1	1	1	2	2	2	1	1	1	1	1	1	1	1	1	1	0
1	1	1	1	1	1	1	1	2	5	7	8	2	1	1	1	1	1	1	1	1	1	0
1	1	1	1	1	1	1	2	5	17	26	26	6	3	1	1	1	1	1	1	1	1	1
1	1	1	1	1	1	1	2	7	26	45	64	24	5	2	1	1	1	1	1	1	1	1
1	1	1	1	1	1	1	2	8	26	64	×											

$$K_6 = \quad (109)$$

1	1	1	1	1	1	1	1	1	1	1	1	1	1	0	0	0	0	0	0	0	0	0
1	1	1	1	1	1	1	1	1	1	1	1	1	1	1	1	1	0	0	0	0	0	0
1	1	1	1	1	1	1	1	1	1	1	1	1	1	1	1	1	1	0	0	0	0	0
1	1	1	1	1	1	1	1	1	1	1	1	1	1	1	1	1	1	1	0	0	0	0
1	1	1	1	1	1	1	1	1	1	1	1	1	1	1	1	1	1	1	0	0	0	0
1	1	1	1	1	1	1	1	1	1	1	1	1	1	1	1	1	1	1	1	1	0	0
1	1	1	1	1	1	1	1	1	1	1	1	1	1	1	1	1	1	1	1	1	1	0
1	1	1	1	1	1	1	1	1	2	2	2	1	1	1	1	1	1	1	1	1	1	0
1	1	1	1	1	1	1	1	2	5	7	6	2	1	1	1	1	1	1	1	1	1	0
1	1	1	1	1	1	1	2	6	17	26	26	6	3	1	1	1	1	1	1	1	1	1
1	1	1	1	1	1	1	2	7	26	45	64	24	5	2	1	1	1	1	1	1	1	1
1	1	1	1	1	1	1	2	5	26	64	×											

by the operator $\mathcal{R}(\tilde{K}, \ell_K, \varepsilon(\ell_K))$. This operator is defined only for $\ell_K \leq \ell_{\tilde{K}}$, where $\tilde{K}$ is an $\ell_{\tilde{K}} \times (2\ell_{\tilde{K}} - 1)$ basic filter. $\mathcal{R}(\tilde{K}, \ell_K, \varepsilon(\ell_K))$ returns an $\ell_K \times (2\ell_K - 1)$ wedge-shaped filter K such

that its columns with numbers less than $(\ell_K - \varepsilon(\ell_K))$ are formed of elements of $\tilde{K}$ located in the appropriate positions with respect to $\times$. The other columns of $\mathcal{R}(\tilde{K}, \ell_K, \varepsilon(\ell_K))$ are filled with zeros. For example,

$$
\mathcal{R}(K_6, 4, -1) =
\begin{array}{|c|c|c|c|c|c|c|}
\hline
2 & 5 & 7 & 6 & 2 & 0 & 0 \\
\hline
6 & 17 & 26 & 26 & 6 & 0 & 0 \\
\hline
7 & 26 & 45 & 64 & 24 & 0 & 0 \\
\hline
5 & 26 & 64 & \times & & & \\
\hline
\end{array}.
\tag{110}
$$

Table A.1 explains how K is computed, depending on Δ from Eq. (75).

Table A.1

Δ	$K(\Delta)$
$\Delta \in \left[0, \dfrac{13}{255}\right)$	$\mathcal{R}(K_1, 6, -5)$
$\Delta \in \left[\dfrac{13}{255}, \dfrac{28}{255}\right)$	$\mathcal{R}(K_2, 6, -5)$
$\Delta \in \left[\dfrac{28}{255}, \dfrac{31}{255}\right]$	$\mathcal{R}(K_3, 3 + \mathrm{rand}(0..1), -\ell_K + 1)$
$\Delta \in \left(\dfrac{31}{255}, \dfrac{45}{255}\right]$	$\mathcal{R}(K_3, 5 + 2 \cdot \mathrm{rand}(0..1), -\ell_K + 1)$
$\Delta \in \left(\dfrac{45}{255}, \dfrac{49}{255}\right]$	$\mathcal{R}(K_3, 5 + \mathrm{rand}(0..2), -\ell_K + 1)$
$\Delta \in \left(\dfrac{49}{255}, \dfrac{88}{255}\right)$	$\mathcal{R}(K_3, 5 + \mathrm{rand}(0..2), -1)$
$\Delta \in \left[\dfrac{88}{255}, \dfrac{94}{255}\right)$	$\mathcal{R}(K_4, 5, -1)$
$\Delta \in \left[\dfrac{94}{255}, \dfrac{95}{255}\right]$	$\mathcal{R}(K_4, 5 + \mathrm{rand}(0..1), -1)$
$\Delta \in \left(\dfrac{95}{255}, \dfrac{100}{255}\right]$	$\mathcal{R}(K_5, 7, -2)$
$\Delta \in \left(\dfrac{100}{255}, \dfrac{106}{255}\right]$	$\mathcal{R}(K_6, 7, -2)$
$\Delta \in \left(\dfrac{106}{255}, \dfrac{111}{255}\right]$	$\mathcal{R}(K_6, 7, -2 - \mathrm{rand}(0..1))$
$\Delta \in \left(\dfrac{111}{255}, \dfrac{120}{255}\right]$	$\mathcal{R}(K_6, 5, -3)$
$\Delta \in \left(\dfrac{120}{255}, \dfrac{121}{255}\right]$	$\mathcal{R}(K_4, 6, -5)$
$\Delta \in \left(\dfrac{121}{255}, \dfrac{122}{255}\right]$	$\mathcal{R}(K_4, 6 + \mathrm{rand}(0..1), -\ell_K + 1)$
$\Delta \in \left(\dfrac{122}{255}, 1\right]$	$\mathcal{R}(K_4, \lceil 255\Delta \rceil - 116, -\ell_K + 1)$

Each random value of the form $\text{rand}(n_1..n_2)$ has to be computed independently for different (i,j), whenever its computation is necessary.

Appendix B. Photometric Measurements and Tone Scale Adjustment

Tone scale adjustment (TSA) ([218], Subsection 1.3.1) means image preprocessing intended to compensate for device distortion of the perceived brightness. It is usually performed by replacing the $N_1 \times N_2$ matrix G of the input intensity values $g_{i,j}$ $(i = 0, 1, \ldots, N_1 - 1, j = 0, 1, \ldots, N_2 - 1)$ with the $N_1 \times N_2$ matrix G' of

$$g'_{i,j} = f(g_{i,j}), \tag{111}$$

where f is a function such that the values $g'_{i,j}$ always lie between 0 and 1. The *tone scale adjustment function* $f(g)$ should not be confused with $\mathbf{f}$ and $f_{u,v}$ found in the main text of this paper. We will call the graphs of the TSA functions the *tone scale adjustment curves*, because of their shape.

Some authors draw distinctions between *brightness* and *lightness* [15, 100, 166], Pratt mixes the two notions ([172], Subsection 7.3.1). The perceived brightness (lightness) of an image area is hard to compute exactly even if the values of such parameters as the area's own luminance, the luminance of background/surround, the luminances of "white" and "black", etc. are known. This is due, in part, to a number of optical illusions [79, 172]. However, we are still interested in the approximations proposed by different researchers, for the following reason.

In Section 2, meanings were assigned to the numerical intensity values $g = 0$ ("black") and $g = 1$ ("white"). In general, this is not enough to determine how a digital image should be reproduced. We need to assign meanings to the intensity values in $(0, 1)$, too. Since the number of different values of g that can be stored in a computer is always finite, we would like to assign the meanings so that, for any two ordered pairs of intensity levels (g_1, g_2) and (g_3, g_4), if $g_1 - g_2 = g_3 - g_4$, then the perceived brightness difference between any two output image areas with their respective digital image intensities equal to g_1 and g_2 tends to remain close to the perceived brightness difference between any two output image areas with their respective digital image intensities equal to g_3 and g_4. The exact version of the requirement above is stricter than the usual conditions imposed in the ordinary Weber quantization, where the multiple quantization levels are selected to be equidistant in a coordinate system such that the *just noticeable differences* are the same for each g. Furthermore, the just noticeable differences cannot simply be integrated to give information about the perceived brightness differences [166], so the exact version of the requirement is impossible to meet. (Other phenomena, such as the optical illusions and the influence of background/surround, share the blame for this.) For the image printing purposes, we are interested in finding an approximate solution that would ensure that the perceived brigntness of the linear-intensity gray scale ramp appears to change approximately linearly when the printed image is well-lit. The image is assumed to be printed on white paper.

Note that, if the input digital image was adjusted to be "correctly" displayed on a monitor such that the linear-intensity gray scale ramp does not seem linear on it when the background/surround is bright, then a different solution is needed. For example, the display luminances corresponding to different grayscale levels could be measured, and the behavior of luminance replicated on paper. In other words, if we want to fully benefit from *Weber printing*, we should use *Weber display*, too.

The choice of a digital halftoning algorithm affects the amount of tone scale adjustment needed [184], as you can see in Fig. 17. I performed a number of photometric measurements on the halftone ramps of the same size and orientation as those in Fig. 17. The ramps were produced by SACDH ($n = 255$) using different TSA functions and printed at 300 dpi or 600 dpi.

I used a precalibrated Minolta LS-100 luminance meter to study how the luminance changes along the vertical axes of the ramps. Between measurements, the halftone ramp was moved in 5 mm increments under a 150 mm $\times$ 150 mm square mask made of black matte art paper and affixed to an almost horizontal surface of a wooden chair placed in a well-lit (indoor) area in my office. The

mask had a 20 mm × 5 mm rectangular window in the middle of it. The shorter edge of the window was kept approximately parallel to the vertical axis of the halftone ramp during the measurement. The luminance meter was mounted on a tripod, approximately three feet above the surface of the chair, and focused on the window in the black mask. Typically, I performed 190 luminance measurements per halftone ramp. A round of measurements consisted of measuring luminance of the round areas corresponding to 18 different positions of the ramp under the mask, one of these positions causing only white paper to be seen through the window, and a separate measurement corresponding to an area covered with black toner being seen through the window. The latter was conducted using a black rectangular image printed on the same printer as the corresponding ramp shortly before or after the ramp was printed. Up to 10 rounds of measurements (passes) per halftone ramp were performed. Note that the round area, the average luminance of which was measured with the luminance meter, included part of the black mask, as well as part of the window, so the absolute values of luminance were irrelevant, only the behavior of the resulting graphs mattered. For each new TSA function, the average luminance graph was obtained by averaging over the data for four halftone ramps printed almost simultaneously on four departmental HP LaserJet IVsi laser printers. The standard deviations of luminances for separate halftone ramps remained small compared to the differences between the ramps. Each iteration meant a change of the TSA function. The goal was to make the next graph of the average luminance function as linear as possible.

Figure 48 shows, among other tone scale adjustment curves, the graphs of two "linear average luminance" TSA functions for printing the halftone ramps (produced using SACDH) at 300 dpi and 600 dpi, marked "c6" and "c7", respectively. The empirical "c1" curve, originally developed by Sandler, Gusev, and Milman in 1992 for printing near-linear average brightness halftone ramps produced by their three-weight version of SED [184] at 300 dpi on LaserJet II laser printers, served as the first approximation. The first iteration of the process described in the previous paragraph led to a new TSA curve I had marked "c3". This curve is not shown in Fig. 48. It is pretty close to the curve marked "c6", and Fig. 48 is rather busy as it is. Additional measurements led to two different curves, "c4" and "c5", for printing at 300 dpi and 600 dpi, respectively. These curves were very close to "c6" and "c7", respectively, and are not shown in Fig. 48, either. Each of the curves marked "c6" and "c7" is, therefore, three iterations away from "c1". (The mnemonic "c2" was used to denote an experimental curve for printing at 600 dpi. I did not find that function especially useful.) I stopped when it became obvious that the influence of changes in the printer conditions occurring between the iterations became comparable to the differences between the TSA curves I was getting. Throughout the process, the luminance differences between the 600 dpi halftone ramps produced using the same TSA functions, but printed on different HP LaserJet IVsi printers, remained disappointingly large compared to the (still very visible) differences between the 300 dpi halftone ramps, so I decided not to include a 600 dpi halftone ramp in the illustrations.

Figure 49 (a) shows the halftone ramp produced using the linear average luminance TSA function "c6". This ramp is apparently too light, which is not surprising, given that the human vision system in the photopic region tends to be more sensitive to the luminance changes in the darker areas of images [85]. (Luminance was formerly called "photometric brightness" [100]. Apparently, the old name went out of style once it became clear that this measure is not close enough to being directly proportional to the perceived brightness.)

The halftone ramp in Figure 49 (b) was produced using the "c1" TSA function of Sandler et al. While the behavior of the perceived brightness of such ramps tends to be close to linear for 300 dpi ramps printed on the laser printers belonging to the HP LaserJet II, III, and IV families, the primitive method of empirical curve adjustment does not seem to be convenient enough if one needs the ability to quickly and reliably find near-linear average brightness TSA functions for Weber printing at different resolutions on different printers.
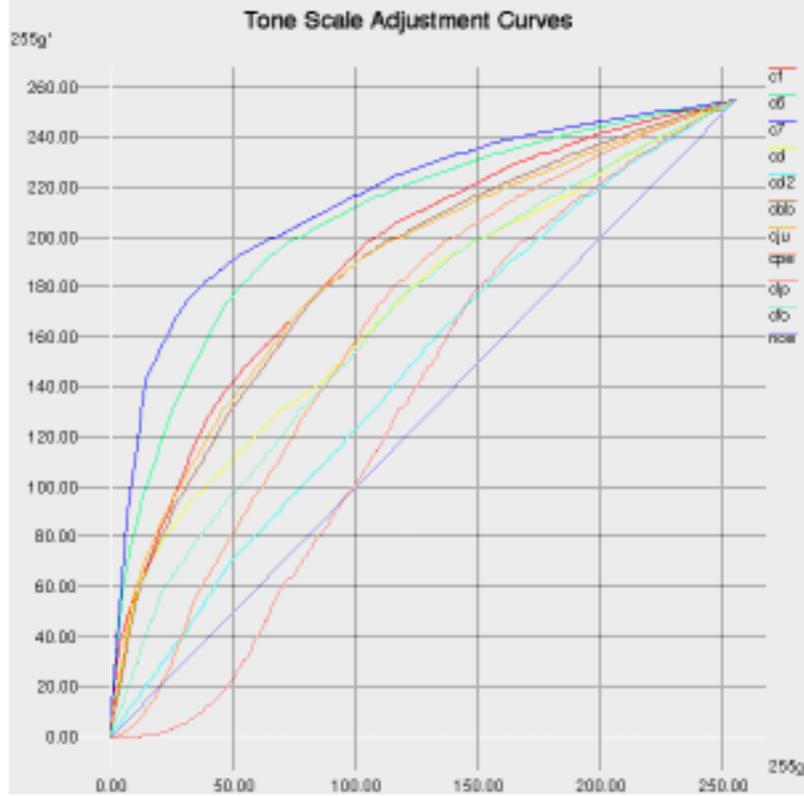
Fig. 48. Tone scale adjustment curves for SACDH
on the HP LaserJet IVsi laser printers:
"c1" — a curve (by Sandler et al.) for linear average perceived brightness (300 dpi);
"c6" — a curve for linear average luminance (300 dpi);
"c7" — a curve for linear average luminance (600 dpi);
"cd" — the first curve for linear average reflection density (300 dpi);
"cd2" — the second curve for linear average reflection density (300 dpi);
"cbb" — a curve for linear average perceived Bartleson–Breneman brightness (300 dpi);
"cju" — a curve for linear average perceived Judd "lightness" (300 dpi);
"cpe" — a curve for square-root average luminance (300 dpi);
"clp" — a curve for cube-root average luminance (300 dpi);
"cfo" — a curve computed using recommendations of Foley et al. [66] (300 dpi);
"noa" — no tone scale adjustment.

The halftone ramps produced without tone scale adjustment tend to be too dark (see Figure 49 (j)), because the printer dots are almost round, so the nearby dots on a square grid have to overlap.

Let Φ_r denote *reflected flux* (flux reflected by sample and used), and let Φ_{rs} denote *reference reflected flux* (flux reflected by reference standard and used). *Reflection density* ([235], Section 15.2) is

$$D_r = -\lg \frac{\Phi_r}{\Phi_{rs}}. \tag{112}$$

Reflection density can be measured with a reflection densitometer, as described in [235]. According to Roetling and Holladay [177], "If Weber's law holds, spacing available levels evenly in density will be the best way to distribute levels for equal visual detectability."

a)   b)   c)

d)   e)   f)
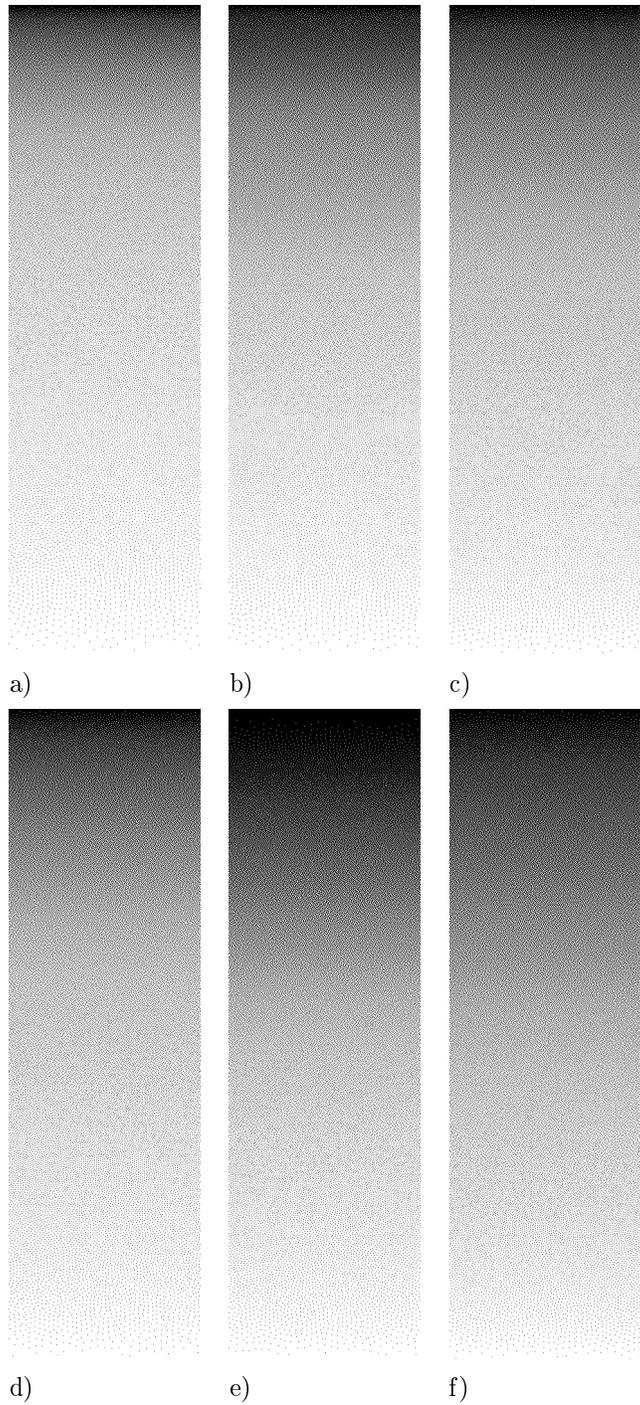
Fig. 49 (Part I). Gray scale ramp, 300 dpi, SACDH
a) Linear average luminance (the "c6" TSA function)
b) The "c1" TSA function (Sandler et al.)
c) Linear average Judd "lightness" (the "cju" TSA function)
d) Linear average Bartleson–Breneman brightness (the "cbb" TSA function)
e) Square-root average luminance (the "cpe" TSA function)
f) The "cfo" TSA function (Foley et al.)
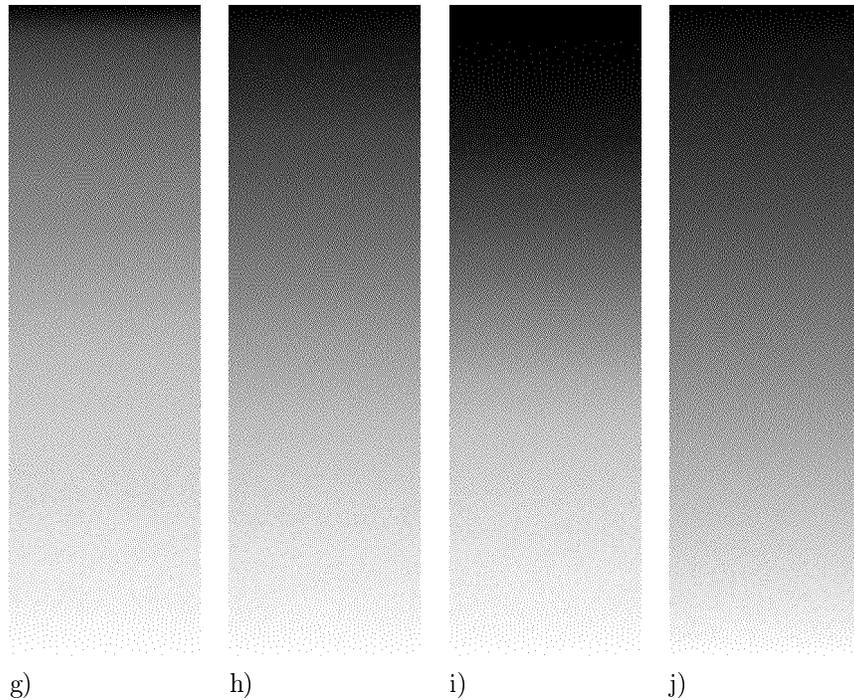
Fig. 49 (Part II). Gray scale ramp, 300 dpi, SACDH
    g) Linear average reflection density, function 1 (the "cd" TSA function)
    h) Linear average reflection density, function 2 (the "cd2" TSA function)
    i) Cube-root average luminance (the "clp" TSA function)
    j) No tone scale adjustment

I used a Speedmaster Universal Densitometer with accuracy ± 0.02 to perform $19 \times 5 = 95$ measurements on a "c3" halftone ramp image and the corresponding black rectangle, for which the luminance measurements had been performed before. That particular halftone ramp image was chosen for its average luminance being very close to linear. Between the measurements done on the ramp, the densitometer was moved along the vertical axis of the ramp in 5 mm increments. This allowed me to perform 18 measurements per pass, starting near the top of the ramp. The nineteenth measurement was performed separately on an area covered with black toner in order to measure the reflection density of "black". The densitometer was calibrated once, just before the series of measurements began. Given the construction of the device, no mask was needed. Three sheets of high-grade white paper were placed beneath the sheet with the image on which the measurements were conducted. The results of the five passes were averaged, and the estimates of the standard deviations of the sample means were computed, none of them above 0.02. The average reflection densities ranged from 1.40 for "black" to 0.11 for "white". The first TSA curve for near-linear average reflection density was then computed numerically from the near-linear average luminance curve "c6". This curve is marked "cd" in Fig. 48, and the corresponding halftone ramp is shown in Fig. 49 (g). Note that, since the TSA functions were being designed for SACDH with $n = 255$, each $f(g)$ was, in fact, a function from $\{0, 1/n, 2/n, \ldots, (n-1)/n, 1\}$ into $\{0, 1/n, 2/n, \ldots, (n-1)/n, 1\}$. Having 19 average reflection density values and 19 average luminance values, I used linear interpolation whenever an intermediate value was needed.

Using the "cd" curve, I applied SACDH to compute a new halftone ramp, which I printed on five departmental HP LaserJet IVsi laser printers, along with the corresponding black rectangles. $20 \times 10 = 200$ reflection density measurements were then performed with the same densitometer, 2 20-measurement passes per halftone ramp. This time, two measurements of the reflection density

73

of "white" were performed during each pass (one near the ramp, one away from the ramp), and the densitometer was recalibrated several times between the passes. The differences between the readings corresponding to the same position in the same ramp proved small compared to the differences between the readings for the same position in the ramps printed on different HP LaserJet IVsi printers. In particular, the reflection density readings of "black" were between 1.31 and 1.34 for three of the printers, and between 1.40 and 1.42 for the other two printers. The reflection density readings of "white" remained between 0.07 and 0.09, 0.08 being the average. Due largely to the difference between the states of the four printers used several weeks earlier to develop the "c6" curve, and the five printers used in this experiment, the "cd" ramps turned out to be too light on average in terms of their reflection density. The second near-linear average reflection density TSA curve was computed from the new measurement data. It is marked "cd2" in Fig. 48, and the corresponding halftone ramp can be seen in Fig. 49 (h). The ramps that measure close to being linear in reflection density seem too dark to me, so I doubt that the perceived brightness is linear in reflection density. (Note that if it were, the coefficient of D_r would have to be negative.)

Bartleson and Breneman [15] conducted subjective measurements to determine how the perceived brightness P in complex images (photographic reproductions and transparencies) depends on luminance L. They came up with the formula

$$P = 10^{2.037 + 0.1401 \cdot \lg(0.3142L) - c_1(L_w) \exp(c_2(L_w) \lg(0.3142L))}, \tag{113}$$

where L_w is the luminance of "white", and the values of the constants $c_1(L_w)$ and $c_2(L_w)$ depend on whether the surround is bright or dark. $0.3142L$ is luminance expressed in millilamberts [100]. (L is measured in cd/m^2.) The luminance measurements conducted in a well-lit area of my office estimated the average luminance of "black" L_b at 13 cd/m^2 and the average luminance of "white" L_w at 169 cd/m^2. While no mask was used in these measurements, so the absolute values make sense, one should keep in mind that luminance varies wildly with the lighting conditions. In particular, the outdoor luminances may be significantly higher than those measured indoors ([91], Chapter 3). My measurements conducted outdoors on a sunny afternoon yielded $L_b = 512$, $L_w = 7790$. However, the values of $c_1(L_w)$ and $c_2(L_w)$ do not change all that much within the photopic range. From a graph in [15], I estimated $c_1(L_w) = c_1(169) = 2$ and $c_2(L_w) = c_2(169) = -0.28$ for the case of the bright surround. Having these values substituted into Eq. (113), I numerically computed the "cbb" TSA curve for near-linear average perceived brightness from the "c6" curve. The "cbb" curve is shown in Fig. 48, and the corresponding halftone ramp can be seen in Fig. 49 (d).

Judd [101] introduced a "lightness" scale that incorporates the background luminance level L_B. According to Judd, "lightness"

$$P = \frac{(L - L_b)(L_B + L_w - 2L_b)}{(L_w - L_b)(L_B + L - 2L_b)}. \tag{114}$$

Judd's formula for the bright background ($L_B = L_w$) becomes

$$P = \frac{2(L - L_b)}{L + L_w - 2L_b}. \tag{115}$$

We want to find a TSA function $f_J(k/n)$, $k = 0, 1, \ldots, n$, such that the "lightness" of the resulting halftone ramp is close to linear. Given the "c6" TSA function $f_L(k/n)$ approximately ensuring that the luminance

$$L(f_L(k/n)) = L_b + \frac{k}{n}(L_w - L_b), \tag{116}$$

we can find $f_J(k/n)$ as $f_L(k'/n)$, where $k' \in [0, n]$ does not have to be an integer, so $f_L(k'/n)$ will be computed using interpolation. Indeed,

$$P(f_J(k/n)) = \frac{k}{n} = \frac{2(L_b + (k'/n)(L_w - L_b) - L_b)}{L_b + (k'/n)(L_w - L_b) + L_w - 2L_b}, \tag{117}$$

so

$$\frac{k}{n} = \frac{2k'}{k' + n}, \tag{118}$$

$$k' = \frac{kn}{2n - k}, \tag{119}$$

and

$$f_J(k/n) = f_L(k'/n) = f_L\left(\frac{k}{2n - k}\right). \tag{120}$$

The values of $f_J(k/n)$ form the TSA curve marked "cju" in Fig. 48. The corresponding halftone ramp is shown in Fig. 49 (c).

Note that the "cbb" curve and the "cju" curve are very close to the independently designed "c1" curve and to each other, well within the "error range" suggested by the difference between the two near-linear average reflection density curves, "cd" and "cd2". Naturally, it is not easy to distinguish between the three corresponding ramps (Fig. 49 (b,c,d)).

Pearson [166] recommended the formula

$$P = \left(\frac{L - L_b}{L_w - L_b}\right)^{\gamma}, \tag{121}$$

where

$$\gamma = \begin{cases} 1/3 & \text{if the surround is dark [120],} \\ 1/2 & \text{if the surround is bright [174].} \end{cases} \tag{122}$$

A simple derivation analogous to the previous one allows to compute the TSA functions with the graphs marked "cpe" (square-root average luminance) and "clp" (cube-root average luminance) in Fig. 48 from the "c6" TSA function $f_L(k/n)$ by the formula

$$f_\gamma(k/n) = f_L\left((k/n)^{1/\gamma}\right). \tag{123}$$

($k' = n(k/n)^{1/\gamma}$.) The resulting halftone ramps are shown in Fig. 49 (e) and (i). Not surprisingly, the cube-root average luminance ramp is obviously too dark.

Foley et al. ([66], Subsection 13.1.1) wrote that "the intensity levels should be spaced logarithmically rather than linearly, to achieve equal steps in brightness." According to their recommendations, we should select a TSA function $f_F(k/n)$ such that

$$L(f_F(k/n)) = L_b \left(\frac{L_w}{L_b}\right)^{k/n}. \tag{124}$$

Substituting $f_L(k'/n)$ for $f_F(k/n)$ in the left-hand side of Eq. (124) and applying Eq. (116) to express $L(f_L(k'/n))$, we get

$$L_b + \frac{k'}{n}(L_w - L_b) = L_b \left(\frac{L_w}{L_b}\right)^{k/n}. \tag{125}$$

Then

$$k' = \frac{nL_b}{L_w - L_b}\left(\left(\frac{L_w}{L_b}\right)^{k/n} - 1\right) \tag{126}$$

and

$$f_F(k/n) = f_L \left(\frac{L_b}{L_w - L_b} \left(\left(\frac{L_w}{L_b} \right)^{k/n} - 1 \right) \right). \tag{127}$$

The resulting "cfo" TSA curve is shown in Fig. 48, and the corresponding halftone ramp can be seen in Fig. 49 (f).

Some of the TSA curves in Fig. 48, including the curves "c6", "cpe", and "cd2", were actually smoothed "by hand" a little bit to reduce jaggedness after their prototypes were computed numerically.

References

1. L. Akarun, Y. Yardimci, and A. E. Çetin, *Adaptive Methods for Dithering Color Images*, IEEE Transactions on Image Processing **6**(7) (1997) pp. 950–955.
2. J. P. Allebach, *Visual Model-Based Algorithms for Halftoning Images*, Proc. of SPIE: Image Quality **310** (1981) pp. 151–157.
3. J. P. Allebach, T. J. Flohr, D. P. Hilgenberg, C. B. Atkins, and C. A. Bouman, *Model-Based Halftoning via Direct Binary Search*, IS&T's 47th Annual Conference/ICPS (1994) pp. 476–482.
5. M. Analoui and J. P. Allebach, *Model Based Halftoning Using Direct Binary Search*, Proc. of SPIE: Human Vision, Visual Processing, and Digital Display III **1666** (1992) pp. 96–108.
4. D. Anastassiou, *Neural Net Based Digital Halftoning of Images*, Proc. of the IEEE International Symposium on Circuits and Systems, IEEE, New York (1988) pp. 507–510.
6. D. Anastassiou, *Error Diffusion Coding for A/D Conversion*, IEEE Transactions on Circuits and Systems **36** (9) (1989) pp. 1175–1186.
7. D. Anastassiou and S. Kollias, *Digital Image Halftoning Using Neural Networks*, Proc. of SPIE: Visual Communications and Image Processing **1001** (1988) pp. 1062–1069.
8. C. B. Atkins, T. J. Flohr, D. P. Hilgenberg, C. A. Bouman, and J. P. Allebach, *Model-Based Color Image Sequence Quantization*, Proc. of SPIE: Human Vision, Visual Processing, and Digital Display V **2179** (1994) pp. 310–317.
9. P. R. Bakić and D. P. Brzaković, *Extension of CNN Based Multilevel Halftoning to Color Reproduction*, Proc. of ICIP-97: 1997 IEEE International Conference on Image Processing V (1997).
10. P. R. Bakić, B. D. Reljin, N. S. Vujović, D. P. Brzaković and P. D. Kostić, *Multilayer Transient-Mode CNN for Solving Optimization Problems*, Proc. of CNNA '96: Fourth IEEE International Workshop on Cellular Neural Networks and their Applications (1996) pp. 25–30.
11. P. R. Bakić, N. S. Vujović, D. P. Brzaković, P. D. Kostić, and B. D. Reljin, *CNN Paradigm Based Multilevel Halftoning of Digital Images*, IEEE Transactions on Circuits and Systems – II **44**(1) (1997) pp. 50–53.

12. R. Balasubramanian and J. P. Allebach, *A New Approach to Palette Selection for Color Images*, Proc. of SPIE: Human Vision, Visual Processing, and Digital Display II **1453** (1991) pp. 58–69.

13. R. Balasubramanian, J. P. Allebach, and C. A. Bouman, *Color-Image Quantization with Use of a Fast Binary Splitting Technique*, Journal of the Optical Society of America A **11**(11) (1994) pp. 2777–2786.

14. R. Balasubramanian, C. A. Bouman, and J. P. Allebach, *Sequential Scalar Quantization of Color Images*, Journal of Electronic Imaging **3**(1) (1994) pp. 45–59.

15. C. J. Bartleson and E. J. Breneman, *Brightness Perception in Complex Fields*, Journal of the Optical Society of America **57**(7) (1967) pp. 953–957.

16. B. E. Bayer, *An Optimum Method for Two-Level Rendition of Continuous-Tone Pictures*, Conference Record, IEEE International Conference on Communications **1**, IEEE, New York (1973) pp. (26-11)–(26-15).

17. T. Bernard, *From Sigma-Delta Modulation to Digital Halftoning of Images*, ICASSP-91: 1991 IEEE International Conference on Acoustics, Speech, and Signal Processing **4** (1991) pp. 2805–2808.

18. C. Billotet-Hoffman and O. Bryngdahl, *On the Error Diffusion Technique for Electronic Halftoning*, Proc. of Society for Information Display **24**(3) (1983) pp. 253–258.

19. F. Bock, H. Walter, M. Wilde, *A New Distortion Measure for the Assessment of Decoded Images Adapted to Human Perception*, Proc. of IWISP '96: Third International Workshop on Image and Signal Processing on the Theme of Advances in Computational Intelligence (1996) pp. 215–218.

20. M. Broja and O. Bryngdahl, *Quantization Noise in Electronic Halftoning*, Journal of the Optical Society of America A **10**(4) (1993) pp. 554–560.

21. M. Broja, K. Michalowski, and O. Bryngdahl, *Error Diffusion Concept for Multi-Level Quantization*, Optics Communications **79** (1990) pp. 280–284.

22. M. Broja, F. Wyrowski, and O. Bryngdahl, *Digital Halftoning by Iterative Procedure*, Optics Communications **69**(3,4) (1989) pp. 205–210.

23. A. E. Burgess, R. F. Wagner, and R. J. Jennings, *Human Signal Detection Performance for Noisy Medical Images*, Proceedings of the International Workshop on Physics and Engineering in Medical Images, IEEE, New York (1982).

24. F. W. Campbell, H. S. Carpenter, and J. Z. Levinson, *Visibility of Aperiodic Patterns Compared with that of Sinusoidal Gratings*, Journal of Physiology (London) **190** (1969) pp. 283–298.

25. F. W. Campbell, J. J. Kulikowski, and J. Z. Levinson, *The Effect of Orientation on the Visual Resolution of Gratings*, Journal of Physiology (London) **187** (1966) pp. 427–436.

26. F. W. Campbell and J. J. Kulikowski, *Orientational Selectivity of the Human Visual System*, Journal of Physiology (London) **187** (1966) pp. 437–445.

27. J. C. Candy, G. C. Temes (Eds.), *Oversampling Delta-Sigma Data Converters*, IEEE Press, New York (1992).

28. P. Carnevali, L. Coletti, S. Patarnello, *Image Processing by Simulated Annealing*, IBM Journal of Research and Development **29**(6) (1985) pp. 569–579.

29. N. Chaddha, W.-C. Tan, and T. H. Y. Meng, *Color Quantization of Images Based on Human Visual Perception*, ICASSP-94: 1994 IEEE International Conference on Acoustics, Speech, and Signal Processing **5** (1994) pp. 89–92.

30. S. S. Chan and R. Nerheim-Wolfe, *An Empirical Assessment of Selected Color-Quantizing Algorithms*, Proc. of SPIE: Human Vision, Visual Processing, and Digital Display V **2179** (1994) pp. 298–309.

31. L.-W. Chang and H.-H. Chang, *Fast Algorithm for Color Vector Quantization*, Proc. of SPIE: Applications of Digital Image Processing XVI **2028** (1993) pp. 106–117.

32. X. Chen, R. Kothari, and P. Klinkhachorn, *Reduced Color Image Based on Adaptive Color Selection Using Neural Networks*, Proc. of the World Congress on Neural Networks **I** (1993) pp. 555–558.

33. W. Chou, P. W. Wong, R. M. Gray, *Multistage Sigma-Delta Modulation*, IEEE Transactions on Information Theory **35**(4) (1989) pp. 784–796.

34. A. J. Cole, *Halftoning without Dither or Edge Enhancement*, The Visual Computer **7** (1991) pp. 232–246.

35. P. C. Cosman, R. M. Gray, and R. A. Olshen, *Evaluating Quality of Compressed Medical Images: SNR, Subjective Rating, and Diagnostic Accuracy*, Proc. of the IEEE, **82**(6) (1994) pp. 919–932.

36. K. R. Crounse, T. Roska, and L. O. Chua, *Image Halftoning with Cellular Neural Networks*, IEEE Transactions on Circuits and Systems **40** (1993) pp. 267–283.

37. J. Dalton, *Perception of Binary Texture and the Generation of Stochastic Halftone Screens*, Proc. of SPIE: Human Vision, Visual Processing, and Digital Display VI **2411** (1995) pp. 207–220.

38. S. Daly, *Subroutine for the Generation of a Two-Dimensional Human Visual Contrast Sensitivity Function*, Easman Kodak Tech. Rep. No. 233203Y (1987).

39. S. Daly, *The Visible Differences Predictor: An Algorithm for the Assessment of Image Fidelity*, in: A. B. Watson (Ed.), Digital Images and Human Vision, The MIT Press, Cambridge, Mass. (1993) pp. 179–206.

40. A. Dekker, *Kohonen Neural Networks for Optimal Colour Quantization*, Network Computation in Neural Systems **5** (1994) pp. 351–367.

41. *Densitometry and Dot Gain Technology Report*, PrePRESS.

42. A. M. Derrington, *Distortion Products in Geniculate X-Cells: A Physiological Basis for Masking by Spatially Modulated Gratings?*, Vision Research **27**(8) (1987) pp. 1377–1386.

43. A. M. Derrington, D. R. Badcock, *Detection of Spatial Beats: Non-Linearity or Contrast Increment Detection?*, Vision Research **26**(2) (1986) pp. 343–348.

44. S. S. Dixit, *Quantization of Color Images for Display/Printing on Limited Color Output Devices*, Computers & Graphics **15**(4) (1991) pp. 561–568.

45. M. P. Eckstein, A. J. Ahumada, Jr., and A. B. Watson, *Visual Signal Detection in Structured Backgrounds. II. Effects of Contrast Gain Control, Background Variations, and White Noise*, Journal of the Optical Society of America A **14**(9) (1997) pp. 2406–2419.

46. R. Ellis, D. Gulick, *Calculus with Analytic Geometry*, Harcourt Brace Jovanovich, San Diego, third edition (1986).

47. R. Eschbach, *Pulse-Density Modulation on Rastered Media: Combining Pulse-Density Modulation and Error Diffusion*, Journal of the Optical Society of America A **7**(4) (1990) pp. 708–716.

48. R. Eschbach, *Reduction of Artifacts in Error Diffusion by Means of Input-Dependent Weights*, Journal of Electronic Imaging **2**(4) (1993) pp. 352–358.

49. R. Eschbach, *Error Diffusion Algorithm with Homogeneous Response in Highlight and Shadow Areas*, Journal of Electronic Imaging **6**(3) (1997) pp. 348–356.

50. R. Eschbach and R. Hauck, *Binarization Using a Two-Dimensional Pulse-Density Modulation*, Journal of the Optical Society of America A **4**(10) (1987) pp. 1873–1878.

51. R. Eschbach and K. T. Knox, *Error-Diffusion Algorithm with Edge Enhancement*, Journal of the Optical Society of America A **8**(12) (1991) pp. 1844–1850.

52. A. M. Eskicioglu, *Application of Multidimensional Quality Measures to Reconstructed Medical Images*, Optical Engineering (Redondo Beach, CA) **35**(3) (1996) pp. 778–785.

53. Z. Fan, *Dot-to-Dot Error Diffusion*, Journal of Electronic Imaging **2**(1) (1993) pp. 62–66.

54. Z. Fan, *Stability Analysis of Error Diffusion*, ICASSP-93: 1993 IEEE International Conference on Acoustics, Speech, and Signal Processing **5** (1993) pp. 321–324.

55. W. Feller, *An Introduction to Probability Theory and its Application*, Vol. 2, John Wiley & Sons, New York, second edition (1971).

56. F. Fetthauer, *Objectabhängige Kontrolle von lokalen Quantisierungsalgorithmen*, Shaker Verlag, Aachen (1997).

57. F. Fetthauer and O. Bryngdahl, *Quantization Noise and the Error Diffusion Algorithm*, Journal of Electronic Imaging **3**(1) (1994) pp. 37–44.

58. F. Fetthauer, O. Bryngdahl, *On the Error Diffusion Algorithm: Object Dependence of the Quantization Noise*, Optics Communications **120** (1995) pp. 223–229.

59. F. Fetthauer and O. Bryngdahl, *Texture Control in Image Quantization by Iterative Wavelet Transform Algorithms*, Journal of the Optical Society of America A **13**(1) (1996) pp. 12–17.

60. F. Fetthauer and O. Bryngdahl, *Image-Dependent Quantization by Iterative Wavelet Algorithms*, Journal of the Optical Society of America A **13**(12) (1996) pp. 2348–2354.

61. E. Fiume and M. Ouellette, *On Distributed, Probabilistic Algorithms for Computer Graphics*, Graphics Interface '89 (1989) pp. 211–218.

62. P. Fletcher, *A SIMD Parallel Colour Quantization Algorithm*, Computers & Graphics **15**(3) (1991) pp. 365–373.

63. T. J. Flohr, B. W. Kolpatzik, R. Balasubramanian, D. A. Carrara, C. A. Bouman, and J. P. Allebach, *Model Based Color Image Quantization*, Proc. of SPIE: Human Vision, Visual Processing, and Digital Display IV **1913** (1993) pp. 270–281.

64. R. W. Floyd and L. Steinberg, *An Adaptive Algorithm for Spatial Grey Scale*, SID 75 Digest, Society for Information Display (1975) pp. 36–37.

65. R. W. Floyd and L. Steinberg, *An Adaptive Algorithm for Spatial Greyscale*, Proc. of Society for Information Display **17**(2) (1976) pp. 75–77.

66. J. D. Foley, A. van Dam, S. K. Feiner, and T. F. Hughes, *Computer Graphics: Principles and Practice*, Addison-Wesley, Reading, Mass., second edition (1990).

67. J. L. Furlani, L. McMillan, and L. Westover, *Adaptive Color Selection Algorithm for Motion Sequences*, Proc. of ACM Multimedia '94 (1994) pp. 341–347.

68. I. Galton, *Granular Quantization Noise in the First-Order Delta-Sigma Modulator*, IEEE Transactions on Information Theory **39**(6) (1993) pp. 1944–1956.

69. J. D. Gaskill, *Linear Systems, Fourier Transforms, and Optics*, John Wiley & Sons, New York (1978).

70. R. Geist, R. Reynolds, and D. Suggs, *A Markovian Framework for Digital Halftoning*, ACM Transactions on Graphics **12**(2) (1993) pp. 136–159.

71. R. S. Gentile, E. Walowit, and J. P. Allebach, *Quantization and Multilevel Halftoning of Color Images for Near-Original Quality*, Journal of the Optical Society of America A **7**(6) (1990) pp. 1019–1026.

72. M. A. Georgeson, T. M. Shackleton, *Perceived Contrast of Gratings and Plaids: Non-Linear Summation Across Oriented Filters*, Vision Research **34**(8) (1994) pp. 1061–1075.

73. M. Gervautz and W. Purgathofer, *A Simple Method for Color Quantization: Octree Quantization*, in: A. S. Glassner (Ed.), Graphics Gems, Academic Press Professional, Cambridge, Mass. (1990) pp. 287–293.

74. G. Goertzel, G. R. Thompson, *Digital Halftoning on the IBM 4250 Printer*, IBM Journal of Research and Development **31**(1) (1987) pp. 2–15.

75. J. R. Goldschneider, E. A. Riskin, and P. W. Wong, *Embedded Multilevel Error Diffusion*, IEEE Transactions on Image Processing **6**(7) (1997) pp. 956–964.

76. R. Gonzalez and P. Wintz, *Digital Image Processing*, Addison-Wesley, Reading, Mass., second edition (1987).

77. R. M. Gray, *Oversampled Sigma-Delta Modulation*, IEEE Transactions on Communications **35**(5) (1987) pp. 481–489.

78. T. A. Grogan and D. Keene, *Image Quality Evaluation with a Contour-Based Perceptual Model*, Proc. of SPIE: Human Vision, Visual Processing, and Digital Display III **1666** (1992) pp. 188–197.

79. S. Grossberg and D. Todorović, *Neural Dynamics of 1-D and 2-D Brightness Perception: A Unified Model of Classical and Recent Phenomena*, in: S. Grossberg (Ed.), Neural Networks and Natural Intelligence, The MIT Press, Cambridge, Mass. (1988) pp. 127–194.

80. D. A. Gusev, G. Y. Milman, E. A. Sandler, *Principles of Optimal Rasters Application to Pattern Recognition Problems*, in: N. N. Evtikhiev (Ed.), Voprosy Kibernetiki, Ustroystva i Sistemy (MIREA Transactions), Moscow Institute of Radioengineering, Electronics, and Automation, Moscow (1992) pp. 18–29 [in Russian].

81. C. F. Hall and E. L. Hall, *A Nonlinear Model for the Spatial Characteristics of the Human Visual System*, IEEE Transactions on Systems, Man, and Cybernetics, **7**(3) (1977) pp. 161–170.

82. P. Hamill, *Line Printer Modification for Better Grey Level Pictures*, Computer Graphics and Image Processing **6** (1977) pp. 485–491.

83. H. Haneishi, T. Suzuki, N. Shimoyama, and Y. Miyake, *Color Digital Halftoning Taking Colorimetric Color Reproduction into Account*, Journal of Electronic Imaging **5**(1) (1996) pp. 97–106.

84. N. He, F. Kuhlmann, A. Buzo, *Multi-Loop Sigma-Delta Quantization*, IEEE Transactions on Information Theory **38**(2) (1992) pp. 1015–1028.

85. S. Hecht, *A Theory of Visual Intensity Discrimination*, Journal of General Physiology **18** (1935) pp. 767–789.

86. P. S. Heckbert, *Color Image Quantization for Frame Buffer Display*, Computer Graphics (Proc. of SIGGRAPH '82) **16**(3) (1982) pp. 297–307.

87. S. Hein and A. Zakhor, *Halftone to Continuous-Tone Conversion of Error-Diffusion Coded Images*, IEEE Transactions on Image Processing **4**(2) (1995) pp. 209–216.

88. K. Hosaka, *A New Picture Quality Evaluation Method*, Proceedings of the International Picture Coding Symposium, Tokyo, Japan (1986) pp. 17–18.

89. G. Houle and E. Dubois, *Quantization of Color Images for Display on Graphics Terminals*, Proc. of GLOBE_ COM '86: 1986 IEEE Global Telecommunications Conference (1986) pp. 284–297.

90. Y. C. Hsueh, M. G. Chern, and C. H. Chu, *Image Requantization by Cardinality Distribution*, Computers & Graphics **15**(3) (1991) pp. 397–405.

91. D. H. Hubel, *Eye, Brain, and Vision*, Scientific American Library, New York (1988).

92. H. Ikeda, W. Dei, and Y. Higaki, *A Study on Colorimetric Errors Caused by Quantizing Color Information*, IEEE Transactions on Instrumentation and Measurement **41** (6) (1992) pp. 845–849.

93. N. Jacobson and W. Bender, *Strategies for Selecting a Fixed Palette of Colors*, Proc. of SPIE: Human Vision, Visual Processing, and Digital Display **1077** (1989) pp. 333–341.

94. B. Jähne, *Digital Image Processing: Concepts, Algorithms, and Scientific Applications*, Springer-Verlag, Berlin, third edition (1995).

95. A. K. Jain, *Fundamentals of Digital Image Processing*, Prentice Hall, Englewood Cliffs, NJ (1989).

96. J. F. Jarvis, C. N. Judice, and W. H. Ninke, *A Survey of Techniques for the Display of Continuous-Tone Pictures on Bilevel Displays*, Computer Graphics and Image Processing **5**(1) (1976) pp. 13–40.

97. J. F. Jarvis and C. S. Roberts, *A New Technique for Displaying Continuous Tone Images on a Bilevel Display*, IEEE Transactions on Communications **24** (1976) pp. 891–898.

98. G. Joy and Z. Xiang, *Center-Cut for Color-Image Quantization*, The Visual Computer **10**(1) (1993) pp. 62–66.

99. G. Joy and Z. Xiang, *Reducing False Contours in Quantized Color Images*, Computers & Graphics **20**(2) (1996) pp. 231–242.

100. D. B. Judd, *Basic Correlates of the Visual Stimulus*, in: S. S. Stevens (Ed.), Handbook of Experimental Psychology, John Wiley & Sons, New York (1951) pp. 811–867.

101. D. B. Judd, *Hue, Saturation, and Lightness of Surface Colors with Chromatic Illumination*, Journal of the Optical Society of America **30**(1) (1940) pp. 2–32.

102. B. Julesz and J. R. Bergen, *Textons, The Fundamental Elements in Preattentive Vision and Perception of Textures*, The Bell System Technical Journal **62**(6) (1983) pp. 1619–1645.

103. I. Katsavounidis and C.-C. J. Kuo, *A Multiscale Error Diffusion Technique for Digital Halftoning*, IEEE Transactions on Image Processing **6**(3) (1997) pp. 483–490.

104. C. Kim, S. Kim, Y. Seo, and I. Kweono, *Model-Based Color Halftoning Techniques on Perceptually Uniform Color Spaces*, IS&T's 47th Annual Conference/ICPS (1994) pp. 494–499.

105. S. A. Klein, *Image Quality and Image Compression: A Psychophysicist's Viewpoint*, in: A. B. Watson (Ed.), Digital Images and Human Vision, The MIT Press, Cambridge, Mass. (1993) pp. 73–88.

106. K. Knowlton and L. Harmon, *Computer-Produced Greyscales*, Computer Graphics and Image Processing **1**(1) (1972) pp. 1–20.

107. K. T. Knox, *Edge Enhancement in Error Diffusion*, Advance Printing of Paper Summaries: SPSE's 42nd Annual Conference (1989) pp. 310–313.

108. K. T. Knox, *Error Image in Error Diffusion*, Proc. of SPIE: Image Processing Algorithms and Techniques III **1657** (1992) pp. 268–279.

109. K. T. Knox and R. Eschbach, *Threshold Modulation in Error Diffusion*, Journal of Electronic Imaging **2**(3) (1993) pp. 185–192.

110. D. E. Knuth, *Fonts for Digital Halftones*, TUGboat **8**(2) (1987) pp. 135–160.

111. D. E. Knuth, *Digital Halftones by Dot Diffusion*, ACM Transactions on Graphics **6**(4) (1987) pp. 245–273.

112. S. Kollias and D. Anastassiou, *A Unified Neural Network Approach to Digital Image Halftoning*, IEEE Transactions on Signal Processing, **39** (1991) pp. 980–984.

113. B. W. Kolpatzik, C. A. Bouman, *Optimized Error Diffusion Based on a Human Visual Model*, Proc. of SPIE: Human Vision, Visual Processing, and Digital Display III **1666** (1992) pp. 152–164.

114. B. W. Kolpatzik, C. A. Bouman, *Optimized Error Diffusion for Image Display*, Journal of Electronic Imaging **1** (1992) pp. 277–292.

115. B. W. Kolpatzik, C. A. Bouman, *Optimized Universal Color Palette Design for Error Diffusion*, Journal of Electronic Imaging **4** (1995) pp. 131–143.

116. K. Kotani, Q. Gan, M. Miyahara, and V. R. Algazi, *Objective Picture Quality Scale for Color Image Coding*, Proc. of ICIP-95: 1995 IEEE International Conference on Image Processing II (1995) pp. 133–136.

117. T. Kurosawa and H. Kotera, *Multi-Level CAPIX Algorithm for High Quality Image Display*, SID Japan Display (1989) pp. 616–619.

118. T. Kurosawa, H. Tsuchiya, Y. Maruyama, H. Ohtsuka, and K. Nakazato, *A New Bi-Level Reproduction of Continuous Tone Images*, Proc. of the Second IEE International Conference on Image Processing and its Applications (1986) pp. 82–86.

119. B. J. Kurz, *Optimal Color Quantization for Color Displays*, IEEE Computer Vision and Pattern Recognition Proceedings (1983) pp. 217–224.

120. J. H. Ladd and J. E. Pinney, *Empirical Relationships with the Munsell Value Scale*, Proc. of IRE (Correspondence) **43**(9) (1955) p. 1137.

121. C.-C. Lai and D.-C. Tseng, *Printer Model and Least-Squares Halftoning Using Genetic Algorithms*, Journal of Imaging Science and Technology **42**(3) (1998) pp. 241–249.

122. D. L. Lau, G. R. Arce, and N. C. Gallagher, *Green Noise Digital Halftoning*, submitted for publication (1998).

123. H. Lee, A. H. Rowberg, M. S. Frank, H. S. Choi, and Y. Kim, *Subjective Evaluation of Compressed Image Quality*, Proc. of SPIE: Image Capture, Formatting, and Display **1653** (1992) pp. 241–251.

124. M. Y. Lermontov, *Hero of Our Time*, Otechestvennye Zapiski, Saint Petersburg (1839).

125. P. Li, J. P. Allebach, *Look-Up-Table Based Halftoning Algorithm*, Proc. of ICIP-98: 1998 IEEE International Conference on Image Processing VI (1998).

126. D. J. Lieberman, J. P. Allebach, *Digital Halftoning Using the Direct Binary Search Algorithm*, Proc. of the Fifth International Conference on High Technology: Imaging Science and Technology, Evolution and Promise, Chiba, Japan (1996) pp. 114–124.

127. J. O. Limb, *Design of Dither Waveforms for Quantized Visual Signals*, Bell System Technical Journal **48**(9) (1969) pp. 2555–2582.

128. Q. Lin, *Halftone Image Quality Analysis Based on a Human Vision Model*, Proc. of SPIE: Human Vision, Visual Processing, and Digital Display IV **1913** (1993) pp. 378–389.

129. Q. Lin, *Improving Halftone Uniformity and Tonal Response*, Proc. of IS&T's Tenth International Congress on Advances in Non-Impact Printing Technologies (1994) pp. 377–380.

130. Q. Lin, *Screen Design for Printing*, Proc. of the 1995 IEEE Intenational Conference on Image Processing (1995) pp. 331–334.

131. Q. Lin and J. P. Allebach, *Color FM Screen Design Using DBS Algorithm*, Proc. of SPIE: Color Imaging: Device Independent Color, Color Hardcopy, and Graphic Arts III **3300** (1998) pp. 353–360.

132. B. J. Lindbloom, *Accurate Color Reproduction for Computer Graphics*, Computer Graphics (Proc. of SIGGRAPH '89) **23**(3) (1989) pp. 117–126.

133. B. Lippel and M. Kurland, *The Effect of Dither on Luminance Quantization of Pictures*, IEEE Transactions on Communications Technology **19**(6) (1971) pp. 879–888.

134. S. P. Lloyd, *Least Squares Quantization in PCM*, IEEE Transactions on Information Theory **28**(2) (1982) pp. 129–137.

135. J. L. Mannos and D. J. Sakrison, *The Effects of a Visual Fidelity Criterion on the Encoding of Images*, IEEE Transactions on Information Theory **20**(4) (1974) pp. 525–536.

136. H. Marmolin, *Subjective MSE Measures*, IEEE Transactions on Systems, Man, and Cybernetics **16**(3) (1986) pp. 486–489.

137. S. L. Marple, Jr., *Digital Spectral Analysis with Applications*, Prentice-Hall, Englewood Cliffs, NJ (1987).

138. S. Matsumoto and B. Liu, *Analytical Fidelity Measures in the Characterization of Halftone Processes*, Journal of the Optical Society of America **70**(10) (1980) pp. 1248–1254.

139. J. Max, *Quantizing for Minimum Distortion*, IRE Transactions on Information Theory **6**(1) (1960) pp. 7–12.

140. *Merriam-Webster's Collegiate Dictionary*, Merriam-Webster, Springfield, Mass., tenth edition (1993).

141. R. Miller and C. Smith, *Mean-Preserving Multilevel Halftoning Algorithm*, Proc. of SPIE: Human Vision, Visual Processing, and Digital Display IV **1913** (1993) pp. 367–377.

142. R. Miller and J. R. Sullivan, *Color Halftoning Using Error Diffusion and a Human Visual System Model*, Advance Printing of Paper Summaries: SPSE's 43rd Annual Conference (1990) pp. 149–152.

143. G. Y. Milman, *Principles of Delta-Sigma Modulation in Digital Devices for Image Processing*, doctoral dissertation, Moscow Institute of Radioengineering, Electronics, and Automation (University of Technology), Russia (1995).

144. D. P. Mitchell, *Generating Antialiased Images at Low Sampling Densities*, Computer Graphics (Proc. of SIGGRAPH '87) **21**(4) (1987) pp. 65–72.

145. T. Mitsa, *Evaluation of Halftone Techniques Using Psychovisual Testing and Quantitative Quality Measures*, Proc. of SPIE: Human Vision, Visual Processing, and Digital Display III **1666** (1992) pp. 177–187.

146. T. Mitsa and J. R. Alford, *Applications of Fractal Analysis in the Evaluation of Halftoning Algorithms and a Fractal-Based Halftoning Scheme*, Proc. of SPIE: Human Vision, Visual Processing, and Digital Display V **2179** (1994) pp. 195–206.

147. T. Mitsa and K. J. Parker, *Digital Halftoning Technique Using a Blue-Noise Mask*, Journal of the Optical Society of America A **9**(11) (1992) pp. 1920–1929.

148. K. Miyata, M. Saito, N. Tsumura, and Y. Miyake, *An Evaluation of Image Quality for High Quality Digital Halftoning: Image Analysis and Evaluation of Multi-Level Error Diffusion*, Proc. of SPIE: The 1997 IS&T/SPIE International Symposium on Electronic Imaging Science and Technology, **3016** (1997) pp. 176–183.

149. J. B. Mulligan and A. J. Ahumada, Jr., *Principled Methods for Color Dithering Based on Models of the Human Visual System*, SID Digital Technology Papers (1992) pp. 194–197.

150. K. J. Myers and H. H. Barrett, *Addition of a Channel Mechanism to the Ideal-Observer Model*, Journal of the Optical Society of America A **4**(12) (1987) pp. 2447–2457.

151. K. J. Myers, H. H. Barrett, M. C. Borgstrom, D. D. Patton, and G. W. Seeley, *Effect of Noise Correlation on Detectability of Disk Signals in Medical Imaging*, Journal of the Optical Society of America A **2** (1985) pp. 1752–1759.

152. J. Nachmias and B. E. Rogowitz, *Masking by Spatially-Modulated Gratings*, Vision Research **23**(12) (1983) pp. 1621–1629.

153. R. Näsänen, *Visibility of Halftone Dot Textures*, IEEE Transactions on Systems, Man, and Cybernetics **14**(6) (1984) pp. 920–924.

154. N. B. Nill and B. H. Bouzas, *Objective Image Quality Measure Derived from Digital Image Power Spectra*, Optical Engineering (Redondo Beach, CA), **31**(4) (1992) pp. 813–825.

155. S. R. Norsworthy, R. Schreier, G. C. Temes (Eds.), *Delta-Sigma Data Converters: Theory, Design, and Simulation*, IEEE Press, New York (1997).

156. H. C. Nothdurft, *Different Effects from Spatial Frequency Masking in Texture Segregation and Texture Detection Tasks*, Vision Research **31**(2) (1991) pp. 299–320.

157. A. V. Oppenheim and J. S. Lim, *The Importance of Phase in Signals*, Proc. of the IEEE **69** (1981) pp. 529–541.

158. A. V. Oppenheim and R. W. Schafer, *Discrete-Time Signal Processing*, Prentice-Hall, Englewood Cliffs, NJ (1989).

159. M. T. Orchard and C. A. Bouman, *Color Quantization of Images*, IEEE Transactions on Signal Processing, **39**(12) (1991) pp. 2677–2690.

160. T. N. Pappas, *Digital Halftoning: A Model-Based Perspective*, International Journal of Imaging Systems and Technology **7**(2) (1996) pp. 110–120.

161. T. N. Pappas, *Model-Based Halftoning of Color Images*, IEEE Transactions on Image Processing **6**(7) (1997) pp. 1014–1024.

162. T. N. Pappas, D. L. Neuhoff, *Least-Squares Model-Based Halftoning*, Proc. of SPIE: Human Vision, Visual Processing, and Digital Display III **1666** (1992) pp. 165–176.

163. T. N. Pappas, C.-K. Dong, D. L. Neuhoff, *Measurement of Printer Parameters for Model-Based Halftoning*, Journal of Electronic Imaging **2**(3) (1993) pp. 193–204.

164. K. J. Parker, T. Mitsa, and R. Ulichney, *Digital Halftone Techniques in Medical Imaging*, Proc. of the Sixth International Congress on Advances in Non-Impact Printing Technologies (1990) pp. 853–858.

165. E. A. Patrick, D. R. Anderson, and F. K. Bechtel, *Mapping Multidimensional Space to One Dimension for Computer Output Display*, IEEE Transactions on Computers (1968) pp. 949–953.

166. D. E. Pearson, *Transmission and Display of Pictorial Information*, John Wiley & Sons, New York (1975).

167. E. Peli, *Contrast in Complex Images*, Journal of the Optical Society of America A **7**(10) (1990) pp. 2032–2040.

168. E. Peli, *In Search of a Contrast Metric: Matching the Perceived Contrast of Gabor Patches at Different Phases and Bandwidths*, Vision Research **37**(23) (1997) pp. 3217–3224.

169. B. Perry and M. L. Mendelsohn, *Picture Generation with a Standard Line Printer*, Communications of the ACM **7**(5) (1964) pp. 311–313.

170. L. N. Piotrowski and F. W. Campbell, *A Demonstration of the Visual Importance and Flexibility of Spatial-Frequency Amplitude and Phase*, Perception **11** (1982) pp. 337–346.

171. P. Pirsch, A. N. Netravali, *Transmission of Gray Level Images by Multilevel Dither Techniques*, Computers & Graphics **7**(1) (1983) pp. 31–44.

172. W. K. Pratt, *Digital Image Processing*, John Wiley & Sons, New York (1978).

173. W. K. Pratt, *Spatial Transform Coding of Color Images*, IEEE Transactions on Communications **19** (1971) pp. 980–992.

174. I. G. Priest, K. S. Gibson, and H. J. McNicholas, *An Examination of the Munsell Color Sysem, I. Spectral and Total Reflection and the Munsell Scale of Value*, U. S. National Bureau of Standards, Technical Paper 167 (1920).

175. F. Ratliff, *Mach Bands: Quantitative Studies on Neural Networks in the Retina*, Holden-Day, San Francisco (1965).

176. J. M. Risch, a UseNet posting quote, newsgroups `comp.dsp`, `comp.sys.ibm.pc.soundcard.tech`, `comp.speech`, `alt.sci.physics.acoustics` (1996).

177. P. G. Roetling and T. M. Holladay, *Tone Reproduction and Screen Design for Pictorial Electrographic Printing*, Journal of Applied Photographic Engineering **5**(4) (1979) pp. 179–182.

178. D. F. Rogers, *Procedural Elements for Computer Graphics*, McGraw-Hill, New York (1985).

179. E. Roytman and G. Gotsman, *Dynamic Color Quantization of Video Sequences*, IEEE Transactions on Visualization and Computer Graphics **1**(3) (1995) pp. 274–286.

180. M. B. Sachs, J. Nachmias, and J. G. Robson, *Spatial-Frequency Channels in Human Vision*, Journal of the Optical Society of America **61**(9) (1971) pp. 1176–1186.

181. H. Saito and N. Kobayashi, *Evolutionary Computation Approaches to Halftoning Algorithm*, Proc. of the First IEEE Conference on Evolutionary Computation (1994) pp. 787–791.

182. D. J. Sakrison, *Image Coding Applications of Vision Models*, in: W. K. Pratt (Ed.), Image Processing Techniques, Academic Press, San Diego, CA (1979) pp. 21–71.

183. D. J. Sakrison, *On the Role of the Observer and a Distortion Measure in Image Transmission*, IEEE Transactions on Communications **25**(11) (1977) pp. 1251–1267.

184. E. A. Sandler, D. A. Gusev, and G. Y. Milman, *Hybrid Algorithms for Digital Halftoning and Their Application to Medical Imaging*, Computers & Graphics **21**(1,6) (1997) pp. 69–78, 859 (erratum).

185. E. A. Sandler, D. A. Gusev, G. Y. Milman, M. L. Podolsky, *Estimating from Outputs of Oversampled Delta-Sigma Modulation*, Signal Processing **59**(3) (1997) pp. 305–311.

186. E. A. Sandler, G. Y. Milman, D. A. Gusev, *New Methods for Computer-Aided High-Quality Printing of Halftone Images*, Proceedings of the International Exhibition-Seminar COGRAPH-93 (Computational Geometry and Computer Graphics in Education), Nizhni Novgorod State University of Technology, Nizhni Novgorod (1993) p. 48 [in Russian].

187. T. Scheermesser, O. Bryngdahl, *Threshold Accepting for Constrained Halftoning*, Optics Communications **115**(1,2) (1995) pp. 13–18.

188. T. Scheermesser and O. Bryngdahl, *Texture Metric of Halftoning Images*, Journal of the Optical Society of America A **13**(1) (1996) pp. 18–24.

189. T. Scheermesser and O. Bryngdahl, *Spatially Dependent Texture Analysis and Control in Digital Halftoning*, Journal of the Optical Society of America A **14**(4) (1997) pp. 827–835.

190. M. Schroeder, *Images from Computers*, IEEE Spectrum **6**(3) (March 1969) pp. 66–78.

191. M. A. Seldowitz, J. P. Allebach, and D. W. Sweeney, *Synthesis of Digital Holograms by Direct Binary Search*, Applied Optics **26**(14) (1987) pp. 2788–2798.

192. G. Sharma and H. J. Trussell, *Digital Color Imaging*, IEEE Transactions on Image Processing **6**(7) (1997) pp. 901–932.

193. A. S. Sherstinsky, *M-Lattice: A System for Signal Synthesis and Processing Based on Reaction-Diffusion*, doctoral dissertation, the MIT, Cambridge, Mass. (1994).

194. A. S. Sherstinsky and R. W. Picard, *Color Halftoning with Textem M-Lattice*, Proc. of ICIP-95: 1995 IEEE International Conference on Image Processing II (1995), pp. 335–338.

195. P. Shirley, *Discrepancy as a Quality Measure for Sample Distributions*, in: F. H. Post and W. Barth (Eds.), Proc. of Eurographics '91, North Holland, Amsterdam (1991) pp. 183–194.

196. B. L. Shoop and E. K. Ressler, *Optimal Error Diffusion for Digital Halftoning Using an Optical Neural Network*, Proc. of ICIP-94: 1994 IEEE International Conference on Image Processing **II** (1994) pp. 1036–1040.

197. L. D. Silverstein, J. H. Krantz, F. E. Gomer, Y.-Y. Yeh, and R. W. Monty, *Effect of Spatial Sampling and Luminance Quantization on the Image Quality of Color Matrix Displays*, Journal of the Optical Society of America A **7**(10) (1990) pp. 1955–1969.

198. K. Sloan, *A Hybrid Scheme for Color Dithering*, Proc. of SPIE: Human Vision and Electronic Imaging: Models, Methods, and Applications **1249** (1990) pp. 238–248.

199. K. E. Spaulding, R. L. Miller, J. Schildkraut, *Methods for Generating Blue-Noise Dither Matrices for Digital Halftoning*, Journal of Electronic Imaging **6**(2) (1997) pp. 208–230.

200. K. E. Spaulding, L. A. Ray, and J. R. Sullivan, *Secondary Quantization of Color Images for Minimum Visual Distortion*, Proc. of SPIE: Human Vision, Visual Processing, and Digital Display IV **1913** (1993) pp. 261–269.

201. R. Steele, *Delta Modulation Systems*, Pentech Press, London; Halstead Press, New York (1975).

202. G. A. Stephen, *A Comparison of Selected Digital Halftoning Techniques*, Microprocessors and Microsystems **15** (1991) pp. 249–255.

203. R. L. Stevenson and G. R. Arce, *Binary Display of Hexagonally Sampled Continuous-Tone Images*, Journal of the Optical Society of America A **2** (1985) pp. 1009–1013.

204. M. C. Stone, W. B. Cowan, and J. C. Beatty, *Color Gamut Mapping and the Printing of Digital Images*, ACM Transactions on Graphics **7**(3) (1988) pp. 249–292.

205. P. Stucki, *MECCA — a Multiple-Error Correcting Computation Algorithm for Bilevel Image Hardcopy Reproduction*, Research Report RZ1060, IBM Research Laboratory, Zurich (1981).

206. P. Stucki, *3D Halftoning*, Proc. of SPIE: Imaging Science and Display Technologies **2949** (1997) pp. 314–317.

207. S. Sugiura and T. Makita, *An Improved Multilevel Error Diffusion Method*, Journal of Imaging Science and Technology **39**(6) (1995) pp. 495–501.

208. J. Sullivan, R. Miller, and G. Pios, *Image Halftoning Using a Visual Model in Error Diffusion*, Journal of the Optical Society of America A **10**(8) (1993) pp. 1714–1724.

209. J. Sullivan, L. Ray, and R. Miller, *Design of Minimum Visual Modulation Halftone Patterns*, IEEE Transactions on Systems, Man, and Cybernetics **21**(1) (1991) pp. 33–38.

210. Y. Tadmor and D. J. Tolhurst, *Both the Phase and Amplitude Spectrum May Determine the Appearance of Natural Images*, Vision Research **33** (1993) pp. 141–145.

211. C. C. Taylor, Z. Pizlo, J. P. Allebach, and C. A. Bouman, *Image Quality Assessment with a Gabor Pyramid Model of the Human Visual System*, Proc. of SPIE: The 1997 IS&T/SPIE

International Symposium on Electronic Imaging Science and Technology, **3016** (1997) pp. 58–69.

212. M. G. A. Thomson and D. H. Foster, *Role of Second- and Third-Order Statistics in the Discriminability of Natural Images*, Journal of the Optical Society of America A **14**(9) (1997) pp. 2081–2090.

213. S. Thurnhofer and S. K. Mitra, *Nonlinear Detail Enhancement of Error-Diffused Images*, Proc. of SPIE: Human Vision, Visual Processing, and Digital Display V **2179** (1994) pp. 170–181.

214. D. J. Tolhurst, Y. Tadmor, *Band-Limited Contrast in Natural Images Explains the Detectability of Changes in the Amplitude Spectra*, Vision Research **37**(23) (1997) pp. 3203–3215.

215. A. Tremeau, M. Calonnier, and B. Laget, *Color Quantization Error in Terms of Perceived Image Quality*, ICASSP-94: 1994 IEEE International Conference on Acoustics, Speech, and Signal Processing **5** (1994) pp. 93–96.

216. T. Tuttass and O. Bryngdahl, *Image Halftoning: Fourier Transform/Neural Net Iteration*, Optics Communications **99** (1,2) (1993) pp. 25–30.

217. T. Tuttass and O. Bryngdahl, *Neural Learning Algorithms for Halftoning*, Optics Communications **113** (1995) pp. 360–364.

218. R. Ulichney, *Digital Halftoning*, The MIT Press, Cambridge, Mass. (1987).

219. R. Ulichney, *Frequency Analysis of Ordered Dither*, Proc. of SPIE: Hard Copy Output **1079** (1989) pp. 361–373.

220. R. Ulichney, *Filter Design for Void-and-Cluster Dither Arrays*, SID 94 Digest (1994) pp. 809–812.

221. R. Ulichney, *The Void-and-Cluster Method for Dither Array Generation*, Proc. of SPIE: Human Vision, Visual Processing, and Digital Display IV **1913** (1993) pp. 332–343.

222. R. Ulichney, *Video Rendering*, Digital Technical Journal, **5**(2) (1993) pp. 9–18.

223. U. S. Federal Standard 1037C: Glossary of Telecommunications Terms.

224. L. Velho and J. de M. Gomes, *Digital Halftoning with Space Filling Curves*, Computer Graphics **25**(4) (1991) pp. 81–90.

225. S. J. Wan, P. Prusinkiewicz, and S. K. M. Wong, *Variance-Based Color Image Quantization for Frame Buffer Display*, Color Research and Application, **15**(1) (1990) pp. 52–58.

226. L. G. Wash and J. F. Hamilton, Jr., *The Design of a Graphic Arts Halftone Screening Computer*, Proc. of SPIE: Electronic Imaging Applications in Graphic Arts **1073** (1989) pp. 26–60.

227. A. B. Watson, *Efficiency of a Model Human Image Code*, Journal of the Optical Society of America A **4**(12) (1987) pp. 2401–2417.

228. A. B. Watson and J. A. Solomon, *Model of Visual Contrast Gain Control and Pattern Masking*, Journal of the Optical Society of America A **14**(9) (1997) pp. 2379–2391.

229. W. Watunyuta, C. H. Chu, *A Dither Pattern Ensemble Method for Digital Halftoning*, Optics Communications **129**(5,6) (1996) pp. 331–336.

230. S. Weissbach and F. Wyrowski, *Numerical Stability of the Error Diffusion Concept*, Optics Communications **93** (1992) pp. 151–155.

231. J. S. Wisniewski, a UseNet posting, newsgroups `comp.dsp`, `comp.sys.ibm.pc.soundcard.tech`, `comp.speech`, `alt.sci.physics.acoustics` (1996).

232. I. H. Witten and R. M. Neal, *Using Peano Curves for Bilevel Display of Continuous-Tone Images*, IEEE Computer Graphics and Applications **2**(3) (1982) pp. 47–52.

233. P. W. Wong, *Error Diffusion with Dynamically Adjusted Kernel*, ICASSP-94: 1994 IEEE International Conference on Acoustics, Speech, and Signal Processing **5** (1994) pp. 113–116.

234. P. W. Wong, *Adaptive Error Diffusion and Its Application in Multiresolution Rendering*, IEEE Transactions on Image Processing **5**(7) (1996) pp. 1184–1196.

235. T. Woodlief, Jr. (Ed.), *SPSE Handbook of Photographic Science and Engineering*, John Wiley & Sons, New York (1973).

236. X. Wu, *Color Quantization by Dynamic Programming and Principal Analysis*, ACM Transactions on Graphics **11**(4) (1992) pp. 348–372.

237. X. Wu, *Efficient Statistical Computations for Optimal Color Quantization*, in: J. Arvo (Ed.), Graphics Gems II, Academic Press Professional, Cambridge, Mass. (1991) pp. 126–133.

238. X. Wu, *Optimal Quantization by Matrix-Searching*, Journal of Algorithms **12**(4) (1992) pp. 663–673.

239. X. Wu, *Statistical Color Quantization for Minimum Distortion*, in: B. Falcidieno, I. Herman, and C. Pienovi (Eds.), Computer Graphics and Mathematics, Springer-Verlag, Berlin (1992) pp. 189–202.

240. Z. Xiang, *Color Image Quantization by Minimizing the Maximum Intercluster Distance*, ACM Transactions on Graphics **16**(3) (1997) pp. 260–276.

241. Z. Xiang and G. Joy, *Color Image Quantization by Agglomerative Clustering*, IEEE Computer Graphics and Applications **14**(3) (1994) pp. 44–48.

242. Z. Xiang and G. Joy, *Feedback-Based Quantization of Color Images*, Proc. of SPIE: Image and Video Processing II **2182** (1994) pp. 34–42.

243. M. Yao, K. J. Parker, *Modified Approach to the Construction of a Blue Noise Mask*, Journal of Electronic Imaging **3**(1) (1994) pp. 92–97.

244. J. I. Yellott, Jr., *Implications of Triple Correlation Uniqueness for Texture Statistics and the Julesz Conjecture*, Journal of the Optical Society of America A **10**(5) (1993) pp. 777–793.

245. A. Zakhor, S. Lin, and F. Eskafi, *A New Class of B/W Halftoning Algorithms*, IEEE Transactions on Image Processing **2**(4) (1993) pp. 499–508.

246. T. Zeggel, *Lokal adaptive Halbtonverfahren*, doctoral dissertation, University of Essen, Germany (1997).

247. T. Zeggel, O. Bryngdahl, *Halftoning with Error Diffusion on an Image-Adaptive Raster*, Journal of Electronic Imaging **3**(3) (1994) pp. 288–294.

248. T. Zeggel, O. Bryngdahl, *Halftoning with Iterative Convolution Algorithm*, Optics Communications **118**(5,6) (1995) pp. 484–490.

249. T. Zeggel, O. Bryngdahl, *Gradient-Controlled Iterative Half-Toning*, Applied Optics **36**(2) (1997) pp. 423–429.

250. T. Zeggel, S. Weissbach, and O. Bryngdahl, *Noise Modification in Iterative Multi-Level Image Quantization*, Optics Communications **100** (1993) pp. 67–71.

251. S. K. Zeremba, *The Mathematical Basis of Monte Carlo and Quasi-Monte Carlo Methods*, SIAM Review **10**(3) (1968) pp. 303–314.

252. C. Zetzsche and G. Hauske, *Multiple Channel Model for the Prediction of Subjective Image Quality*, Proc. of SPIE: Human Vision, Visual Processing, and Digital Display **1077** (1989) pp. 209–216.

253. Y. Zhang and R. E. Webber, *Space Diffusion: An Improved Parallel Halftoning Technique Using Space-Filling Curves*, Computer Graphics Proceedings (1993) pp. 305–312.